Master's thesis

NTNU
Norwegian University of Science and Technology
Faculty of Engineering
Department of Marine Technology

Enrico Pettineo

Dynamic response analysis of a semi-submersible floating wind turbines during combined ice and aerodynamic loads

Master's thesis in Maritime Engineering
Supervisor: Zhen Gao
Co-supervisor: Ekaterina Kim, Pentti Kujala
July 2021

NTNU
Norwegian University of
Science and Technology

Enrico Pettineo

Dynamic response analysis of a semi-submersible floating wind turbines during combined ice and aerodynamic loads

Master's thesis in Maritime Engineering
Supervisor: Zhen Gao
Co-supervisor: Ekaterina Kim, Pentti Kujala
July 2021

Norwegian University of Science and Technology
Faculty of Engineering
Department of Marine Technology

NTNU
Norwegian University of
Science and Technology

NTNU
Norwegian University of Science and Technology

Aalto University
School of Engineering

Department of Marine Technology

TMR4930 - Master's Thesis

Master's Thesis

Dynamic response analysis of a semi-submersible floating wind turbines under combined ice and aerodynamic loads

Author:
Enrico Pettineo

Supervisor:
Professor Zhen Gao
Co-supervisors:
Professor Ekaterina Kim
Professor Pentti Kujala

July 14, 2021

Acknowledgments

I would like to start by thanking my supervisors: Professor Ekaterina Kim, Professor Pentti Kujala and Professor Zhen Gao. The help they provided me and their understanding of the issues I faced during this work was fundamental for me. I would not have been able to achieve this goal without them. I also want to thank Professor Poul Anderson, Professor Jani Romanoff and all the people involved in the organization of Nordic Master in Maritime Engineering. Being part of this program was an amazing experience which made me grow as an engineer and as a person.

To Professor Zhen Gao, who gave me the opportunity to work on such an interesting topic and who took a lot of time to answer my numerous question and to help me solve the numerous issues I faced.

To Professor Ekaterina Kim, who provided me a lot of useful suggestion and comments and who gave me not only academic support but also human support.

To Professor Pentti Kujala, who has always been available to help me and to share his deep knowledge with me.

To Professor Erin Bachynski, Professor Wei Shi and PhD. candidate George Katsikogiannis, for the precious help they provided me regarding the software and the ice DLL.

To all the friends from Helsinki and Trondheim, because these two years would not have been this great without you all.

To Elena and Salvatore, who have always been there for me, despite everything.

To my family, because without them I would not be here. This achievement belongs to you too.

Finally, to my grandfather, whom this work is dedicated. Without the fear that you were no longer here, this would have taken much more time.

Abstract

This thesis aims to analyze the dynamic response of a semi-submersible floating wind turbine under combined wind and ice loads through a coupled analysis. The importance of the topic is due to the increased interest and investments in the renewable energy and particularly in the wind energy. Lots of cold region have shown great potential in terms of wind energy and therefore the effect of ice loads on wind turbines should be investigated. Among the different types of floating wind turbine concepts, semi-submersible platform are probably the most suitable for operating in cold region due to the high stability, the depth flexibility and the possibility to fit the column with ice-breaking cones without compromising the hydrodynamic performances.

The analysis was performed using a aero-servo-hydro-elastic model developed on the software SIMA that was coupled with a semi-empirical ice module developed through a FORTRAN DLL. The loads acting on the platform and on the wind turbine are: ice loads, aerodynamic loads, mooring line loads and hydrodynamic loads. When evaluating the hydrodynamic loads, no waves are considered since they are assumed to be damped out by the ice.

First, we analyzed the ice load on a bottom fixed cylinder in order to test the ice load DLL and to understand how the different parameters affected the ice loads. After that, we performed different sets of coupled analysis on the floating wind turbine. For each set, we considered both ice and wind load and we kept one parameter constant while changing the others to understand how the ice characteristics affect the ice load and consequently the platform motion.

Our analysis showed that the ice load magnitude increases with both the ice thickness and the ice drifting speed, while the ice load frequency increases with the ice drifting speed and it decreases with increasing ice thickness. It also showed that the wind loads are dominant in wind direction, while the ice loads are dominant in the direction perpendicular to the wind direction. Regarding the ice load influence on the platform motion, we found out that roll and sway motion are the most affected by the ice loads while pitch and surge depend mainly on the wind loads. Moreover, the ice loads showed a damping effect on the platform motion in most of the cases, while only a few load cases resulted in a motion amplification effect which was related mainly to the roll motion.

Contents

List of Figures

List of Tables

List of Abbreviation

BEM	Blade Element Momentum
DLL	Dynamic Link Library
DOF	Degrees Of Freedom
FOWT	Floating Offshore Wind Technologies
GWEC	Global Wind Energy Council
ISO	International Organization of Standardization
LCOE	Levelized Cost of Energy
MSL	Mean Sea Level
OREAC	Ocean Renewable Energy Action Coalition
QTF	Quadratic Transfer Function
YoY	Year over Year
TLP	Tension Leg Platform
WL	Water Line

List of Symbols

$^{(1)}$	First order quantities
$^{(2)}$	Second order quantities
A	Disk Area
$\mathbf{A}$	Added mass matrix
A_{cr}	Contact Area
a	Axial induction factor
a'	Angular induction factor
B	Number of blades
$\mathbf{B}$	Potential damping matrix
$\mathbf{C}$	Linear restoring matrix
C_D	Drag coefficient
C_L	Lift coefficient
C_N	Normal force coefficient
C_T	Tangential force coefficient
c	Cord length
D	Drag force
D	Column diameter (§3.1.3)
F	Prandtl correction factor (§3.1.2)
F_{cr}	Local crushing force
F_{DLL}	Force due to ice load in the DLL reference system
F_{SIMA}	Force due to ice load in the SIMA reference system
$\mathbf{F}$	Force vector
g	Acceleration of gravity
h_i	Ice thickness
i	Imaginary unit
L	Lift force
L_d	Indentation length
L_h	Contact length
$\mathbf{M}$	Mass matrix
M_{DLL}	Moment due to ice load in the DLL reference system
M_{SIMA}	Moment due to ice load in the SIMA reference system
$\mathbf{n}$	Normal vector pointing into the fluid
P_N	Force normal to the blade
P_T	Force tangential to the blade
p	Pressure
Q	Torque
R	Rotor radius
$\mathbf{R}$	Rotation matrix
r	Disk radius
$\mathbf{r}_0$	Initial position of the platform column in the body reference system
$\mathbf{r}$	Position of the platform column in the body reference system
S_{0B}	Mean body surface
S_B	Instantaneous body surface
T	Thrust
T	Quadratic transfer function (§3.2.1)
$\mathbf{T}$	Tension (§3.3)
$U(z)$	Wind speed at height z
$\mathbf{U}$	Relative velocity between tower and wind at height z (§3.1.3)
$\bar{U}$	Mean wind speed

U_{ref}	Wind speed at reference height z_{ref}
$u'(t)$	Wind speed variation over time (turbulence)
$\mathbf{V}_b$	Body velocity
v	Wind speed (§3.1.2)
v_i	Ice drifting speed
v_w	Average wind speed
$\mathbf{w}$	Mooring line specific weight
z_{ref}	Reference height
α	Vertical shear exponent
$\boldsymbol{\eta}$	Body displacement vector
Δt	Simulation time step
ξ_a	Wave amplitude
ρ_a	Air density
ρ_i	Ice density
ρ_w	Water density
σ	Solidity ratio
ϕ	Flow angle (§3.1.3)
ϕ	Velocity potential (§3.2.1)
ϕ	Angle between mooring line and seabed (§3.3)
ϕ	Frame angle (§4.2)
Ω	Rotor rotational speed
ω	Wake rotational speed (§3.1.2)
ω	Frequency
$\boldsymbol{\omega}$	Platform angular position

1 Introduction

1.1 Wind Energy Industry

The importance of renewable energy industry has been constantly growing in the last years due to the increased concern about global warming and greenhouse effects. Because of that, several international bodies have set new target for renawable energy market. E.g. the European Union's Renewable Energy Directive has set the renewable energy target for the EU for 2030 of at least 32% [1], increasing this target by 5% with respect to the previous directive [2].

Among the different sources of renewable energy, wind energy has been emerging as probably the most relevant for the near future: the 93 GW installed worldwide in 2020 brought its installed capacity to 743 GW, resulting in year-over-year (YoY) growth of 14% and making it the second highest source among all renowable energy sources [3].

Onshore market is the most established one in the wind energy field, since onshore wind turbines have been used for electricity production since the early 20^{th} century [4] and have been developing ever since, reaching a reliable level in technology and a competitive cost. In 2019, onshore wind accounted for almost 91% of the total wind energy installed power, with 86.9 GW [5]

Moreover, wind as an usable energy source is diffused worldwide both onshore and offshore, pushing national government and international bodies to invest in this field, thus improving the technology and reducing the costs. As a result, wind energy is forecasted to keep growing at very high rate, reaching a total installed power of 6.2 TW in 2050 and providing, together with solar energy, 24% of the total world electricity in 2030 and 62% in 2050 [6].

1.2 Offshore Wind Industry Status

Unlike onshore wind, offshore wind is a quite new technology: the first offshore wind farm was built in 1991 near the cost of Denmark [7]. Moreover, it has to deal with a number of extra challenges due to the sea action in addition to normal onshore turbines challenges. As a results, state of the art offshore wind turbines are more complex and expensive then onshore ones.

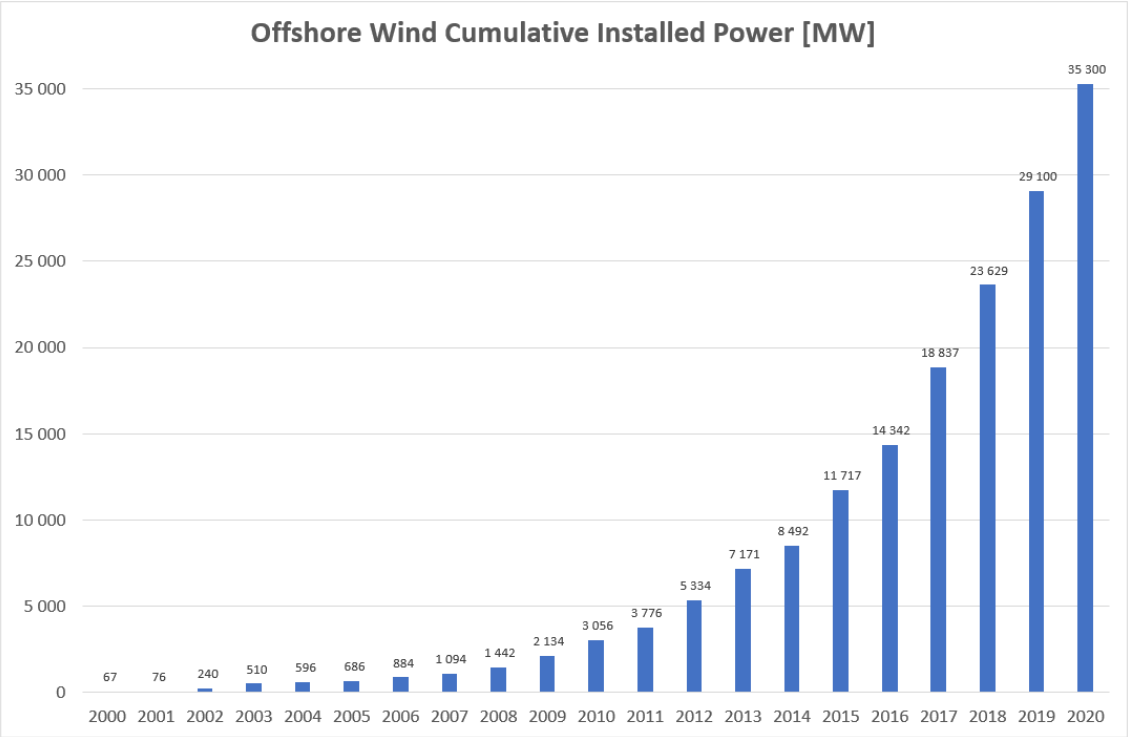

Figure 1.1: Offshore wind installed power

However, offshore wind installed power has grown by 27% in average during last 5 years, as shown in Figure 1.1, with last 2 years particularly being the best year ever with over 6 GW installed worldwide in both years[5]. China, UK and Germany were the leading markets in 2019, but the US and other European country have shown important growth too and can represent important markets for the future due to their high potential [8]. One reason for this growth is that, unlike the onshore ones, offshore wind turbines do not require land space and do not affect cities with noise pollution. Moreover, wind speed is the most relevant parameter when it comes to deciding the location for a wind farm [9] and it is usually higher and steadier in offshore location than on-land, making offshore wind farms more productive with higher capacity factors [10].

The most of the offshore wind turbines are nowadays located in shallow waters and therefore they consists in bottom fixed monopile wind turbines. Of the 6.1 GW installed in 2019, only 11.4 MW are due to floating wind, of which 8.4 MW is from Portugal and 3 MW from Japan [8].

However, 80% of global offshore wind resource potential is located in water deeper then 60 m [8], thus making the role of floating offshore wind technologies (FOWT) of primary importance for the development of the sector. FOWT are a very recent technology: the first full-scale operating wind farm is Hywind Scotland, a floating wind farm completed by Equinor in 2017 consisting in five 6MW floating wind turbines [11].

FOWT present many challenges in terms of installation, stability and dynamic behavior, and therefore only a few project have already reached the production stage. These extra challenges, together with the late start of the development are the reason for the maximum installed power for FOWT to be less then that of bottom fixed wind turbines: 8.4 MW reached by MHI Vestas V16 compared to the 15 MW reached by Siemens Gamesa SG14-222 DD.

1.3 Offshore Wind Outlook Prediction

Due to the high potential of wind as an energy source and to the growing importance of renewable energy, offshore wind industry is forecast to grow at high rate in the near future [8]. Another driving force for the development of the sector, will be the technological improvement that will be achieved in the near future, resulting in cheaper and bigger structures. As shown in Figure 1.2, average turbine size has been growing constantly in the past 20 years and is forecast to keep growing in the future.

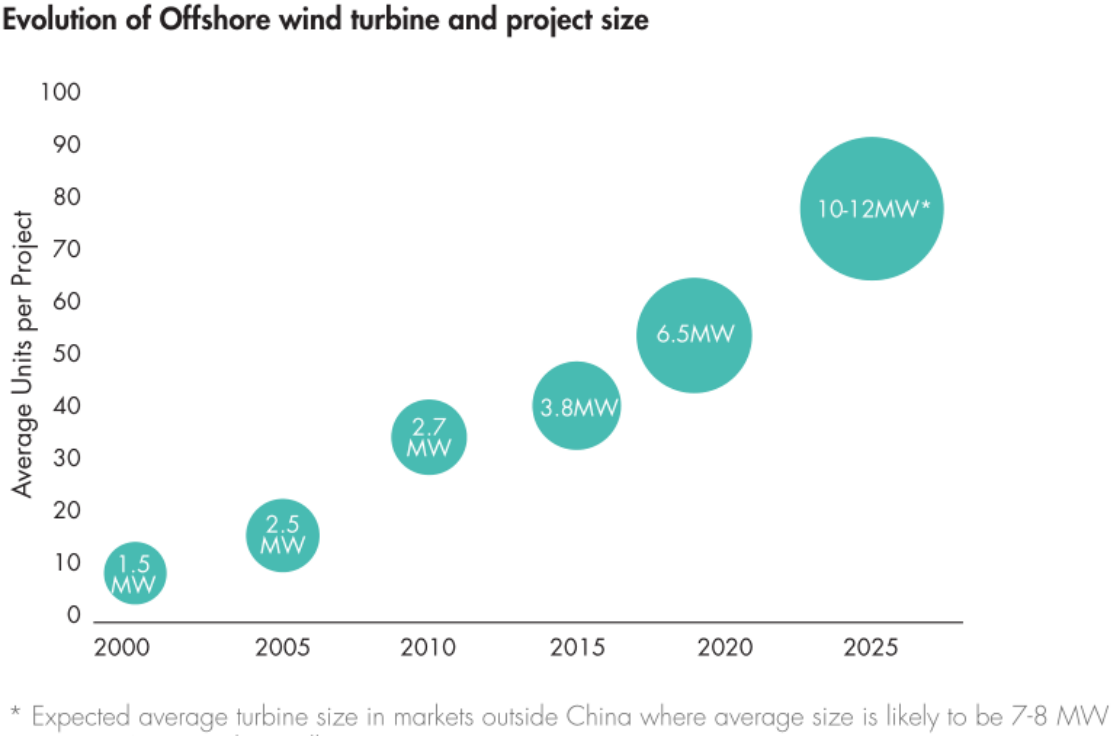

Figure 1.2: Evolution of Offshore wind turbine and project size [8]

It should be also considered that wind energy may not be used only for industrial electricity production, but also for other purposes that may boost its importance even more. Among these, green hydrogen production, that consists in electrolyzing the water using the electricity produced by a wind turbine [12], is one of the most promising purposes for wind energy [13].

New installations are expected to reach 20 GW in 2025 and 30 GW 2030, while the total installed power at the end of the decade is expected to be higher than 205 GW [8]. Despite the fact that the entire wind energy industry will undergo a substantial improvement, offshore wind share of the market is foreseen to become even bigger, increasing from the 10% of 2019 to 20% in 2025, driven also by the increased competitiveness of the cost: offshore wind Levelized Cost of Energy (LCOE) is forecast to drop and reach onshore wind one [14].

Looking beyond the next decade, national government and international organization are setting the goals to even higher level. The Ocean Renewable Energy Action Coalition (OREAC) targets 1.4 TW of offshore wind [8], while the EU alone aims to reach between 240 GW and 450 GW of offshore wind installed power by 2050 [15]. In order to meet the goal aimed by EU, all the European main locations (Atlantic Ocean, North sea, Baltic sea and south Mediterranean) need to substantially increase the amount of power they

install every year [16]. Moreover, several challenges will be faced in order to meet this goal, including understanding of the environmental impact of wind turbine, ensuring the multipurpose use of sea areas and, most important, the exploration of new areas such as deeper water and frozen seas.

As already mentioned, when aiming to expand the offshore wind industry towards unexplored areas characterized by deeper water, the role of FOWT becomes of primary importance, but the complexity and the high cost of these technology could slow down its development. However, as shown in Figure 1.3 floating offshore wind cost is forecast to drop by approximately 50% in 2030 and 60% in 2050, due to the R&D effects and to the increased capacity.

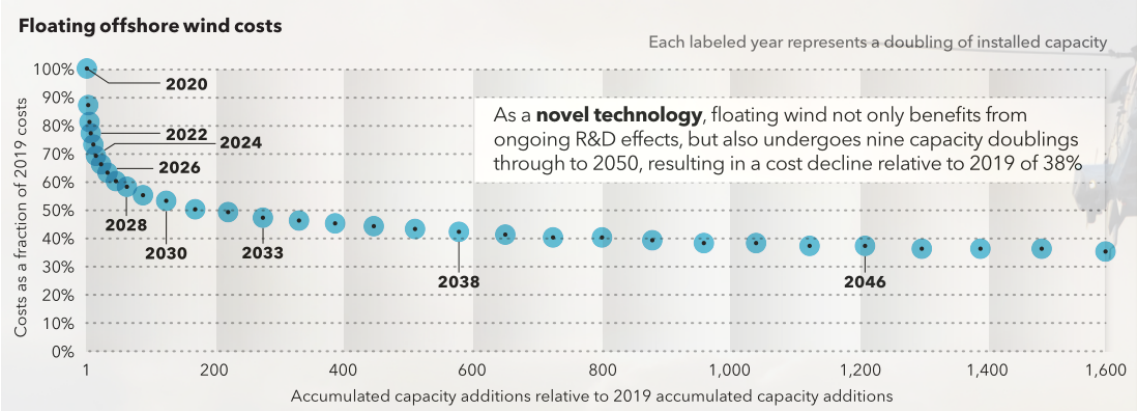

Figure 1.3: FOWT cost forecast up to 2050 [6]

1.4 Future Development of FOWT

From previous sections we can conclude that the offshore wind industry is growing and will probably keep growing in the next 30 years. In order to do to this and to match the world increasing need of clean energy, new solutions should be found and new possibilities should be explored. The most realistic way the offshore wind industry has to do this is through the exploitation of the regions with higher potential than those that are being exploited today.

As already mentioned, wind as an energy source is distributed world-wide, but some regions show higher potential than others, especially when talking about offshore wind. As can be seen in Fig. 1.4, Asia, Americas and Northern Europe are the most interesting regions, with a wind potential speed way above the lower limit for wind energy production (usually around 7 m/s). Therefore it is not a surprise that all the existing offshore wind farms are located in these regions.

Moreover, we can notice that lots of high-potential regions are located in cold and harsh environments, including Canada, Barents Sea, Bering Sea, Greenland Sea, Great Lakes and the Arctic. As shown in Fig. 1.5, in these regions the sea is frozen for at least some months during the year. This means that a floating wind turbine to be placed in this locations need to be designed for withstanding ice loads, making the design process more complex and expensive.

Despite the fact that realizing a floating wind turbine in ice-covered seas presents extra challenges, it is worth to analyze the possibility of such a structure to be designed, since this areas are of strong interest for the offshore wind market. For instance, the Baltic

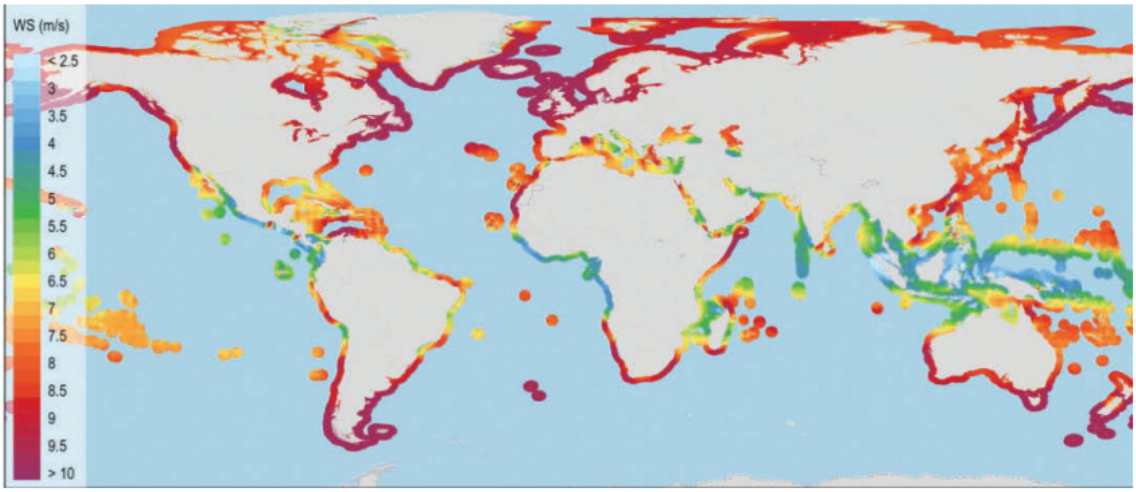

Figure 1.4: Global offshore wind speed up to 200 km from shore at 100 m hub height [17]

sea annual installations need to increase from the actual 2.2 GW per year to 3.6 GW per year between 2030 and 2040 in order to meeti the European Union target, resulting in an occupation of 720 km^2 per year [16], meaning that a substantial amount of space will be occupied by wind turbines and that there is a high possibility that ice-covered sea areas will be taken into account. Therefore we can conclude that a niche exists for floating wind turbines in ice, because of the need for extra wind sources and of the high potential of these regions.

Another aspect that should be considered when selecting possible location for a FOWT in ice is the sea depth. In fact, sea depth is a key parameter for the selection of the type of unit, since spar buoy can not be placed in water shallower than 120 m. Because of that, an interesting possible location such as the Baltic Sea, is more suitable for Semi-submersible or TLP platform, that can be used up to 50 m of depth, since the Baltic Sea average depth is approximately 50 m and 86% of it is shallower than 100 m [18].

Nowadays, no floating wind turbines exist in frozen seas but some oil and gas platform can be found in these regions. Moreover, oil and gas platform concepts are already the source for the existing FOWT, meaning that also the ones designed for ice can be used as a starting point for this study.

Therefore the aim of this thesis is to present a possible methods to perform a dynamic coupled analysis of a floating wind turbine under combined ice and wind loads. The software SIMA will be used for the simulations while the ice load will ice load will be evaluated through an external Dynamic Link Library (DLL) written in Fortran. As shown in the following sections, semi-submersible platform are the most suitable for this application and therefore this kind of structure will be considered. Particularly, the 10 MW CSC platform described by Qiang Wang Master's Thesis [19] will be used, since this model already exists in SIMA. Different combination of wind speed, ice thickness and ice drifting speed will be chosen based on environmental data from the Baltic Sea and corresponding results will be presented. It should be noted that not all the possible cases will be covered since the main aim of this work is to establish a methodology that can be improved and applied for design purposes.

We will start by presenting the different concepts of FOWT and by selecting the most suitable one for ice operation. The main characteristics of the considered model, the 10 MW CSC semi-submersible platform, will also be presented. Then we will discuss

the theory and models used to account for the different type of loads: aerodynamic, hydrodynamic, mooring lines and ice loads. After that the coupled analysis theory and the method used to solve it will be presented. Finally, the results of the relevant load cases will be shown in terms of loads and platform motion.

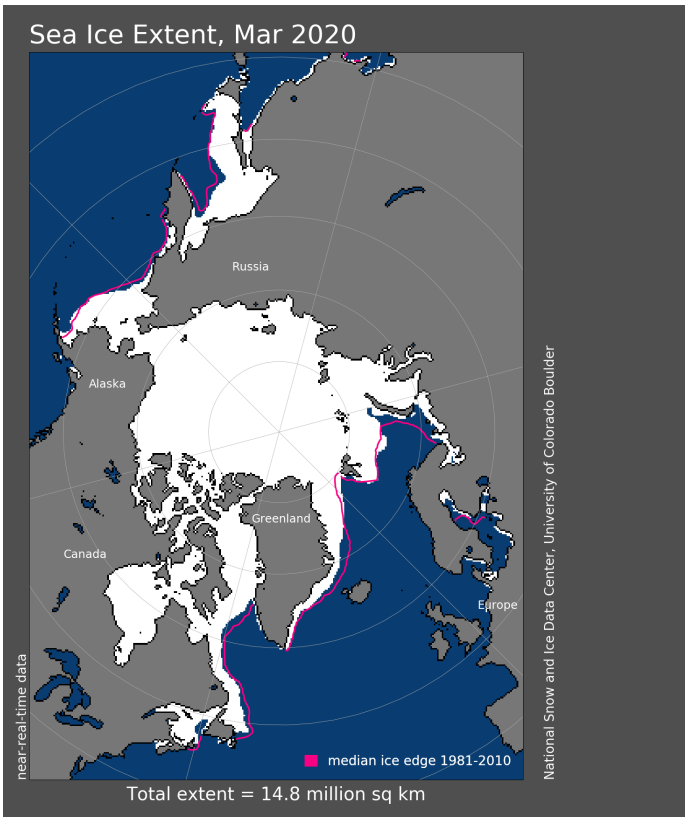

Figure 1.5: Maximum winter ice extent in Arctic in 2020 (areas with concentration higher than 5% are marked) [20]

2 Floating Wind Turbines Concepts

The existing FOWT derives mainly from the oil and gas sector and at the moment four different concept of floating platforms supporting the rotor exists: barge, semi-submersible, spar buoy and tension leg platform (TLP). The first three concepts have already been tested and are nowadays used in free water condition, but none of them have been built for frozen sea and therefore we must refer to oil and gas technology that already account for different concepts of floating platform designed to withstand ice loads. On the other hand, barges have never been tested or built in full scale as a support for wind turbines, probably due to the large wave-induced motions [21], so we will not discuss this solution in the following.

These concepts presents many differences that make them more suitable for some conditions than for others and therefore it is important to understand the main advantages and disadvantages of each of them in order to select the best solution for the analyzed case. Since we are aiming to analyze how a floating wind turbine responds to combined ice, aerodynamic and hydrodynamic loads, we are interested in characteristics such as the overall strength of the structure with respect to drifting ice loads, the dynamic stability and the reliability of the structure and of its mooring lines.

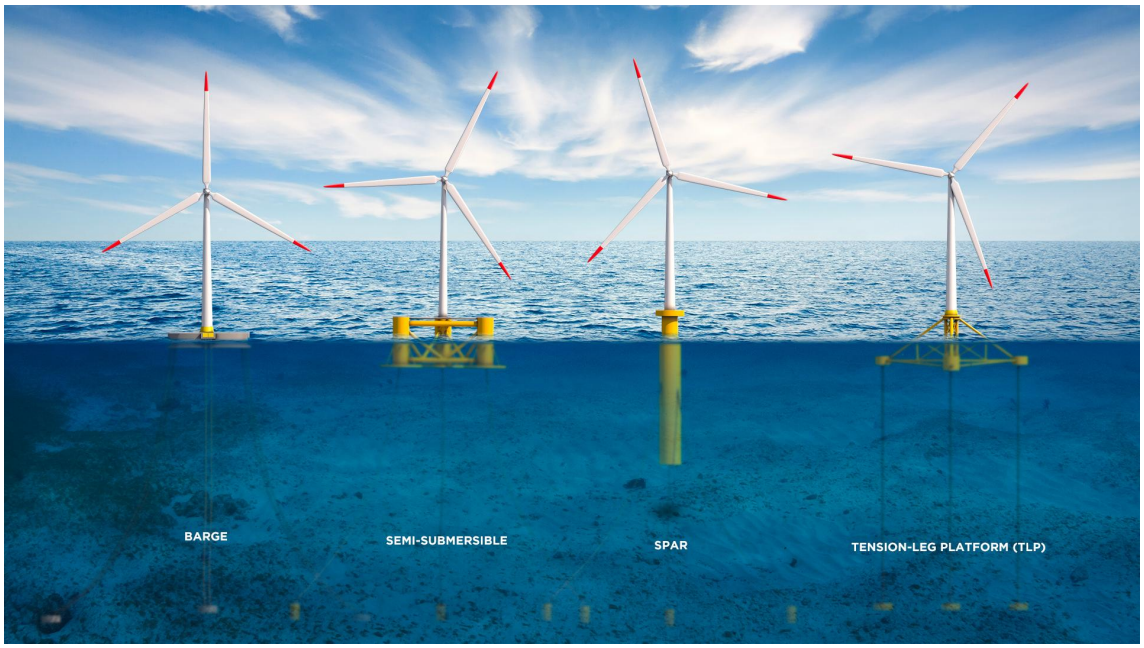

Figure 2.1: Illustrations of floating wind turbines supported by a barge, a semi-submersible platform, a spar buoy and a tension leg platform [22]

All the concepts are kept in position by passive mooring line system, but they show substantial differences in other aspects [21]. Floaters dynamic behavior particularly is a fundamental aspect in the design process, since the wave loads, that constitute the most relevant component of the hydrodynamic loads, depends on this. Ocean waves contain 1^{st} harmonic wave energy in the period range of 5 - 25 s [23], thus this range is to be avoided for the floater motions natural period. As shown in Table 2.1, all concepts are "soft" in the horizontal plane, while they show differences in the vertical plane motions, which have the highest influence on loads acting on both the platform and the mooring lines. TLP platform are "stiff" with respect to vertical plane motion, while semi and spar are soft, with the natural period being higher than the typical ocean waves period [23].

Table 2.1: Typical natural periods of deep water floaters [23]

	Semi	Spar	TLP
Surge	> 100	> 100	> 100
Sway	> 100	> 100	> 100
Heave	20 - 50	20 - 35	< 5
Roll	30 - 60	50 - 90	< 5
Pitch	30 - 60	50 - 90	< 5
Yaw	> 100	> 100	> 100

In addition to the natural periods, the concepts presents differences in other aspects, including the physical principle used to achieve static stability, dynamic behavior, fabrication, installation process and cost. This should be considered before choosing the floater to analyze, so we will summarize these differences in the following sections.

2.1 Semi-submersible

Semi-submersible are column-stabilized units, that consist of a deck structure with large diameter support columns attached to submerged pontoons and therefore they achieve stability by water plane stiffness. Some of them can be equipped with active ballast systems that improve stability and prevent tilt in rough seas. This type of floaters have reduced draught if compared to spar and installation process does not require specialized vessel as the platform can be towed in position, making the installation process easy and the unit flexible in terms of sea depth ($> 50\,\mathrm{m}$), soil condition and weather conditions. Moreover, semi-submersible platforms mooring and anchoring systems are cheap and simple, since an eventual failure of this systems does not represent a fatal event for the survival of the unit.

Most of the negative aspects of semi-submersible are related to the fabrication process, which requires a dry dock and can not be industrialized due to the complexity and size of the structure. Another shortcoming is that the floater can be subjected to big lateral motions that can presents problem for the export cable.

2.2 Spar

Spar buoy usually consists of a ballast stabilized cylinder structure with large mass mainly distributed below the water line. Even though they can show relatively large motions, Spar are suitable for high sea states as they are characterized by a low operational risk. Their fabrication process is simple and can be industrialized due to the overall low complexity of the structure. Moreover, their mooring and anchoring system are cheap and simple and can be applied to every soil condition.

Spar buoy has the highest draugth among these concepts, therefore they are only suited for water deeper than 120 m. Because of this and also because of their heavy weight, spar need specialized installation vessels. Other two negative aspects of this type of floater is that it has high cost per MW and that the structure is the heaviest one.

2.3 TLP

Tension Leg Platform consists in a submerged platform that gains stability by the tension in the mooring line because its buoyancy is higher than its weight. TLP can be used regardless the sea depth ($> 50\,\mathrm{m}$) and since they are stiff to wave loads, they show low motions and high stability. They are the lightest structure among the others and they are also cheap in terms of material cost due to the reduced structural weight. Moreover, their mooring lines anchorage occupy a small amount of seabed if compared to other floaters, thus reducing the seabed footprint. Moreover they are flexible in terms of production, since they can be fabricated both onshore or on dry dock and can be handled easily due to the low weight.

The main negative aspects of TLP are related to the mooring lines. This system is subjected to huge tension forces and therefore it is complex and very expensive both to built and to maintain. Moreover, a mooring failure would cause a complete loss of stability of the structure meaning that lot of maintenance is required as well as an extensive knowledge of the seabed conditions. In addition to that, the high risk connected to the mooring systems, makes TLP not suitable for heavy sea states. Installation process is

another key issue for TLP because, as already mentioned they gain stability from mooring lines and therefore they are unstable up to when they are anchored. As a result, the process is complex and expensive and it requires purpose-built vessels, making the TLP overall cost the highest among the considered concepts.

2.4 Concept Comparison

Each of the considered concepts have its own positive and negative aspects, so a case by case analysis is required depending on the location and on the requirements. In our case, we do not know the exact location, but we can extrapolate some environmental conditions based on the consideration of the previous sections. Since we are aiming to investigate how a FOWT respond to ice loads, the considered platform needs to be able to withstand these loads with reasonable modification in its design. Moreover, regions where sea actually freezes are usually characterized by rough sea states for part of the year, with the only exceptions of Baltic Sea and Great Lakes. However, these two regions are characterized by shallow waters, so sea depth flexibility is another important aspects.

Another aspect we should consider when selecting the concept to analyze is how the different options are developing in the industry. The first FOWT ever built (Hywind Scotland) were supported by Spar Buoys and these concept remain the most used up until now [13]. However, according to GWEC Market Intelligence's, semi-submersible platform are generally gaining popularity due to the relatively low cost, reliability and site flexibility and are foreseen to account for about 62% share of the market by 2022 [13]. On the other hand, TLP are not as diffused as the former 2, most probably due to the high costs and to the high risk, even though they have even higher flexibility with respect to water depth than semi-submersibles.

Summarizing all these aspects, we can conclude that semi-submersible are probably the best choice to test FOWT response to ice loads. In fact, this concepts can be easily modified to better withstand ice loads, by changing the column shape to cylindrical shape. Moreover, they are suitable both for heavy seas, which are typical of Canada, Barents Sea, Bering Sea, Greenland Sea, and Arctic, and for shallow waters, which characterize other cold regions like Baltic Sea and Great Lakes. Therefore semi-submersible could be used almost in every location where sea get frozen, unlike TLP and spar which are not suitable for rough seas or shallow waters respectively. In addition to that, semi-submersible will probably be the leader of the FOWT market in the near future, making it important to have a comprehensive knowledge of their behavior in different conditions.

3 Literature Review

The system analyzed in this work is subjected to four different type of loads: aerodynamic loads, hydrodynamic loads, mooring line loads and ice loads. We will now introduce each of these loads, with reference to the theoretical model used by SIMA, which will be used for the simulation. After introducing the loads, the coupled analysis theory will be presented as this will be used to combine them.

3.1 Aerodynamic Loads

3.1.1 Wind Model

Aerodynamic loads are caused by wind, which varies both in short and long terms, but short term variation are those of interest for wind turbines. These variations occurs typically in three different ways: spatial variation, temporal variation and turbulence [24]. The most simple method consists in condiering spatial variation only, which is caused by the vertical wind shear. This phenomena is caused by the boundary layer which is formed on the sea surface and causes the wind speed to increase as the distance from the sea surface increases. Different models exists to account for this phenomena, including constant, linear, logarithmic and power law, but the most commonly used is the latter one [24], shown in Eq. (3.1).

$$U(z) = U_{ref} \left(\frac{z}{z_{ref}} \right)^{\alpha} \tag{3.1}$$

where:

α: vertical shear exponent

U_{ref}: wind speed at reference height z_{ref}

However the effect of wind shear is of minor importance for offshore application [25] and therefore the constant model can be applied.

A more accurate description that is accounted for by SIMA, includes the turbulence description. In this case, the wind is described by a mean speed $\bar{U}$ and a variation over time $u'(t)$:

$$U = \bar{U} + u'(t) \tag{3.2}$$

The turbulent part is a randomly defined process and therefore it is described by stochastic tools.

3.1.2 Rotor - BEM Theory

Aerodynamic loads on the wind turbine rotor can be modeled using different models, that differs in complexity and simplification assumptions. SIMA relies on the Blade Element Momentum (BEM) theory [26], which is one one of the most widely used [27] because it is a relatively simple model that provides accurate results, especially when the different correction that will be presented here are applied and when accurate description on the airfoil is available.

In order to describe the BEM theory, we need to start by briefly describing the 1D momentum theory. 1D momentum theory considers the control volume shown in Figure 3.1 and assumes the following: homogeneous, incompressible steady-state fluid flow, no frictional drag, no flow thorough the steam tube boundary, infinite blades, uniform trust over disk, pressure equal to ambient pressure far from disk and non-rotating wake.

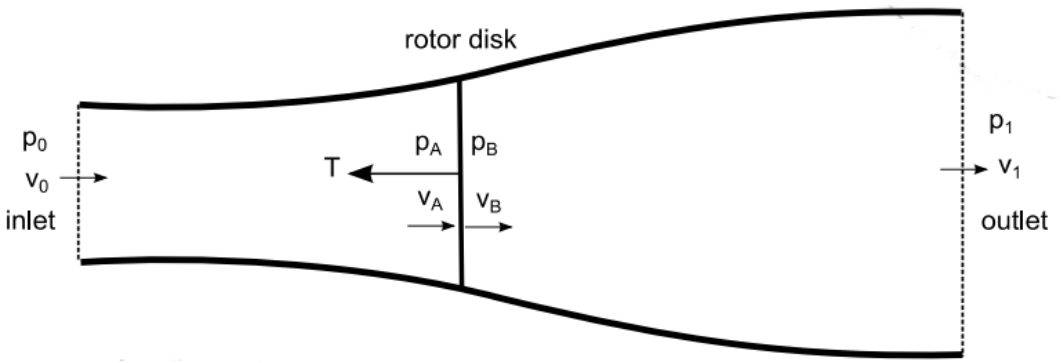

Figure 3.1: 1D momentum theory control volume [24]

With reference to the variables name defined in Figure 3.1, assuming that $p_0 = p_1$ and that $v_A = v_B$, the mass conservation yields:

$$\dot{m} = \rho_a A_0 v_0 = \rho_a A_1 v_1 = \rho A v_A = \rho_a A v_B \tag{3.3}$$

where ρ_a is the density of air, A_0, A_1 and A are the inlet, outlet and disk area respectively. If T is the thrust that the disk apply on the flow, the conservation of momentum gives:

$$T = \dot{m}(v_0 - v_1) \tag{3.4}$$

while applying the Bernoulli equation from inlet to the disk and from the disk to the outlet, we get the following two relations:

$$p_0 + \frac{1}{2}\rho v_0^2 = p_A + \frac{1}{2}\rho v_A^2 \tag{3.5}$$

$$p_B + \frac{1}{2}\rho v_B^2 = p_1 + \frac{1}{2}\rho v_1^2 \tag{3.6}$$

the thrust T can be also evaluated as the difference between the pressure forces due to p_A and p_B, which gives:

$$T = A(p_A - p_B) \tag{3.7}$$

if we solve Eq. (3.5) and Eq. (3.6) for p_A and p_B respectively and substitute these into Eq. (3.7) we get another expression for T:

$$T = \frac{1}{2}\rho_a A(v_0^2 - v_1^2) \tag{3.8}$$

we can now combine Eq. (3.4) and (3.8), to find an expression for v_A as a function of v_0 and v_1

$$v_A = \frac{1}{2}(v_0 + v_1) \tag{3.9}$$

and define the axial induction factor a as:

$$a = \frac{v_0 - v_A}{v_0} \tag{3.10}$$

which means that the wind velocity at the disk is given by

$$v_A = v_0(1 - a) \tag{3.11}$$

by combining Eq. (3.9) and (3.11) we find an expression for the speed at the outlet:

$$v_1 = v_0(1 - 2a) \tag{3.12}$$

finally, we can combine Eq. (3.8) and (3.12) to express the thrust force as a function of known variables

$$T = 2\rho_a A v_0^2 a(1 - a) \tag{3.13}$$

The next step consists in removing the last assumption, i.e. we now consider the rotating wake. In fact, the conservation of angular momentum tells us that if the rotor rotates, the downwind wake need to rotate too [28]. In order to do that, we start by discretizing the the rotor into a number of annular elements of height dr, as shown in Figure, and by assuming that there is no radial dependency and that the force from the blades on the flow is constant in each annular element.

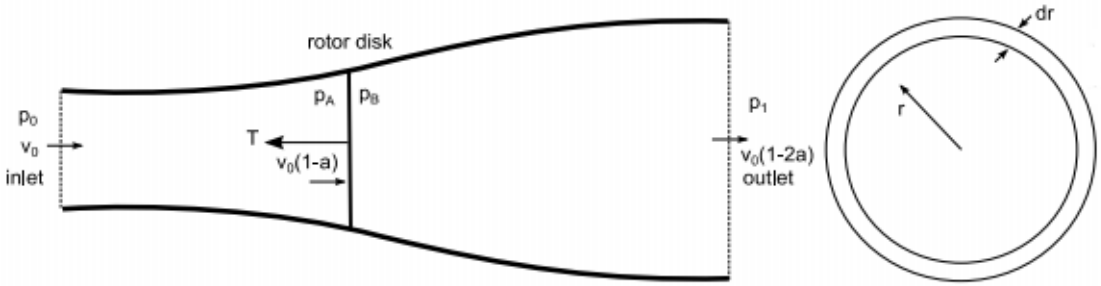

Figure 3.2: 1D momentum theory control volume as annular element [24]

It can be proven [24]that the pressure drop at the rotor disk can be written as

$$p_B - p_A = \rho_a(\Omega + \frac{1}{2}\omega)\omega r^2 \tag{3.14}$$

where Ω is the rotor rotational speed and ω is the wake rotational speed. Combining Eq. (3.7) applied to one annular element with Eq. (3.14) and introducing the angular induction factor a' we get

$$\begin{aligned} a' &= \frac{w}{2\Omega} \\ dT &= \frac{1}{2}\rho_a \Omega^2 4a'(1 + a')2\pi r^3 dr \end{aligned} \tag{3.15}$$

The conservation of angular momentum implies that the torque dQ applied by the annular element is equal to change in angular moment of the wake, but since the wake has no angular velocity until it reach the rotor, this change will be equal to the angular momentum in b:

$$dQ = \rho_a v_A 2\pi r^3 \omega dr \tag{3.16}$$

finally, we can use the relation for v_A and ω as a function of a and a' respectively, to get the following expression for the torque

$$dQ = 4\rho_a \Omega v_0 a'(1 - a)\pi r^3 dr \tag{3.17}$$

moreover, we can apply Eq. (3.13) to the annular control volume which has area $A = 2\pi r dr$

$$dT = 4\rho_a v_0^2 a(1 - a)\pi r dr \tag{3.18}$$

Until now, we consider as if the rotor had an infinite number of blades. However, actual rotors of course have a finite number of blade B and each of them will provides a thrust and a torque such that the sum over the blade will be equal to the thrust and torque given in Eq (3.18) and (3.17) respectively. In order to define these force and torque, we have to apply the blade element theory which account for 3D effect and for the fact that we have a finite number of blades [24].

The local flow past a section of wind turbine blade shown in Figure 3.3 generates a lift force L and a drag force D perpendicular to each other and such that the drag has the same direction as the relative velocity v_{rel} between the wind and the blade element. Note that L and D are here defined as forces acting on the considered section, not on the entire blade.

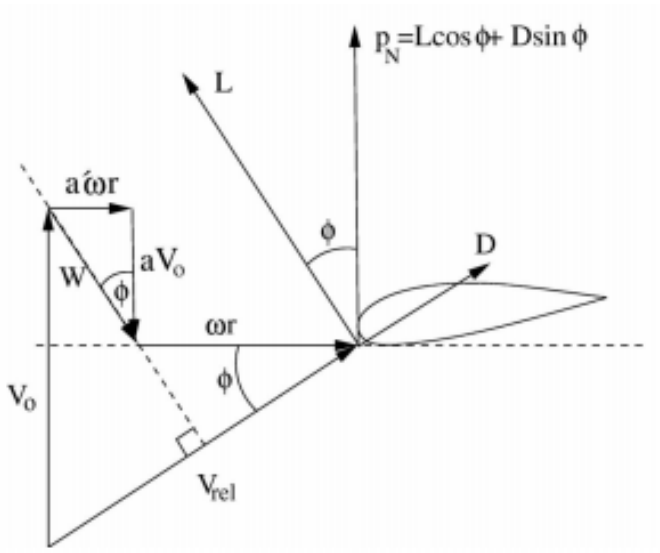

Figure 3.3: Flow past a blade element [24]

The total thrust acting on an annular element, is given by the local normal force P_N on each blade times the number of blades times the length of the blade element

$$dT = BP_N dr = B(L\cos\phi + D\sin\phi)dr \tag{3.19}$$

where ϕ is the flow angle. in the same way we can define the tangential force P_T as

$$P_T = L\sin\phi - D\cos\phi \tag{3.20}$$

and evaluate the corresponding torque

$$dQ = BrP_T dr = Br(L\sin\phi - D\cos\phi)dr \tag{3.21}$$

Finally, we can impose Eq. (3.18) to be equal to Eq. (3.19) and Eq. (3.17) to be equal to Eq. (3.21) to get two expressions for a and a'

$$a = \left(\frac{4F\sin^2\phi}{\sigma C_N} + 1\right)^{-1} \tag{3.22}$$

$$a' = \left(\frac{4F\sin\phi\cos\phi}{\sigma C_T} - 1\right)^{-1} \tag{3.23}$$

where:

$\sigma = \frac{Bc}{2\pi r}$ is the solidity ratio

c is the chord length

$C_N = C_L \cos\phi + C_D \sin\phi$ is the normal force coefficient

$C_T = C_L \sin\phi - C_D \cos\phi$ is the tangential force coefficient

$C_L = \frac{L}{0.5\rho_a V_{rel}^2 c}$ is the lift force coefficient

$C_D = \frac{D}{0.5\rho_a V_{rel}^2 c}$ is the drag force coefficient

F is Prandtl correction factor

The Prandtl tip loss correction factor F account for the fact that the air tends to flow around the tip of each blade and that therefore the flow becomes more three-dimensional as we get close to tip [24]. It can be computed with the following formula:

$$F = \frac{2}{\pi} \arccos\left(e^{-\frac{B(1-r/R)}{2r\sin\phi/R}}\right) \tag{3.24}$$

where R is the radius of the rotor.

In addition to the tip loss correction, SIMA accounts for two more corrections [26]: dynamic wake and dynamic stall. The former accounts for the fact that when the turbine blades are pitched, it takes some time for the wake to become steady again and therefore the real power output from the turbine after the the blades have been pitched does not match the value we get by using the BEM model [24]. The latter considers change in lift and drag due to the dynamic changes of angle of attack.

Another important correction that need to be done before proceeding with the BEM solution, is the tower shadow effect. This effect accounts for the fact the tower modifies the air flow and therefore every time a blade approach the vertical downward positions, it passes through a region of modified flow thus resulting in a modified thrust and torque [24]. This effect is accounted for by the use of the influence factors u and v for the longitudinal and transverse velocity respectively.

Once all the equations have been defined, the actual BEM solution procedure can be performed. This procedure is iterative (as shown Figure 3.4) and it begins by guessing values for the induction factors a and a'. Once the convergence is reached, Eq. (3.18) and (3.17) can be used to evaluate thrust and torque.

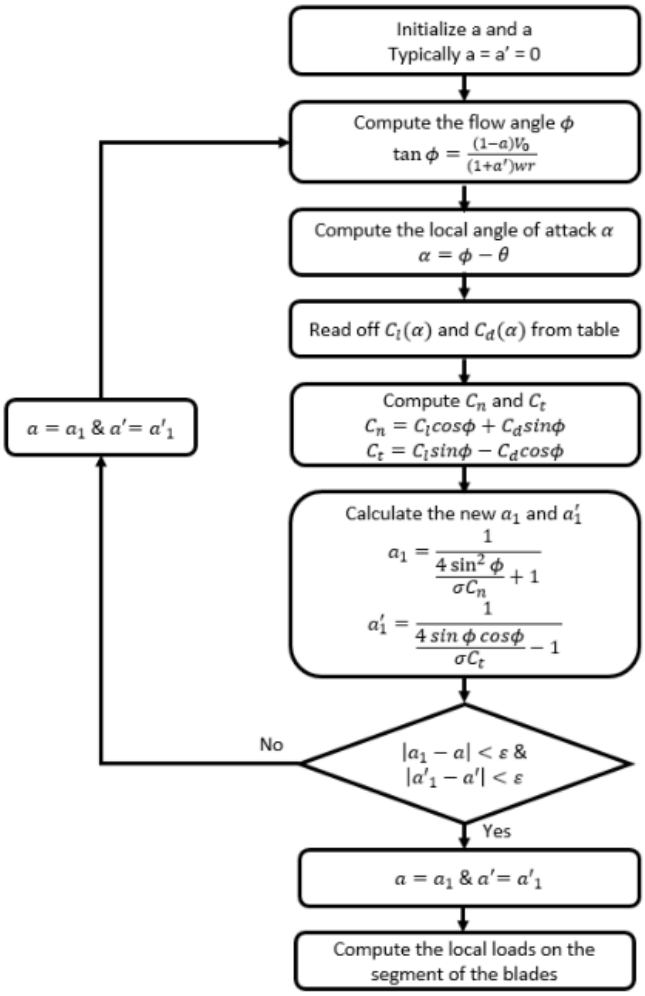

Figure 3.4: BEM solution procedure flowchart [29]

Since we are aiming to perform a coupled analysis, the motion of the platform and the deformation of the blades should be taken into account, since they can modify the results from Eq. (3.18) and (3.17). This coupling is performed by SIMA and will be presented later.

3.1.3 Tower and Nacelle - Drag Force

In addition to the rotor load, the wind generates a loads on the tower and on the nacelle, which are due to the drag force. The drag force dF acting on a section of the tower with height z, can be evaluated through the pressure integration method coupled to the Morison's equation [30]:

$$d\mathbf{F} = \frac{1}{2}\rho_a C_D D(z) dz[\mathbf{U}(z,t)|\mathbf{U}(z,t)|] \tag{3.25}$$

where:

C_D is the viscous drag coefficient

D is the tower diameter at the considered height

$\mathbf{U}(z,t)$ is the relative velocity between the tower and the wind at the considered height

The total force acting on the tower at a general instant t is then obtained by integrating Eq. (3.25) over the tower height. Since $\mathbf{U}$ is the relative velocity between tower and wind, the coupling between drag force and tower motion has a very strong effect, since the tower experience higher aerodynamic loads when is oscillating against the wind direction. Once again, this coupling effect is taken into account by SIMA.

3.2 Hydrodynamic Loads

Hydrodynamic loads on the floater body of a semi-submersible floating wind turbines are wave loads which can be analyzed through the linear potential theory and non-linear theory. We will now present the two theories with respect to their application for the given problem.

3.2.1 Linear Floater Hydrodynamics

Let us start by analyzing the governing equations and the main assumption of the potential flow theory [31].

The main assumptions of the potential flow theory regards the fluid, which must be inviscid, irrotational and incompressible. Combining this assumptions with the linear theory we get the governing equation for the velocity potential ϕ of the fluid due to the interaction of a body moving with velocity $\mathbf{V}_B$ and linear waves:

$$\nabla^2\phi = 0 \tag{3.26}$$

Eq. (3.26) is valid in the body volume, while the following boundary conditions are valid on the sea bottom, body surface and free surface respectively

$$\frac{\partial\phi}{\partial n} = 0 \tag{3.27}$$

$$\frac{\partial\phi}{\partial n} = \mathbf{V}_b \cdot \mathbf{n} \tag{3.28}$$

$$\frac{\partial^2\phi}{\partial t^2} + g\frac{\partial\phi}{\partial z} = 0 \tag{3.29}$$

where $\mathbf{n}$ is the normal vector pointing into the fluid and z is the vertical coordinate with respect to the free surface.

The so-defined velocity potential can be used to evaluate the external load acting on the surface of the floater body. Considering one of the six degrees of freedom, we get the force as the sum of two integrals: the dynamic pressure integrated over the mean body surface S_{0B} and the static pressure integrated over the instantaneous body surface S_B

$$F_j(t) = \int_{S_{0B}} -\rho_w \frac{\partial\phi}{\partial t}\mathbf{n}dS + \int_{S_B} -\rho_w g z\mathbf{n}dS \tag{3.30}$$

The linear wave body interaction problem for large volume floater can be split into the diffraction and radiation problem. The former considers the interaction of a fixed body with the incident waves, while the latter consider how the body motion in its 6 dofs interact with still water with no incident waves.

$$\phi(x,y,z,t) = \phi_0(x,y,z,t) + \phi_D(x,y,z,t) + \phi_R(x,y,z,t) \tag{3.31}$$

where the diffraction problem consists in integrating ϕ_0 and ϕ_D (which represents incident waves and diffraction respectively) to find the wave excitation loads $F_j^{exc}(t)$. While the radiation problem consists in integrating ϕ_R to get the added mass, potential damping and restoring forces.

We introduce the equation

$$\phi_R(x,y,z,t) = \Re\left\{\sum_{k=1}^{6} \dot{\eta}_k \varphi_k(x,y,z)\right\} \tag{3.32}$$

where η_k is the kth body motions and φ_k is the complex spatial velocity potential for the body oscillating with unitary speed in the kth dof. It can be shown that Eq. (3.30) can be written into:

$$F_j(t) = \sum_{k=1}^{6} F_j^{exc}(t) - A_{jk}\ddot{\eta}(t) - B_{jk}\dot{\eta}(t) - C_{jk}\eta(t) \tag{3.33}$$

where A_{jk}, B_{jk} and C_{jk} are added mass, potential damping and linear restoring coefficients respectively

$$A_{jk} = \Re\left\{\rho_w \int_{S_{0B}} \varphi_k \eta_j dS\right\} \tag{3.34}$$

$$B_{jk} = -\omega\Im\left\{\rho_w \int_{S_{0B}} \varphi_k \eta_j dS\right\} \tag{3.35}$$

which allow us the write the equation of motion for the linear wave structure interaction problem in matrix form as

$$(\mathbf{M} + \mathbf{A}(\omega))\ddot{\boldsymbol{\eta}} + \mathbf{B}(\omega)\dot{\boldsymbol{\eta}} + \mathbf{C}\boldsymbol{\eta} = \mathbf{F}^{exc} \tag{3.36}$$

Assuming the system to be linear and at steady state condition, the response will have the same frequency of the excitation and its amplitude will be proportional to the excitation. Assuming that the excitation load is proportional to the wave amplitude ξ_a and that oscillates with frequency ω we can write it into complex form as

$$\mathbf{F}^{exc}(t) = \Re\left\{\xi_a \mathbf{X}(\omega,\beta)e^{i\omega t}\right\} \tag{3.37}$$

and similarly the response

$$\boldsymbol{\eta}(t) = \Re\left\{\boldsymbol{\eta}_a(\omega)e^{i\omega t}\right\} \tag{3.38}$$

We can therefore re-write Eq. (3.36) in frequency domain

$$(-\omega^2(\mathbf{M} + \mathbf{A}(\omega)) + i\omega\mathbf{B}(\omega) + \mathbf{C})\boldsymbol{\eta}_a(\omega) = \xi_a \mathbf{X}(\omega,\beta) \tag{3.39}$$

3.2.2 Non-Linear Floater Hydrodynamics

In addition to first order loads, semi-submersible are subjected to second order loads due to the low drift motions caused by slowly-varying (slow drift) loads connected with second order difference frequency effect and mean drift effect.

Different methods exists for evaluating the force on a marine structure, but the two most widely used are the direct pressure integration and the conservation of fluid momentum

[24]. The latter is generally more complicated, but in the case of a horizontal mean drift force calculation it becomes more simply and yields more accurate results.

An expression for the low frequency second order force is [32]:

$$\mathbf{F}^{(2)} = \oint_{WL} \frac{1}{2}\rho_w g \left(\xi_r^{(1)}\right)^2 \mathbf{n} dl - \int_{S_{0B}} \frac{1}{2}\rho_w \left(\nabla\phi^{(1)}\right)^2 \mathbf{n} dS - \int_{S_{0B}} \rho_w \boldsymbol{\eta}^{(1)} \nabla \frac{\partial \phi^{(1)}}{\partial t} \mathbf{n} dS$$
$$- \mathbf{M}\mathbf{R}^{(1)}\boldsymbol{\eta}_G^{(1)} - \int_{S_{0B}} \rho_w \frac{\partial \phi^{(2)}}{\partial t} \mathbf{n} dS \tag{3.40}$$

where $^{(1)}$ and $^{(2)}$ refers to first and second order quantities respectively, while $\mathbf{R}$ is the rotation matrix. We can see that the force can be split into five components: first order wave relative elevation, pressure drop due to first order velocity, pressure drop due to product of gradient of first order pressure and first order motion, first order angular motions and inertia forces, second order potential.

The first four components represent quadratic contribution of the first order solution, while the last component is the contribution from the second order potential, which is the most challenging one to solve.

Eq. (3.40) can be rewritten as:

$$F_j^{(2)} = \Re\left\{\sum_m \sum_n \xi_m \xi_n T_{mn}^j(\omega_m, \omega_n) e^{-i(\omega_m - \omega_n)t + (\epsilon_m - \epsilon_n)}\right\} \tag{3.41}$$

where $T_{mn}^j(\omega_m, \omega_n)$ is the quadratic transfer function (QTF), i.e. the complex difference frequency second order transfer function, which is used by SIMA to compute the second order hydrodynamic forces [26].

However, evaluating the QTF can represent a problem due to the need of computing the second order velocity potential $\phi^{(2)}$. In order to overcome this, different methods exists and the most widely used is Newman's approximation [33]. This method rely on the mean drift forces, which correspond to the diagonal terms of the QTF and depend only on the first order solution, to derive the QTF

$$T_{mn} = T_{nm} = \frac{1}{2}(T_{mm} + T_{nn}) \tag{3.42}$$

which, together with the introduction of a sum frequency term, let us write Eq. (3.41) in a more simple way [30]:

$$F_j^{(2)} = 2\left(\sum_m \xi_m \sqrt{T_{mm}} \cos(\omega_m t + \epsilon_j)\right)^2 \tag{3.43}$$

where the mean drift force and the corresponding transfer function can be estimated by direct pressure integration or simplified conservation of momentum in the horizontal dofs.

Newman's approximation has been proven to be accurate for deep water and for small frequency difference, however, it may yields inaccurate results (up to 30% lower) for small depth ratio (depth/wavelength) and for high frequency difference [34]. Since horizontal motion natural periods for semi-submersible platform is above 100 s, the frequency difference is small and therefore it does not represent a problem in terms of accuracy. On the other hand, shallow waters could be interesting for a semi-submersible floating wind turbine and therefore the reliability of Newman's approximation is uncertain.

3.2.3 Ice-waves Interaction

The hydrodynamics loads described until now apply to any large volume structure floating in open water. In case of ice-covered sea, the hydrodynamics loads need to be modified in order to account for the interaction between waves and ice. The problem is complex and depends on several factors such as the ice strength (both bending and compressive) and the distance from the ice edge [35]. The latter has strong influence but will not be considered in our case, since we are interested in the effect of level ice on the dynamic of a floating wind turbine and because we want to keep the problem simple. One model exists that describe waves under pack ice in terms of dispersion relation [36].

Despite some model exists, they are complex to implement and therefore in this work, we will account for the ice-waves interaction through assuming that waves do not propagate under level ice. This assumption is reasonable because the models that describes this phenomenon agree on the fact that the ice layer results in an attenuation of the waves [35] [36]. In addition to that, ice load are responsible of the most of the energy consumption, thus making the linear hydrodynamic damping negligible [37]. Therefore, the diffraction effects will be neglected as well as the radiation damping. On the other hand, added mass, hydrostatic restoring forces and viscous damping will be considered.

3.3 Mooring Line Loads

Mooring line consists of a number (typically 3 or 4 lines) of catenary line that keep the platform in position. Unlike TLP, semisumbersible platforms do not gain stability thanks to the mooring lines. The mooring system provides stiffness to the platform from a rigid body motion perspective, since it provides forces that tend to bring the platform back in position as this is displaced by wind, wave or currents , hence acting as non-linear springs [24].

Considering a catenary line, as shown in Figure 3.5, and assuming that only gravity and buoyancy forces are acting and that the lines remain in an xy plane, the static governing equations reads (with respect to the load depicted in Figure 3.6:

$$(\mathbf{T} + \Delta\mathbf{T})\cos(\phi + \Delta\phi) - \mathbf{T}\cos(\phi) = \mathbf{0} \tag{3.44}$$

$$(\mathbf{T} + \Delta\mathbf{T})\sin(\phi + \Delta\phi) - \mathbf{T}\sin(\phi) - \mathbf{wds} = \mathbf{0} \tag{3.45}$$

where $\mathbf{T}$ is the tension, ϕ is the angle with the seabed, $\mathbf{w}$ is the specific weight and $\mathbf{ds}$ is the element length.

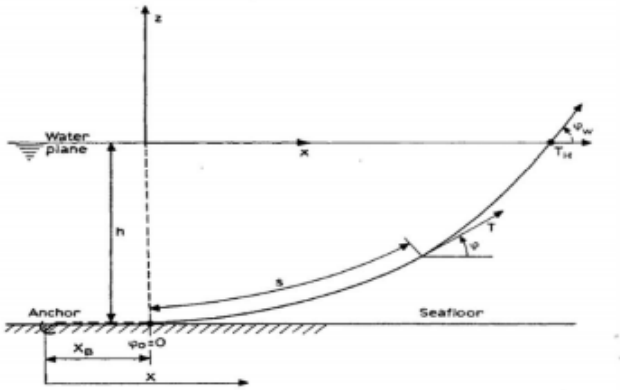

Figure 3.5: Catenary line scheme [24]

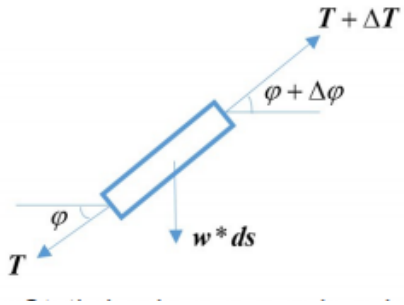

Figure 3.6: Static loads on a mooring element[24]

As the platform is displaced away from its equilibrium position, an horizontal force will start to develop and will produce a restoring effect on the platform motions. This effect can be evaluated as:

$$K = \frac{\Delta F_x}{\Delta X} \tag{3.46}$$

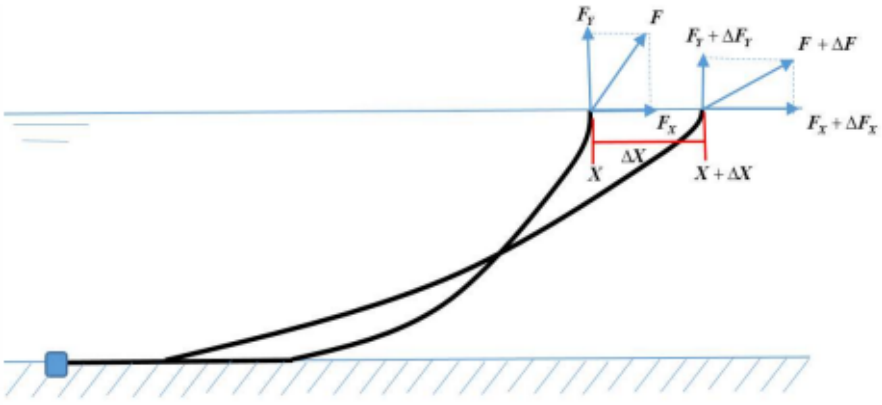

Figure 3.7: Catenary line scheme restoring effect[24]

In the case of a dynamic analysis Eq: (3.44) and (3.45) need to be modified to account for inertia and hydrodynamic loads too, as represented in Figure 3.8. Here $\mathbf{F}_n$ and $\mathbf{F}_t$ represent the hydrodynamic forces in normal and tangential direction, while $\mathbf{a}_n$ and $\mathbf{a}_t$

are acceleration in normal and tangential direction respectively. Solving the Dynamic equations obtained through this analysis it is possible to determine the mooring load, that need to be considered in the coupled analysis.

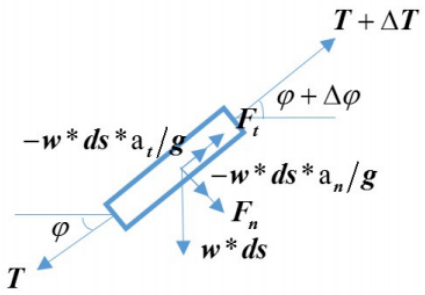

Figure 3.8: Dynamic loads on a mooring element [24]

The main effects of the mooring lines, can be divided into 4 categories: weight, stiffness, inertia and damping. Weight effect consists in the vertical loads induced by the weight of the catenary. Stiffness effect affect the the natural period of the platform rigid body motions; surge say and yaw are the motions that suffer this influence the most. Inertia effects depends on the fact that the mooring line elements will change the fairlead mooring line tension. Damping effect is mainly related to slowly varying motions of the platform, that will suffer the damping effect from the mooring lines.

3.4 Ice Loads

Ice loads can occurs in different ways and conditions, including level ice, brash ice, ridges and icebergs. In this work, only level ice loads will be considered. Ice loads due to level ice can be analyzed according to different standards depending on the application. When offshore wind turbines are to be considered ISO/FDIS 19906, 2019 [38] is the most suitable [39].

Ice loads on offshore floating structure are due to the compression that occurs when drifting ice is pushed towards the side of the structure by wind, currents and waves. The loads depends on the failure mechanism of the ice, both in terms of load frequency and amplitude. Therefore, knowing how the ice fail in the given circumstances is fundamental in order to estimate the load and corresponding response. Once the failure mechanism is known, it is possible to apply a numerical model that allows us to determine the load acting on the structure in different ice thicknesses.

Ice failure under compression can occur in different ways, depending on the structure geometry and on the ice properties i.e. thickness, velocity, temperature and presence of ridges. Sea ice can fail in the following modes: creep, crushing, bending, buckling and splitting. Since the structure we are considering is designed to have a conical shape at the mean sea level, the main failure mode will be bending [38] [40] [41]. In fact, due to the inclined contact surface between the ice and the structure, a vertical component arise that generate a bending moment leading to the ice bending failure [42]. This method is widely used in the offshore industry because loads due to bending are usually less intense than loads due to crushing, since ice crushing strength is higher than bending strength. Because of these considerations, only bending failure will be considered in this analysis.

3.4.1 Ice Bending Failure

Bending failure process of ice is shown in Figures 3.9 and 3.10. As can be seen from the latter one, the effect of rubble ice piling-up can represent a problem for sloping structure, because it can create a vertical surface against which the ice will start failing trough crushing, thus resulting in an increased load. This effect is less severe on upward-breaking conical structure, due to clearing of rubble ice [38]. In this analysis a conical structure will be considered since this is the most obvious choice due to the shape of the semi-submersible platform column, therefore the piling-up effect will not be considered.

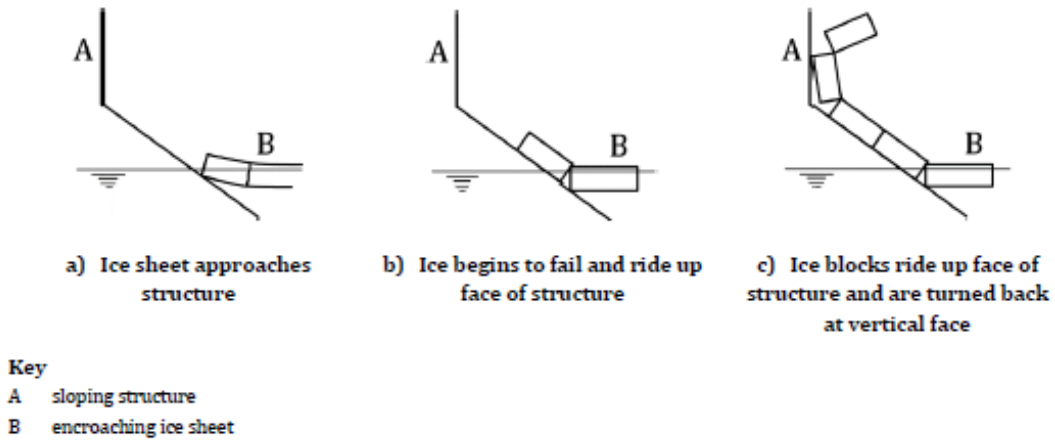

Figure 3.9: Process in the interaction between a sloping structure and sheet ice [38]

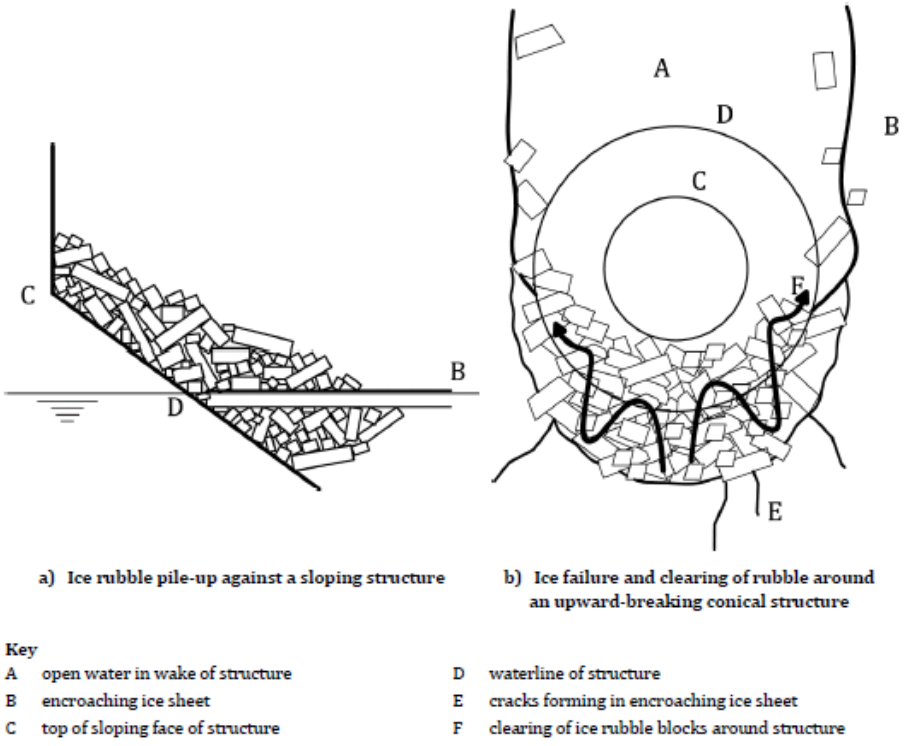

Figure 3.10: Ice rubble pile-up and clearing around a sloping structure [38]

When an ice sheet approaches a slope cone the loading cycle shown in Figure 3.11 occurs. After the first contact, the load starts growing (1) until the vertical component reaches the bending strength of ice and the ice breaks. Then, the unloading process starts (2) that lasts for a longer period than the loading, during which the velocity of the ice pieces decrease as they ride on the cone. Finally, the no load phase occurs (3) when the rubble ice is cleared away until the new contact starts.

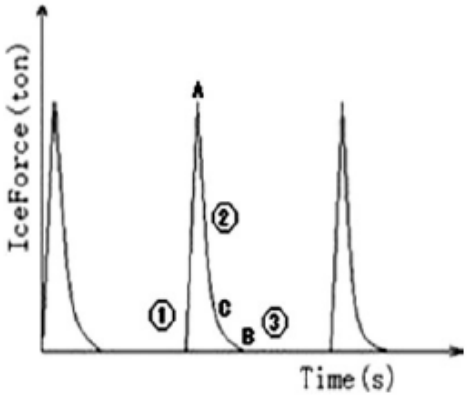

Figure 3.11: Ice force variation during the interaction between the ice and the cone [40]

The loading process can be described in a simplified 2-dimensional manner by Figure 3.12. The horizontal and vertical components of the load are respectively given by [38]:

$$F_H = N \sin\alpha + \mu N \cos\alpha \tag{3.47}$$

$$F_V = N \cos\alpha - \mu N \sin\alpha \tag{3.48}$$

moreover, the relationship between vertical and horizontal component is:

$$F_V = \frac{F_H}{\xi} \tag{3.49}$$

where

$$\xi = \frac{\sin\alpha + \mu \cos\alpha}{\cos\alpha - \mu \sin\alpha} \tag{3.50}$$

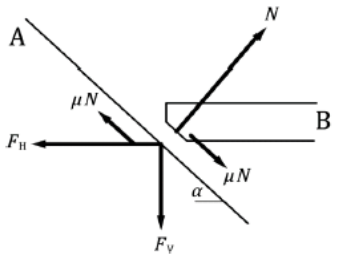

Key

A	sloping face of structure	α	slope of structure face from horizontal
B	encroaching ice sheet	F_H	horizontal component of ice action
N	normal component of reaction to ice action on structure	F_V	vertical component of ice action
μ	ice-structure friction coefficient		

Figure 3.12: Ice action components on a sloping structure for a two-dymensional condition [38]

This cyclical ice breaking process will lead to ice-induced vibration on the structure, which are usually less severe than those occurring on vertical sided structure [41]. Three types of vibrations can occur on conical shaped structures [41]: damping vibration under quasi-static ice force, steady state vibration under ice-excited force and highly random vibration under random ice force. All three of these vibrations can occur, but the most relevant one will depends on the dynamic properties of the structure. Therefore, a dynamic analysis need to be conducted in order to avoid that the ice load frequency match the structure natural frequency, in order to avoid resonance.

Different methods exists to determine ice actions on cones, but the two most relevant for offshore structures, i.e. those used in the considered standard, are based on the theory of plasticity and on the elastic beam bending [38] and will be presented here. Another method commonly employed is the Ralston's method [39] [43]. All these methods are valid for both upward and downward breaking cone structures.

3.4.2 Plastic Method for Cones

This model is based on a limit analysis solution and considers actions due to the flexural failure of the ice sheet and the ride-up actions due to ice pieces. The following derivations is valid for an upward breaking cone but can be applied to a downward-breaking cone if the ice density ρ_i is replaced with $(\rho_w - \rho_i)$ where ρ_w is the water density.

First of all, the following functions are defined:

$$f = \sin\alpha + \mu E_1 \cos\alpha \tag{3.51}$$

$$g_r = \frac{\sin\alpha + \frac{\alpha}{\cos\alpha}}{\frac{\pi}{2}\sin^2\alpha + 2\mu\alpha\cos\alpha} \tag{3.52}$$

$$h_v = \frac{f\cos\alpha - \mu E_2}{\frac{\pi}{4}\sin^2\alpha + \mu\alpha\cos\alpha} \tag{3.53}$$

$$W = \rho_i g h_r \frac{w^2 - w_t^2}{4\cos\alpha} \tag{3.54}$$

$$\tag{3.55}$$

where α is the slope of the structure, w_t is the top diameter of the cone, w is the waterline diameter of the cone and h_r is the ice ride-up thickness. The parameter E_1 and E_2 are elliptical integrals defined by:

$$E_1 = \int_0^{\frac{\pi}{2}} (1 - sin^2\alpha \sin^2\eta)^{-\frac{1}{2}} d\eta \tag{3.56}$$

$$E_2 = \int_0^{\frac{\pi}{2}} (1 - sin^2\alpha \sin^2\eta)^{\frac{1}{2}} d\eta \tag{3.57}$$

$$\tag{3.58}$$

where η is an angular integration parameter.

Now, the horizontal and vertical ride up and breaking actions can be determined. Note that a single sheet thickness is assumed

$$H_R = W\frac{\tan\alpha + \mu E_2 - \mu f g_r \cos\alpha}{1 - \mu g_r} \tag{3.59}$$

$$V_R = W\cos\alpha\left(\frac{\pi}{2}\cos\alpha - \mu\alpha - f h_V\right) + H_R h_V \tag{3.60}$$

$$H_B = \frac{\sigma_f h^2 \tan\alpha}{3(1-\mu g_r)}\left(\frac{1 + Y x \ln x}{x-1} + G(x-1)(x+2)\right) \tag{3.61}$$

$$V_B = H_B h_V \tag{3.62}$$

where σ_f is the flexural strength of ice, Y depends on the yielding model used while G and x are given by:

$$G = \frac{\rho_i g w^2}{4\sigma_f h} \tag{3.63}$$

$$x = 1 + \sqrt{3G + \frac{Y}{2}} \tag{3.64}$$

The total ice loads are simply evaluated by summing up the the breaking and piling up components:

$$F_H = H_B + H_R \tag{3.65}$$

$$F_V = V_B + V_R \tag{3.66}$$

$$\tag{3.67}$$

3.4.3 Elastic Method for Cones

This method relies on one of the most commonly used model for ice sheet bending, i.e. the elastic beam on elastic foundation. Once again, the method is derived for upward-breaking cone, but can be applied to downward breaking cone by replacing the ice weight with the ice buoyancy in water. Figure 3.13 shows the general configuration of the model.

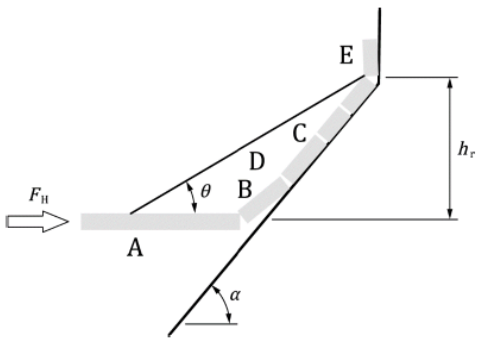

Key

A	advancing ice	F_H	horizontal ice action
B	ice is lifted and failed in bending on slope	α	slope of face of structure from horizontal
C	ice pushed up slope through rubble	θ	rubble angle from horizontal
D	ice rubble	h_r	ride-up height
E	blocks turned at top of slope		

Figure 3.13: General configuration of ice action on a sloping structure [38]

The horizontal component F_H is evaluated as the sum of 5 components multiplied by the correction factor I_P that accounts for the in-plane compression in the ice sheet due to F_H by increasing the effective flexural strength:

$$F_H = (H_B + H_R + H_P + H_L + H_T)I_P \tag{3.68}$$

let us analyze each component separately.

H_B is the horizontal component of the ice-breaking action, given by:

$$H_B = \xi V_B \tag{3.69}$$

where ξ is defined at Eq. (3.50), while V_B is the larger between the first break action V_{B1} and the second break action V_{B2}. Horizontal load need to be evaluated using both actions (calculated according to the formulas provided in the standard [38]) and than the larger one has to be selected. The action to create the first break is simply the one for a semi-infinite elastic beam on elastic foundation [38], while the action to create the second break is based on an improved method that avoid the over-estimation of the load [44].

H_R is the horizontal component of the action to push the ice blocks up the slope and it is given by:

$$H_R = w_R P \frac{1}{\cos\alpha - \mu \sin\alpha} \tag{3.70}$$

where

$$P = 0.5(\mu_i + \mu)\rho_i g(1-e)h_r^2 \cos\alpha \cot\alpha \left(1 - \frac{\tan\theta}{\tan\alpha}\right) + h_r h \rho_i g(1 + \mu\cot\alpha) \tag{3.71}$$

where w_R is the average of waterline width and width at the top of the slope, μ_i us the ice to ice friction coefficient, e is the porosity of rubble ice and θ is the angle the ice rubble makes with the horizontal.

H_P is the action required to push the ice sheet through the rubble ice and it is given by:

$$H_P = w h_r^2 \mu_i \rho_i g(1-e) \left(1 - \frac{\tan\theta}{\tan\alpha}\right)^2 \frac{1}{2\tan\theta} \tag{3.72}$$

where w is the approximated average width of the rubble on the cone.

H_L is the is the horizontal component of the action required to lift the ice rubble on top of the advancing ice sheet and is given by:

$$\begin{aligned} H_L =& 0.5 w h_r^2 \rho_i g(1-e)\xi \left(\frac{1}{\tan\theta} - \frac{1}{\tan\alpha}\right)\left(1 - \frac{\tan\theta}{\tan\alpha}\right) + \\ &+ 0.5 w h_r^2 \rho_i g(1-e)\xi \tan\phi \left(1 - \frac{tan\theta}{\tan\alpha}\right)^2 + \xi c w h_r \left(1 - \frac{\tan\theta}{\tan\alpha}\right) \end{aligned} \tag{3.73}$$

where c is the cohesion of the ice rubble and ϕ is the friction angle of the ice rubble.

H_T is the horizontal component of the action to turn the ice block at the top of the slope and it is given by:

$$H_T = \frac{n}{2} h^2 \rho_i g w_t \frac{\cos\alpha}{\sin\alpha - \mu\cos\alpha} \tag{3.74}$$

where w_t is the larger between the shaft width at the top of the slope and the block width and n is the ration of the ice piece length to its thickness.

3.5 Coupled Analysis

As already described in previous sections, a semisubmersible floating wind turbine gain its buoyancy from the pontoons that constitute the structure and it is kept in position by the mooring lines. In this analysis, the dynamic of the structure will be analyzed in terms of rigid body motion since we will be performing a global coupled analysis. In fact, the floater will be treated as a rigid body and deformation will not be considered. On the other hand, turbine blades and mooring lines will be treated as beams elements.

In frequency domain, the equation of rigid body motion can be written as [24]:

$$-\omega^2(\mathbf{M}+\mathbf{A}(\omega))\mathbf{x}(\omega)+i\omega\mathbf{B}(\omega)\mathbf{x}(\omega)+\mathbf{C}\mathbf{x}(\omega)=\mathbf{F}^{exc}(\omega) \tag{3.75}$$

Where $\mathbf{M}$ is the structural mass matrix, $\mathbf{A}$ is the added mass matrix, $\mathbf{B}$ is the damping matrix, $\mathbf{C}$ is the restoring force matrix and $\mathbf{F}^{exc}$ is the total excitation force, i.e. the combination of wind and ice loads.

Added mass and linear damping can be rewritten as

$$\mathbf{A}(\omega)=\mathbf{a}(\omega)+\mathbf{A}_\infty \tag{3.76}$$

$$\mathbf{B}(\omega)=\mathbf{b}(\omega)+\mathbf{B}_\infty \tag{3.77}$$

by substituting Eq. (3.76) and (3.77) into Eq. (3.75) and applying the Inverse Fourier Transformation, we get the equation of motion in time domain:

$$(\mathbf{M}+\mathbf{A}_\infty)\ddot{\mathbf{x}}(t)+\int_{-\infty}^{+\infty}\mathbf{k}(t-\tau)\dot{\mathbf{x}}(t)d\tau+\mathbf{C}\mathbf{x}(t)=F^{exc}(t) \tag{3.78}$$

The second term of Eq. (3.78) is a convolution integral that represent the wave radiation force vector and k is the retardation function that describes the memory effect of the free surface. Here it should be noticed that in our case, we are considering the dynamic of a floating structure in frozen water, hence the energy dissipated by the linear hydrodynamic damping is negligible with respect to energy consumption due to the ice load [37] and so we can assume $B=0$. However, the analysis will be carried out in general terms at this point.

The retardant function $\mathbf{k}(\tau)$ can be computed by a transform of the frequency dependent added mass and potential damping:

$$\mathbf{k}(\tau)=\frac{1}{2\pi}\int_{-\infty}^{+\infty}(\mathbf{b}(\omega)+i\omega\mathbf{a}(\omega))e^{i\omega t}d\omega \tag{3.79}$$

using the symmetrical properties of $\mathbf{b}$ and $\mathbf{a}$, i.e. $\mathbf{b}(\omega)=\mathbf{b}(-\omega)$ and $\mathbf{a}(\omega)=\mathbf{a}(-\omega)$, we get:

$$\mathbf{k}(\tau)=\frac{1}{\pi}\int_{0}^{+\infty}(\mathbf{b}(\omega)\cos(\omega\tau)d\omega-\omega\mathbf{a}(\omega)\cos(\omega\tau))d\omega \tag{3.80}$$

From causality, we know that the process can not have any memory effect of the future, which means that $\mathbf{k}(\tau)=\mathbf{0}$ for $\tau<0$. This means that the two part of the integral of Eq. (3.80) must be opposite for $\tau<0$ and equal for $\tau>0$:

$$\mathbf{k}(\tau)=\frac{1}{\pi}\int_{0}^{+\infty}\mathbf{b}(\omega)\cos(\omega\tau)d\omega=-\frac{1}{\pi}\int_{0}^{+\infty}\omega\mathbf{a}(\omega)\cos(\omega\tau)d\omega \tag{3.81}$$

From (3.81) we can see that the retardation function can be determined by only one of the two coefficients, potential damping or added mass.

Eq. (3.78) can be determining excitation force vector:

$$\mathbf{F} = \mathbf{F}^{(1)} + \mathbf{F}^{(2)} + \mathbf{F}_{drag} + \mathbf{F}_{mooring} + \mathbf{F}_{wind} + \mathbf{F}_{ice} \tag{3.82}$$

Where $\mathbf{F}^{(1)}$ and $\mathbf{F}^{(1)}$ are the first and second order wave excitation forces. SIMO transforms these wave loads into first and second order transfer functions in order to solve it. Other hydrodynamics actions, such as the nonlinear quadratic drag force, can be added to the equations of motions by using Morison elements in SIMO.

Wind, mooring line and ice loads are evaluated separately by AeroDyn, RIFLEX and Fotran code respectively and added at each time step to the RHS of the equation. In addition to the environmental condition (wind speed and ice drifting speed and thickness), these forces depends on the position of the platform and on its velocity which are updated at every time step based on the forces from the previous time step, thus realizing the coupling between the forces and the platform motion.

After defining the load, Eq. (3.78) is solved in time domain. This is done through an incremental procedure the use the dynamic time integration scheme, according to Newmark β family methods, while the Newton-Raphson iteration is used to assure equilibrium between internal and external forces at every time step.

4 Methods

4.1 Wind Turbine Model in SIMA

The wind turbine model selected for this analysis is the is the DTU 10MW reference wind turbine developed by the department of Wind Energy at Technical University of Denmark (DTU) [45]. It is a 10 MW variable-speed, collective pitch controlled, horizontal axis wind turbine with 3 blades. Its rated wind speed is 11.4 m/s to which correspond a theoretical maximum thrust of 1500 kN; other relevant parameters are shown in Table 4.1, while Figure 4.1 shows the power and thrust curves [45]. In order to investigate the influence of the wind speed on the dynamic of the platform when subjected to combined ice and wind loads, we will use a wind speed equal to $v_w = 12$ m/s; the turbulent wind model described in §3.1.2 will be used.

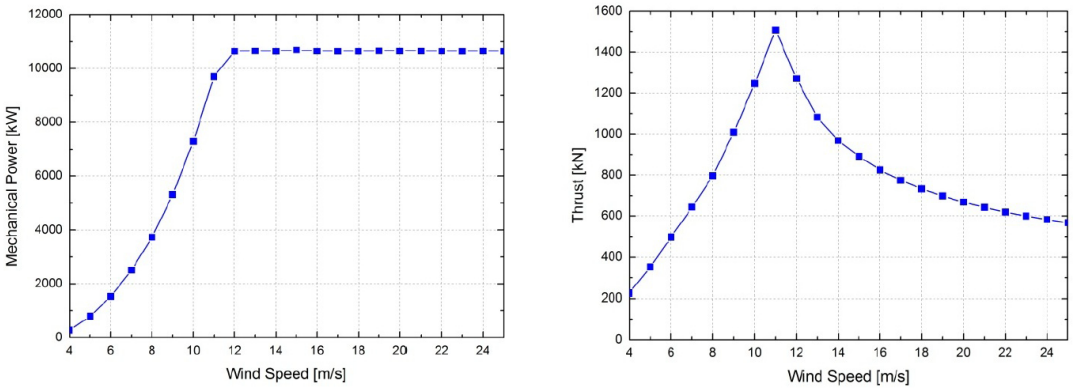

Figure 4.1: Power and thrust curves of the 10 MW wind turbine [45]

Table 4.1: Main parameters of the 10 MW wind turbine

Description	Value	
Rating	10	MW
Configuration	Upwind, 3 blades	
Control	Collective Pitch	
Drivetrain	Multiple stage gearbox	
Rated wind speed	11.4	m/s
Maximum Thrust	1500	kN
Rotor Diameter	178.3	m
Hub Diameter	178.3	m
Hub height	119	m
Tower height	115.63	m
Rotor mass	230	t
Nacelle mass	446	t
Tower mass	628	t
Total mass	1305	t
x position of center of gravity	-0.3	m
y position of center of gravity	0.0	m
z position of center of gravity	85.5	m

The wind turbine is supported by a pontoon-type steel semi-submersible platform which design process is described in greater detail in Qiang Wang's Master's Thesis [19]. The semi-submersible platform floater consists in a 4 column steel pontoons platform which main dimensions are shown in Figure 4.2 and Table 4.2. It should be noted that the model platform columns have vertical sides so they are not fitted with the ice-breaking cone which is assumed for the ice loads calculation. However, the different shape of the columns would only have a minor effect on the hydrodynamic loads acting on the platform. Therefore we can assume that the column have inclined sides when evaluating ice loads, while considering the vertical side model in SIMA. Moreover, the diameter of the breaking cone at the Mean Sea Level (MSL) is assumed to be equal to the columns diameter.

The reference system used to describe the platform and the turbine is the same used in SIMA: the origin is located in the center of the center column, x axis is positive towards one of the side column and z axis points upwards.

The whole structure, wind turbine and floater platform, takes the name of 10 MW CSC. As already mentioned, it is fully modeled in SIMA and a picture of the model is shown in Figure 4.3.

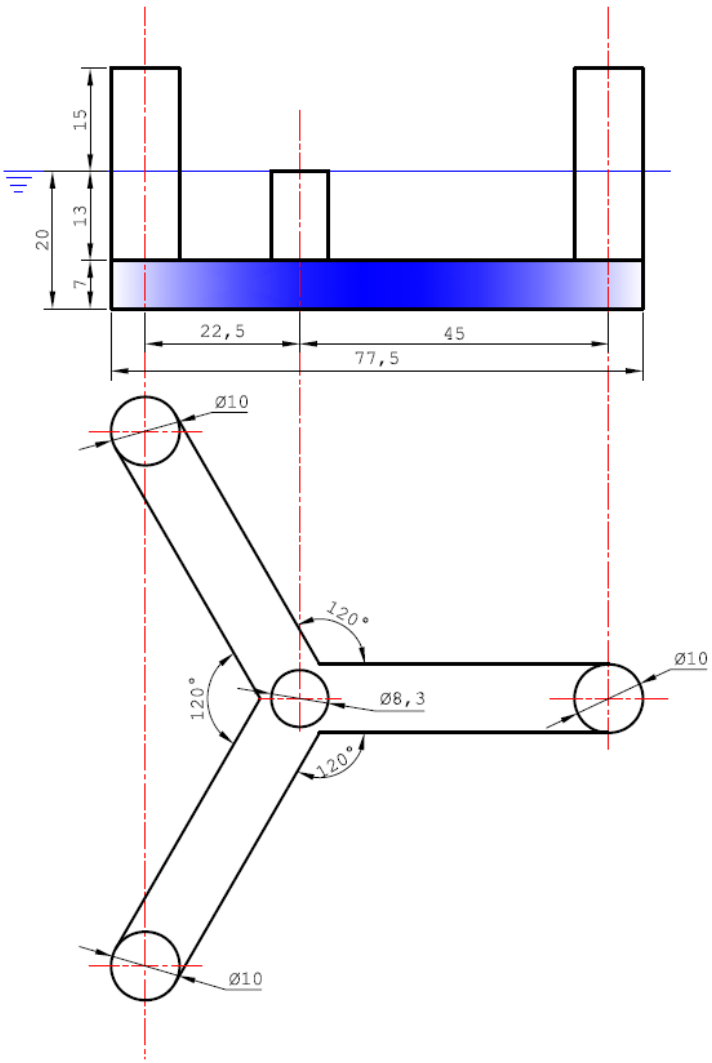

Figure 4.2: Main dimension of the semi-submersible platform [19]

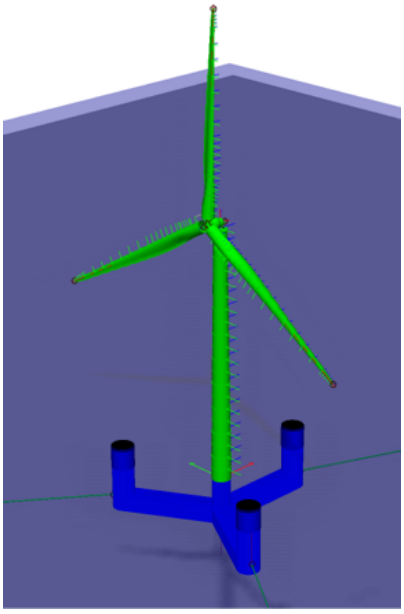

Figure 4.3: The 10 MW CSC semi-submersible floating wind turbine model in SIMA

Table 4.2: Main parameters of the semi-submersible platform

Parameter	Value	
Draft	20.0	m
Freeboard	15.0	m
Center column diameter	8.3	m
Side columns diameter	10.0	m
Side column distance from center	45.0	m
Pontoon height	7.0	m
Pontoon width	10.0	m
Platform mass	2588	t
Wind turbine mass	1305	t
Total mass	3893	t
x position of center of gravity	-0.1	m
y position of center of gravity	0.0	m
z position of center of gravity	22.3	m
Buoyancy	14081	t
x position of center of buoyancy	0.0	m
y position of center of buoyancy	0.0	m
z position of center of buoyancy	-13.8	m
Roll Inertia	$6.41 \cdot 10^9$	kgm^2
Pitch Inertia	$6.41 \cdot 10^9$	kgm^2
Yaw Inertia	$1.18 \cdot 10^{10}$	kgm^2
Sea Depth	200	m
Number of mooring lines	3	
Angle between adjacent lines	120	deg
Radius to anchors from platform center	879.6	m
Unstretched mooring line length	880	m
Pretenion	2190	kN

4.2 Ice Load DLL

SIMA does not have an option to directly introduce ice loads, therefore it has to be provided through an external Dynamic Link Library (DLL). The DLL used in this analysis is based on the one developed by Xian Tan [37] for evaluating ice resistance of ice-breaking ships and it is coded in Fortran. The code was then modified by Marine Saccoman [29] to evaluate ice load on a SPAR buoy working with the software HAWC2. In order to use the DLL to evaluate ice load on a semi-submersible platform with SIMA, we needed to modify the code by Saccoman to solve the compatibility issues between the DLL and SIMA, to ensure convergence and to account for the platform having multiple columns.

4.2.1 Ice Load DLL Description

The ice characteristics were selected following the ISO guidelines [38] regarding ice conditions in the Baltic sea and are listed in Table 4.3. These parameters are kept constant during the whole simulations, but it should be noted that in real conditions relevant variation can be detected. Also the ice thickness range that will be used for the simulations is based on the ISO guidelines, which prescribe to assume a thickness ranging from 0.1 m to 0.8 m and therefore we will use the following values: $h_i = 0.1$ m, $h_i = 0.4$ and m $h_i = 0.8$ m. ISO guidelines do not provide a range of values for the ice drifting speed. Therefore, we opted for a range of value used in similar studies [29] [37] [46]. We will presents results corresponding to the following values: $v_i = 0.1$ m/s, $v_i = 0.3$ m/s and $v_i = 0.5$ m/s.

Table 4.3: Ice characteristics

Parameter	Value	
Density	880	kg/m^3
Crushing strength	2300	kPa
Bending strength	580	kPa
Young modulus	5.4	Gpa
Poisson ratio	0.33	
Friction Coefficient	0.05	

In the DLL the ice loads are evaluated by integrating the contact forces over the structure WL. Due to the irregular geometry of the ice edge and to the platform motion, different breaking events occurs at different times and at different points along the WL. Therefore, the problem needs to be studied in time-domain.

The numerical procedure begins with the definition of the geometries of the platform WL and of the ice edge. The former is based on the platform position at the considered time step so it is constantly updated according to the information sent to the DLL from SIMA. The latter is updated only when a breaking phenomenon occurs. It should be noted that the original DLL was developed to account for all the 6 DOF of the structure, while in this case, due to the simplified nature of the problem, only motions in the horizontal plane are considered. Figure 4.4 shows a representation of the ice edge at three different time instances where can be seen how it is updated. It should be noted that Figure 4.4 refers to a fixed column case, so the WL does not changes with time and that the SIMA reference system is used.

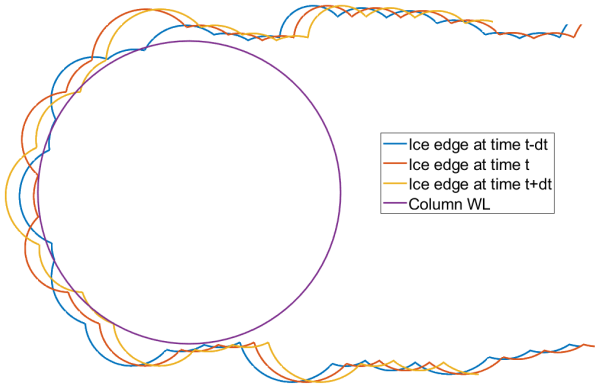

Figure 4.4: Ice edge development in time

Once the geometries have been defined, the code search for overlapping areas between them. For each contact zone, the contact length L_h and indentation length L_d are defined (see Figure 4.5(b)) and then the contact area is calculated based on these lengths, on the frame angle ϕ and on the ice thickness h_i. As shown in Figure 4.5(a), two cases exists for the contact area, which are evaluated following Eq. (4.1).

$$A_{cr} = \begin{cases} \frac{1}{2} L_h \frac{L_d}{\cos\phi} & \text{if } L_d \tan\phi \leq h_i \text{ (case 1)} \\ \frac{1}{2}\left(L_h + L_h \frac{L_d - \frac{h_i}{\tan\phi}}{L_d}\right) \frac{h_i}{\sin\phi} & \text{if } L_d \tan\phi > h_i \text{ (case 2)} \end{cases} \tag{4.1}$$

Once the magnitude of the contact area has been determined, the local crushing force F_{cr} is evaluated based on the average contact pressure method [47], described by Eq. 4.2

$$F_{cr} = p_{av} A_{cr} \tag{4.2}$$

where the average contact pressure p_{av} can be evaluated by the pressure-area curve (Eq. (4.3))

$$p_{av} = k A_{cr}^{n} \tag{4.3}$$

which is a power law based on the empirical parameters k and n.

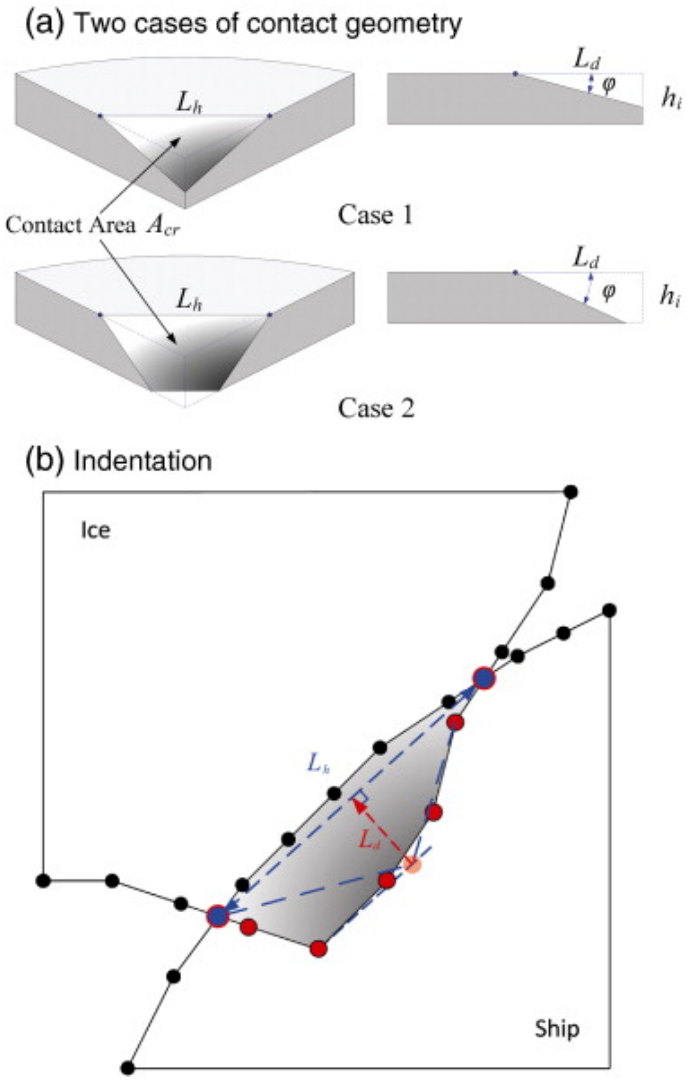

Figure 4.5: Contact geometriy cases [37]

The crushing forces are then integrated over the different contact areas to evaluate the contact loads. These forces will also have a vertical component due to the inclined side of the structure. As the overall load increases, the vertical component increases too until it exceeds the load bearing capacity of the ice sheet that will therefore fail through bending. The DLL applies the dynamic bending failure criterion which is based on finite element calculations and curve fitting. Once the ice has broken, the ice rubble is supposed to be washed away before the next contact occurs, therefore no piling-up and riding-up effect of the broken ice pieces are considered.

In order to define the updated ice edge after a breaking event, some assumptions need to be done. Generally, both circumferential and radial crack can appear. In this case, the bending cracks are supposed to be purely circular, with a breaking radius that depends on the ice thickness as generally thicker ice produces bigger ice pieces when it is broken.

4.2.2 Reference System

Since SIMA and the DLL have different reference system, some modification are needed in order to ensure a correct coupling between the two. The two reference system have opposite x and y axis, while they share they same z axis. As a result, platform position and velocity vector need to be modified according to Eq. (4.4) before they are used in the DLL.

$$\begin{cases} x_{DLL} = -x_{SIMA} \\ y_{DLL} = -y_{SIMA} \\ \dot{x}_{DLL} = -\dot{x}_{SIMA} \\ \dot{y}_{DLL} = -\dot{y}_{SIMA} \end{cases} \tag{4.4}$$

Moreover, in order for the wind and ice drifting speed to have the same direction, the ice drifting will be negative in the DLL. After the ice loads have been calculated, the same transformation done for the position and velocity needs to be applied on them. As can be seen from Eq. (4.5), also the force and moment relative to the z axis are evaluated (the sign does not change in this case) despite the motion in z direction are not considered.

$$\begin{cases} F_{x,SIMA} = -F_{x,DLL} \\ F_{y,SIMA} = -F_{y,DLL} \\ F_{z,SIMA} = F_{z,DLL} \\ M_{x,SIMA} = -M_{x,DLL} \\ M_{y,SIMA} = -M_{y,DLL} \\ M_{z,SIMA} = M_{z,DLL} \end{cases} \tag{4.5}$$

4.2.3 Ice Load DLL Analysis

At the beginning some compatibility issues were encountered, since the original DLL was meant to work with HAWC2 instead of SIMA. These issues involved the exchange of information between SIMA and the DLL. Particularly, the body position and velocity need to be sent from SIMA to the DLL, while the calculated forces are sent from the DLL to SIMA. These variables need to have specific names in the DLL for SIMA to be able to read them, as explained in the SIMO user manual appendix C [48]. Body position and velocity are stored into the variable *state* while the forces that SIMA reads need to be stored into the variable *stor*. Note that since *state* contains both translations and angular position and velocities, no other information on the body are needed to evaluate the ice loads.

Before the fully coupled simulations involving both wind and ice loads on a semi-submersible floating platform can be performed, we need to analyze how the different parameters affect the ice loads and we also need to compare this results with some other test to ensure their reliability. In order to do this, we performed some simulations on a bottom fixed column with a diameter of 8 m and a slope angle of 45°. This simulations have been carried out without any coupling, which means that the column position was kept constant and equal to (0,0), while only the ice was moving.

Since the load in the x direction (F_x) is the most relevant, we will now focus on this

component only. Figure 4.6 shows an example of the load history for a case with $h_i = 0.4$ m and $v_i = 0.3$ m/s. By zooming into the load history (Figure 4.7) we can see that single load cycles follow the behavior described in §3.4. However, since the DLL account for multiple contact zones at the same time, the load does not necessarily drops to zero after a breaking event occurs. This represents the cases for which the ice fails in one point, while the contact force is still arising in some other point of the WL.

In order to study the effect of the ice thickness h_i and velocity v_i, we selected 3 values for each of them and run 9 simulations with all the possible variable combination. Selected ice thicknesses were 0.1 m , 0.4 m and 0.8 m while selected speed were 0.1 m/s, 0.3 m/s and 0.5 m/s. Figures 4.8 and 4.9 summarize the results in terms of mean value and standard deviation. As expected, the load increases with both thickness and velocity, but we can see how the former has a stronger influence on both the mean value and the standard deviation.

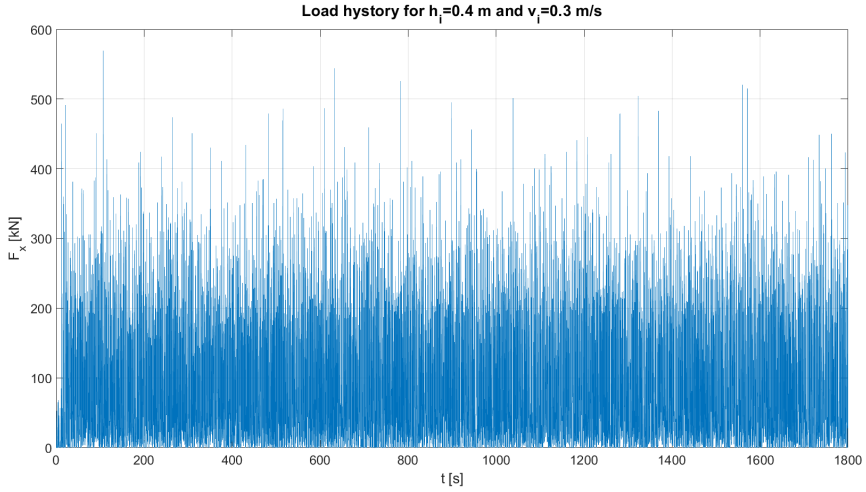

Figure 4.6: Load history for uncoupled analysis on bottom fixed column for $h_i = 0.4$ m and $v_i = 0.3$ m/s

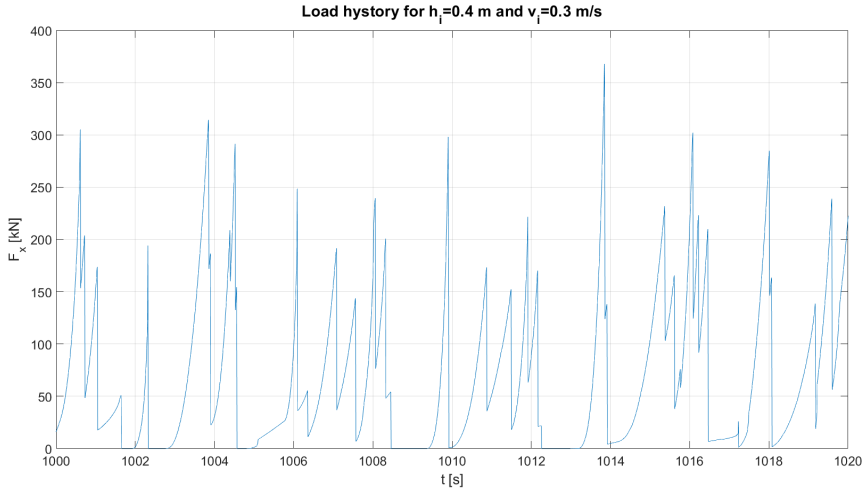

Figure 4.7: Load history for uncoupled analysis on bottom fixed column for $h_i = 0.4$ m and $v_i = 0.3$ m/s (zoom)

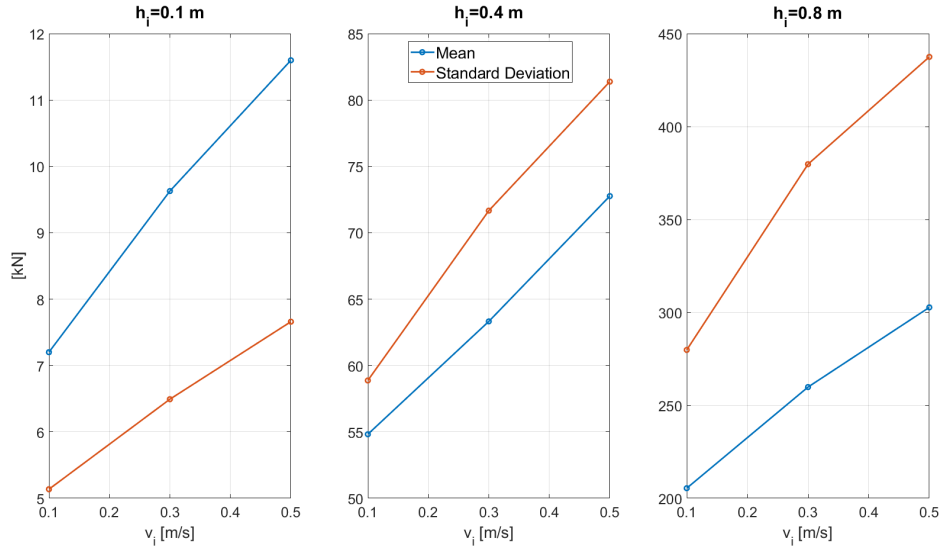

Figure 4.8: Mean value and standard deviation of F_x for uncoupled analysis on bottom fixed column without wind, as a function of ice drifting speed

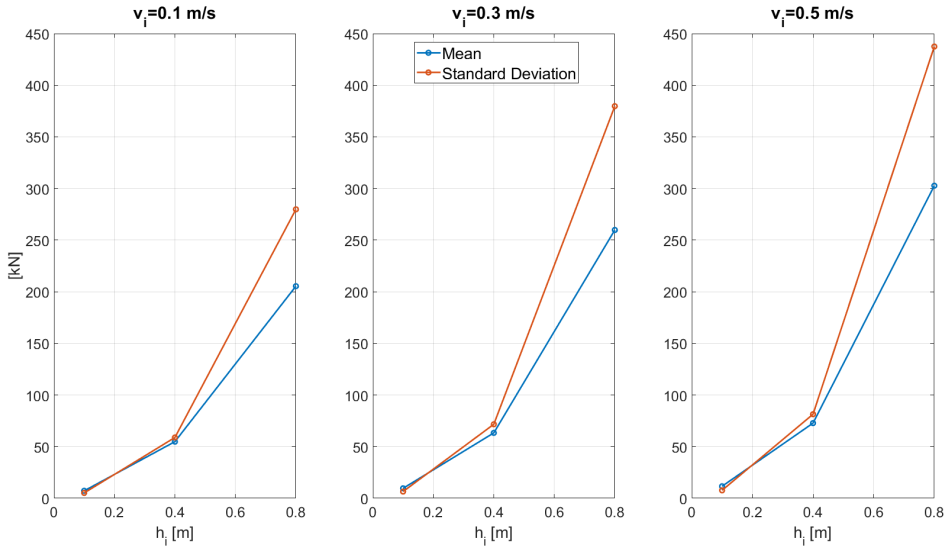

Figure 4.9: Mean value and standard deviation of F_x for uncoupled analysis on bottom fixed column without wind, as a function of ice thickness

These results follow the expectations and they also agree with those obtained by Wei Shi et al. [46], as shown in Figure 4.10. The study by Shi et al. was performed using HACWC2 and the same DLL used in this work and it refers to a rigid monopile wind turbine with the same diameter and slope angle of the bottom fixed column we are considering. Therefore the results are comparable to those obtained with our simulations.

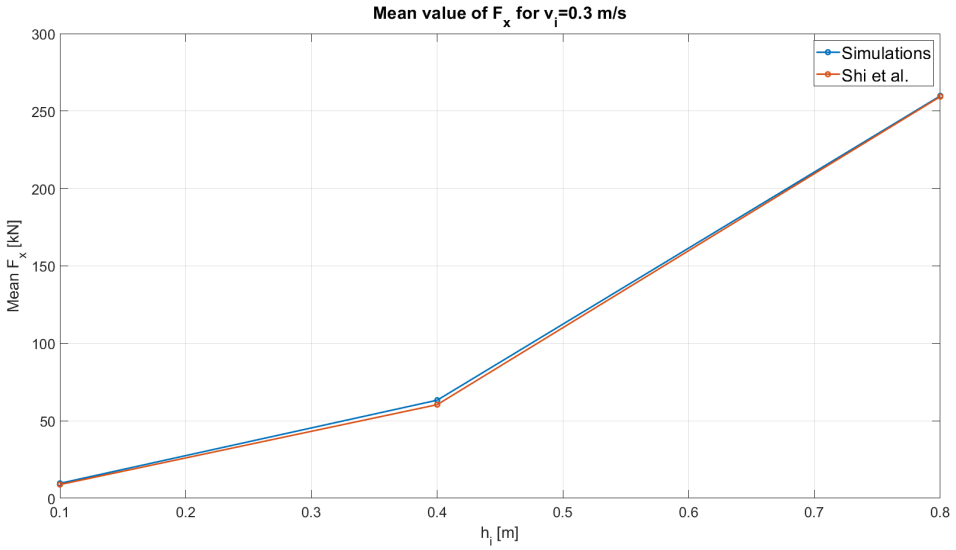

Figure 4.10: Comparison of mean value of F_x for $v_i = 0.3$ m/s between simulations and Shi et al. results [46]

Ice thickness and drifting speed do not affect only the load magnitude but also its frequency and general pattern. This phenomenon can be observed by looking at Figures 4.11 and 4.12 that represent a 100 s time series of F_x for fixed velocity and growing ice thickness and vice versa respectively.

Thin ice ($h_i = 0.1$ m) requires a little vertical component of the contact force for the bending failure to occur. As a result, the failure process is a continuous process where multiple contact points exist at the same time, also causing the load to rarely drops to zero. As the ice get thicker ($h_i = 0.4$ m) the failure process is less continuous. We can observe that in this case the load drops to zero more frequently. However, multiple peaks can still be found between two zero loads. For thick ice ($h_i = 0.8$ m) the load history assumes a periodic saw-tooth-like pattern, which is described also by Shi et al. [46]. We can also see that the load drops to zero between peaks and that it remains at zero for longer time if compared to thinner ice.

On the other hand, increasing the ice speed leads to an higher load frequency. This is easily explained by the fact that as the ice goes faster, the vertical component of the contact load grows faster too, thus triggering the bending failure of ice at higher pace. Therefore, slow ice ($v_i = 0.1$ m/s) result in a periodic and saw-tooth-like pattern, while fast ice ($v_i = 0.3$ m/s and $v_i = 0.5$ m/s) generates a more continuous breaking process.

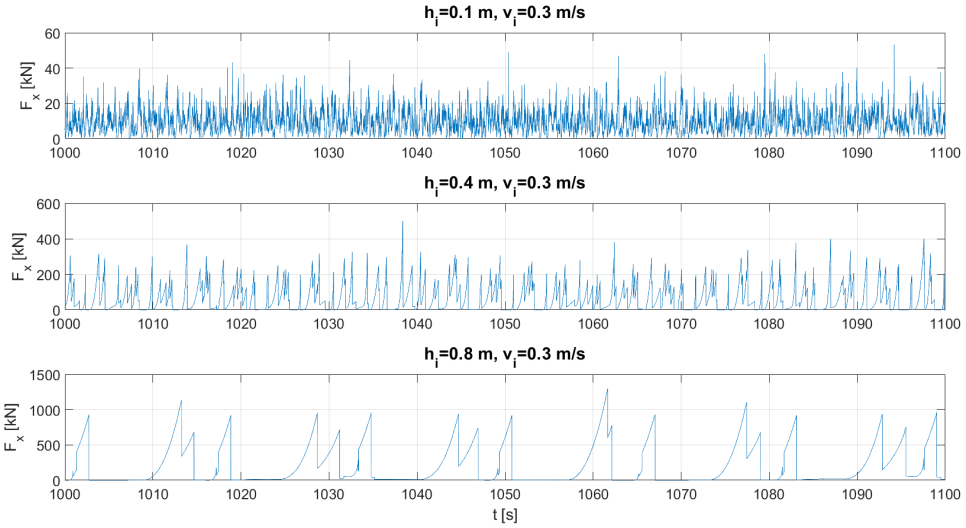

Figure 4.11: Load history for uncoupled analysis on bottom fixed column for $v_i = 0.3$ m/s and varying thickness

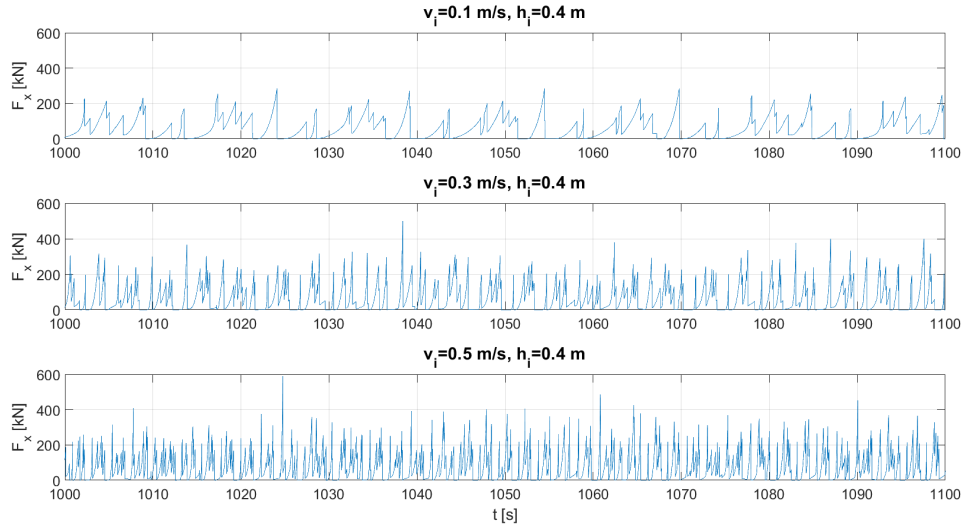

Figure 4.12: Load history for uncoupled analysis on bottom fixed column for $h_i = 0.4$ m and varying speed

In addition to the ice thickness and drifting speed, also the influence of the time step Δt used in the simulations was investigated. In order to do that, we run 6 simulations with different time step, using $v_i = 0.5$ m/s and $h_i = 0.4$ m. As can be seen from the results presented in Figure 4.13, both the mean value and the standard deviation become stable for $\Delta t \leq 0.005$. Therefore we decided to use this value for all the simulations, since smaller values would results in an increased computational time, without any significant improvement of the accuracy.

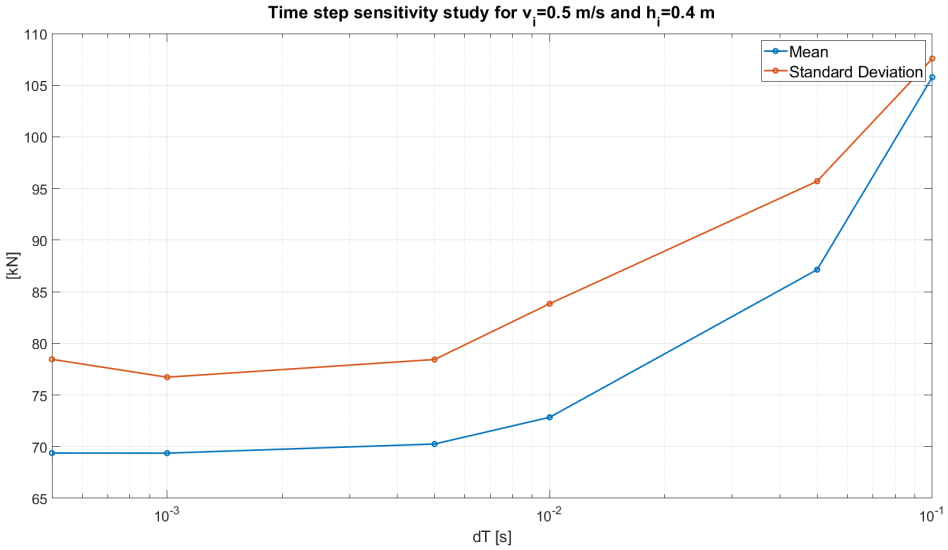

Figure 4.13: Time step sensitivity study for uncoupled analysis for $v_i = 0.5$ m/s and $h_i = 0.4$ m

4.3 Coupled Dynamic Analysis Implementation

4.3.1 Single Column

Once the ice load DLL has been modified to make it compatible with SIMA and it has been analyzed through the uncoupled analysis on a bottom fixed column, we can finally focus on the coupled dynamic analysis implementation for the semi-submersible floating wind turbine. We will first describe the modifications needed to correctly perform the coupled dynamic analysis applying the load on the central column of the platform only. After that, we will present the additional modifications which are needed to account for the ice load on all the 4 columns.

As already mentioned, the coupling between the DLL and SIMA is obtained by updating the platform position and velocity into the DLL using the value from SIMA at the beginning of every time step. Using these inputs, the DLL evaluates the corresponding ice load which is sent to SIMA. SIMA then solves the dynamic equilibrium equations considering all the loads (including the ice load) and evaluate the position of the platform which is the input for the new time step.

In the load history presented in the previous section, the ice load could be started at the beginning of the simulations without this causing any issues. However, this can not be done when the coupling and the floating platform are considered. In fact, the platform is free to move in x direction before reaching an equilibrium point that depends on the magnitude of the load. So if the ice load starts at the beginning of the simulations (i.e. when the platform center has coordinate (0,0)) it will be pushed away by the combined action of wind and ice thus resulting in too high motions that could lead to a too long transient or, in worst cases, too a lack of convergence.

In order to solve this problem, we decided to follow the same procedure presented by Saccoman [29], which is to initialize the load that SIMA receives from the DLL with a 1000 s long linear ramp load that does not depends on the platform position. By doing

this, the platform is pushed as close as possible to the equilibrium position during the first 1000 s. After this period, the ice load can be evaluated without problem since the platform will not be subjected to excessive motions. The load ramp is applied only on F_x and M_y since the other forces and moments a much less relevant impact on the platform position. The ramp is tuned so that the load after 1000 s is equal to the mean load of the uncoupled analysis.

However, applying the ice loads after the platform has been moved to the equilibrium position, means that there is a distance between the initial ice edge and the platform, since the initial ice edge is meant for a column having its center located at (0,0). This causes the time between the end of the ramp and beginning of the actual ice load to be high, since the ice edge must cover all the distance between its initial position and the platform equilibrium position before the contact start. During this time, the platform is not subjected to any load from the DLL and therefore the mooring line tension would tend to bring it back to the initial position, thus resulting again in excessive motion that could arise before the ice load start, leading the the fore-mentioned issues. This problem was solved again using the procedure described by Saccoman [29] which consists in updating the ice edge position before the the ice load calculation begins. After the initial ramp (i.e. for $t = 1000$ s), each of the points constituting the ice edge is moved by a distance equal to the platform position at $t = 1000$ s. It should be noted that this correction is applied for $t = 1000$ s, after this, the ice edge is simply moved by a quantity equal to the velocity times the time step. An example of the initial position correction is shown in Figure 4.14.

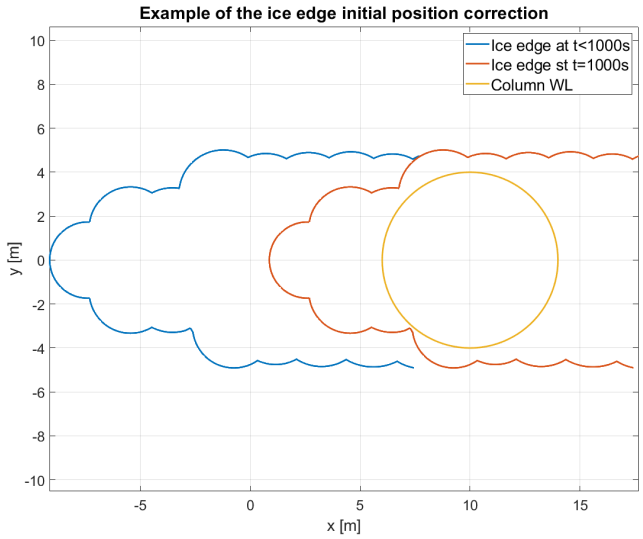

Figure 4.14: Example of the ice edge initial position correction

With these modifications, the code can now be applied to the floating platform to perform coupled analysis including both wind and ice loads. An example of the resulting time series of the ice load acting on the central column only for a case with $v_i = 0.5$ m/s, $h_i = 0.4$ m and $v_w = 12$ m/s can be seen in Figure 4.15.

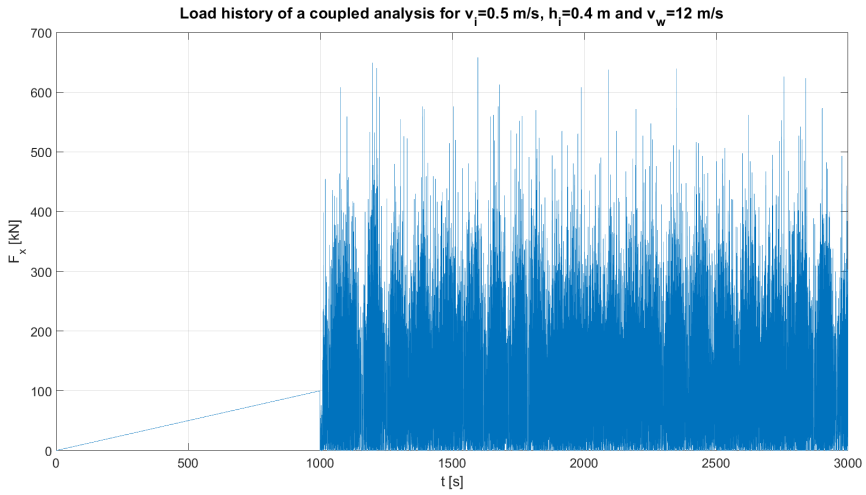

Figure 4.15: Load history for coupled analysis on the central column of the floating platform

4.3.2 Multiple Columns

The ice load DLL is capable to model loads acting on one column only. However, in real conditions, all the four columns will be subjected to different loads at the same time. In order to model this phenomenon, we used 4 different DLL each acting on one column of the platform. As it is shown in Figure 4.16, which represent the 4 columns WL and the correspondent ice edges, no wake interaction is considered. This means that the ice edge around each of the column is completely independent from the others. However, in real life condition, this effect would be present and it would result in a reduced load intensity since some of the column would be subjected to ice loads due to ice rubble instead of level ice. E.g for the ice drifting direction considered in this analysis (i.e. along the x axis), column 3 will be partially in the wake of the central column, thus resulting in a reduced ice load.

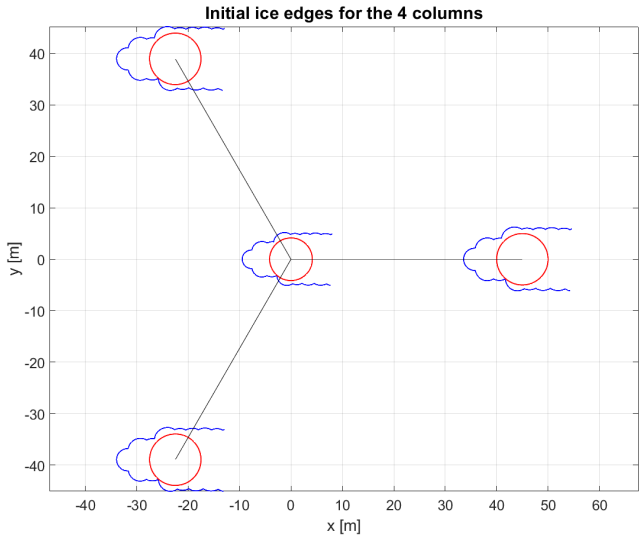

Figure 4.16: Initial ice edge for the 4 column

The 4 DLL are independent from each other, since they use different ice edges and since they evaluate the ice loads based on the position and velocity of the corresponding column. However, SIMA provides positions and velocities only for one point (located at the origin of the reference system) of the SIMO body representing the platform. It was therefore necessary to modify the code in order to evaluate the position and the velocity of each column based on the rigid body motions of the platform. In order to do that, we applied the linear approximations of the equations of motions [30].

If we denote with $\mathbf{r}_0 = x\mathbf{i} + y\mathbf{j} + z\mathbf{k}$ the initial position of a column, the motion of the column is described by:

$$\mathbf{r} = \eta_1\mathbf{i} + \eta_2\mathbf{j} + \eta_3\mathbf{k} + \boldsymbol{\omega} \times \mathbf{r}_0 \tag{4.6}$$

where η_1, η_2, η_3 are the platform displacements, $\mathbf{i}$, $\mathbf{j}$, $\mathbf{k}$ are the unit vectors and

$$\boldsymbol{\omega} = \eta_4\mathbf{i} + \eta_5\mathbf{j} + \eta_6\mathbf{k} \tag{4.7}$$

is the angular position of the platform. Which means that the column position is given by:

$$\mathbf{r} = (\eta_1 + z\eta_5 - y\eta_6)\mathbf{i} + (\eta_2 - z\eta_4 + x\eta_6)\mathbf{j} + (\eta_3 + y\eta_4 - x\eta_5)\mathbf{k} \tag{4.8}$$

The column position is then used to evaluate the column velocity $\dot{\mathbf{r}}$

$$\dot{\mathbf{r}} = \dot{\eta_1}\mathbf{i} + \dot{\eta_2}\mathbf{j} + \dot{\eta_3}\mathbf{k} + \dot{\boldsymbol{\omega}} \times \mathbf{r} \tag{4.9}$$

where $\dot{\eta_1}$, $\dot{\eta_2}$, $\dot{\eta_3}$ are the platform speed in the 3 directions and

$$\dot{\boldsymbol{\omega}} = \dot{\eta_4}\mathbf{i} + \dot{\eta_5}\mathbf{j} + \dot{\eta_6}\mathbf{k} \tag{4.10}$$

is the platform angular velocity.

Table 4.4 lists the initial position of the 3 external columns. This procedure is not needed for the central one, since its position and velocity are the same of the origin of the reference system which are directly given by SIMA.

Table 4.4: Columns initial position

Column	x [m]	y [m]	z [m]
Column 1	-22.50	38.97	0.00
Column 2	-22.50	-38.97	0.00
Column 3	45.00	0.00	0.00

5 Results

Once all the correction and modification have been applied to the code, we are able to perform simulations with all the conditions. First, we will present the total ice load acting on the platform, i.e. the sum of the different loads acting on each of the column.

Then, we will present the ice edge development for the different columns for different conditions, in order to show how the platform dynamic and the ice parameters affect the ice-breaking process.

Finally, in order to understand how the different parameters (ice thickness and ice drifting speed) affect the platform motion, we will present the platform velocity and the platform motions in terms time series and statistical properties. The results are presented by keeping one parameters constant and varying the other. All the presented results corresponds to 3000 s long simulations with a time step $\Delta t = 0.005$ s. The first 1500 s of the simulations are disregarded because we are only interested in the steady state response and not in the transient response. For all the cases, we performed coupled analysis considering the four columns and all the corrections presented in the previous section. Also, wind loads are always considered and the wind turbine is in operating conditions.

5.1 Ice Loads

Forces in x and y direction and moment around the 3 axis are presented. The force in the z direction is not presented since this is of minor relevance with respect to the platform dynamic. Only one case, corresponding to $v_i = 0.5$ m/s, $h_i = 0.4$ m and $v_w = 12$ m/s, is shown here and the first 1000 s of the time series are disregarded since only the initial load ramp is acting during that time.

Force in the x direction F_x (Figure 5.1) and moment around the y axis M_y (Figure 5.4) are the only component having a non-zero mean value, while the other 3 components (Figures 5.2, 5.3 and 5.5) oscillates around zero due to the symmetry of the problem. Another interesting aspect is that the minimum values of F_x and M_y are higher then 0, while the load was almost dropping to 0 for the load on a single column. This is due to the loads on the 4 columns being out of phase, which makes extremely rare for the 4 loads to be equal to 0 at the same time. This effect becomes more relevant as the load frequency increases, i.e. when the ice is thinner and/or faster.

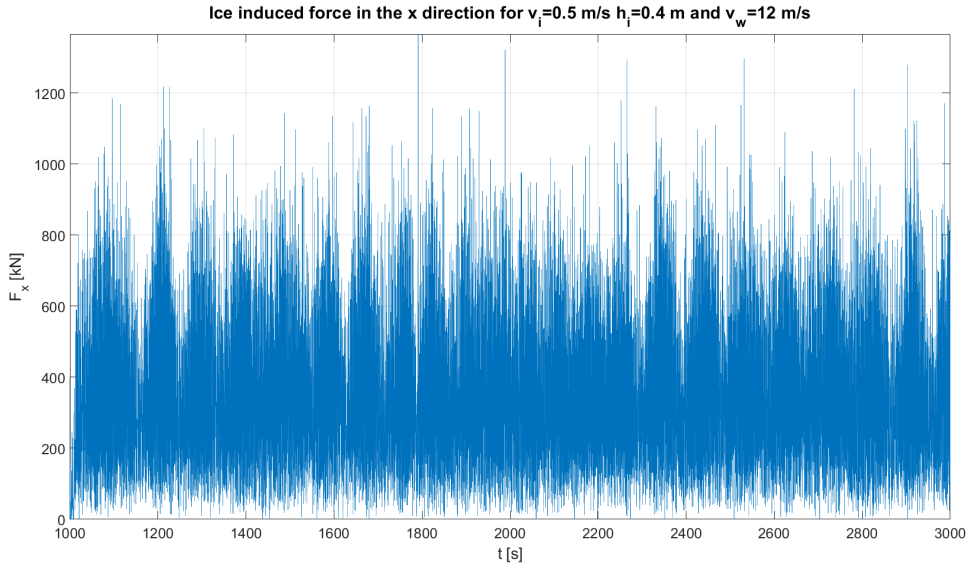

Figure 5.1: Time series of the ice induced force in the x direction for $v_i = 0.5$ m/s, $h_i = 0.4$ m and $v_w = 12$ m/s

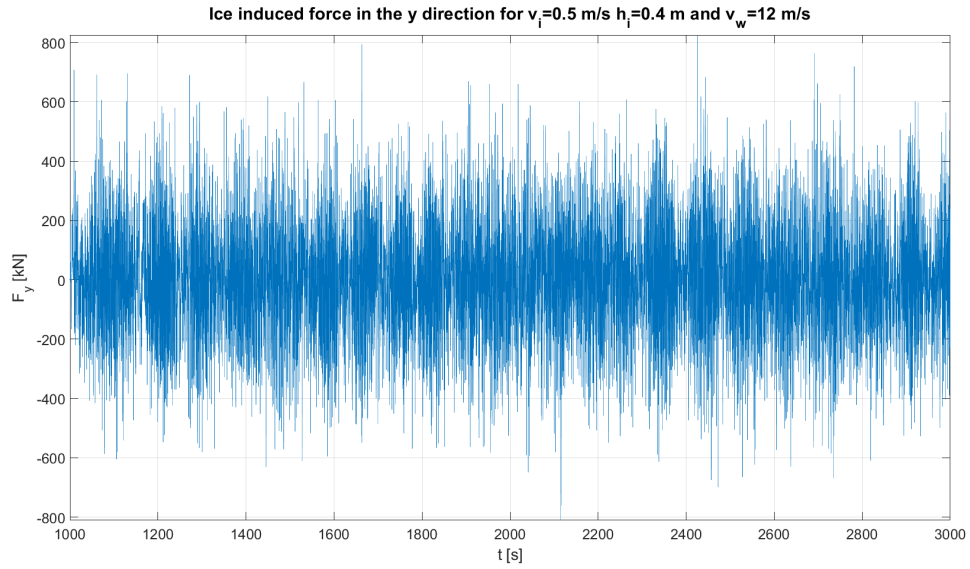

Figure 5.2: Time series of the ice induced force in the y direction for $v_i = 0.5$ m/s, $h_i = 0.4$ m and $v_w = 12$ m/s

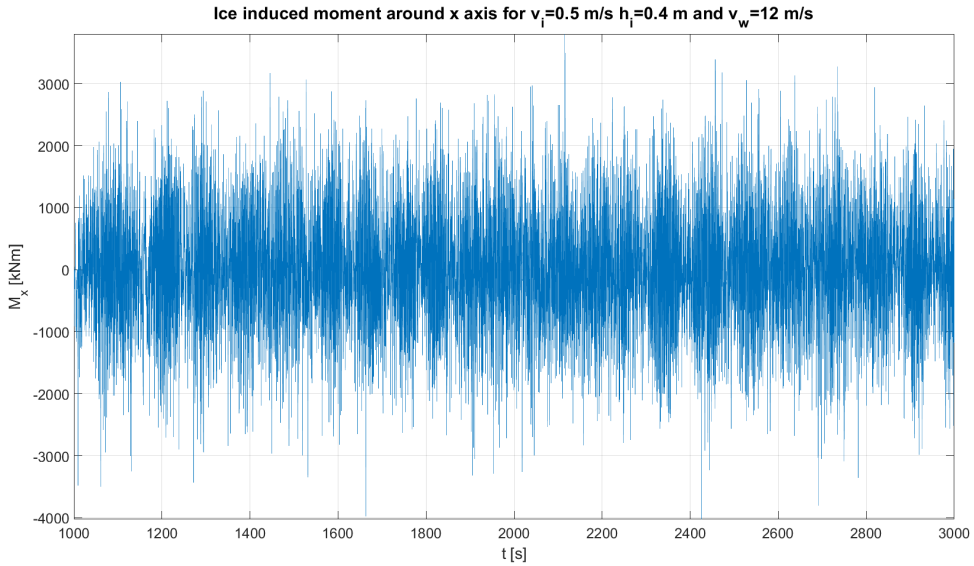

Figure 5.3: Time series of the ice induced moment around the x axis for $v_i = 0.5$ m/s, $h_i = 0.4$ m and $v_w = 12$ m/s

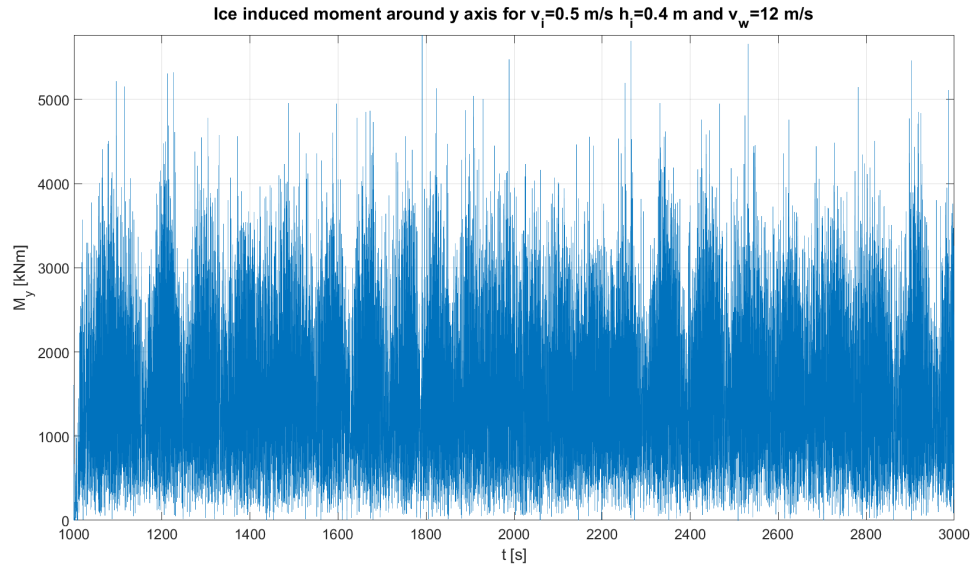

Figure 5.4: Time series of the ice induced moment around the y axis for $v_i = 0.5$ m/s, $h_i = 0.4$ m and $v_w = 12$ m/s

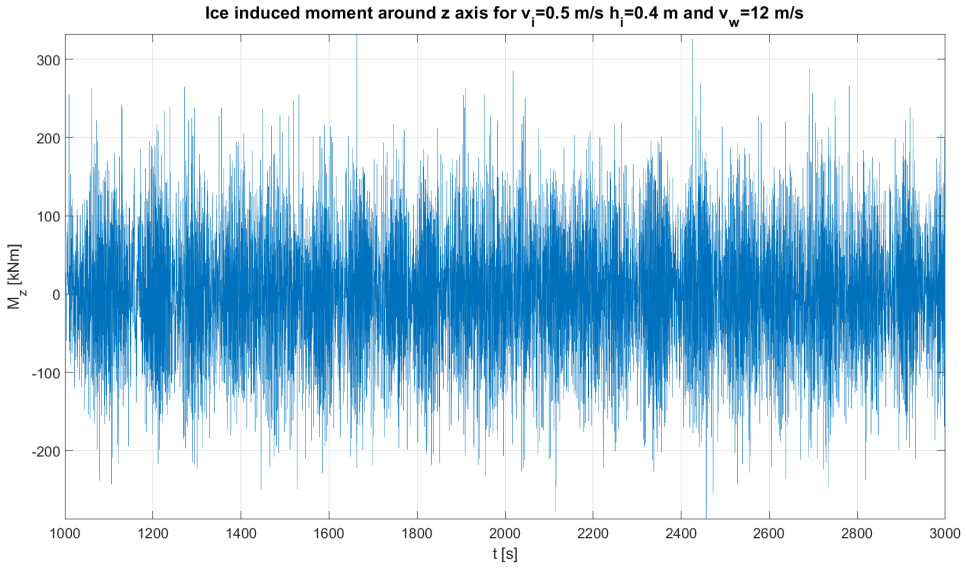

Figure 5.5: Time series of the ice induced moment around the z axis for $v_i = 0.5$ m/s, $h_i = 0.4$ m and $v_w = 12$ m/s

5.2 Ice Edge Analysis

The ice edge development around each of the column is important to understand how the ice loads evolve in time and how the ice parameters affect the ice breaking process. Figures 5.6 and 5.7 shows the central column WL and the corresponding ice edge at different time instances for $v_i = 0.5$ m/s, $h_i = 0.4$ m and $v_w = 12$ m/s.

The side movement of the platform result in the ice crushing on the side of the column in addition to the front. This results in an ice channel that is wider then the actual column diameter. It follows that when a floating structure is considered, the wake will be wider then the one we would get for a bottom fixed structure with the same diameter, as a result of the lateral motion which are not present in bottom fixed structures.

Because of the widening of the wake, it can occur that the column is contact with the ice on one side only (t=2125 s) and as a result the load in the y direction can be unbalanced during these time periods. However, this force in the y direction tends to push the column towards the middle of the ice channel, thus balancing this effect and restoring the usual relative position.

Another interesting aspect is related to the relative velocity between the ice and the platform. At the beginning of the shown time span, the column is moving with negative speed in the x direction (see Figure 5.8), i.e. opposite to the ice drifting speed. As a result, the ice edge tends to expand in the negative x direction despite it is drifting in the positive direction. When this occurs, the ice load is locally higher because the relative speed is higher then the actual ice drifting speed. On the other hand, when the platform is moving in the same direction of the ice edge, the relative speed is lower then the ice drifting speed and therefore the load tends to be lower too. Moreover, the relative velocity has an influence on the load frequency too, which is higher when the relative speed increases, meaning that the load frequency slightly changes as the ice/structure interaction develops. All these effects clearly become more important for slower ice, because the platform velocity is more relevant compared to the ice velocity and therefore it has a

stronger influence on the relative velocity.

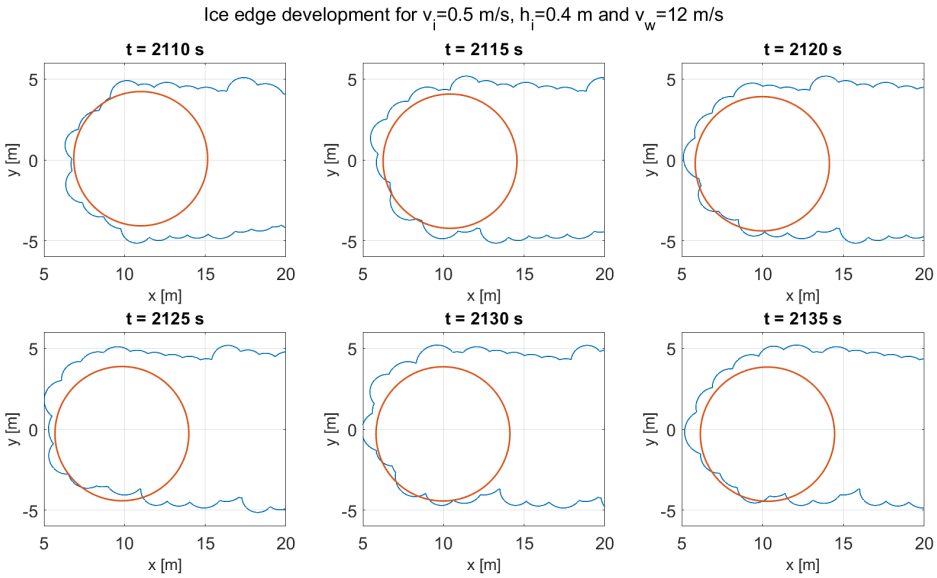

Figure 5.6: Ice edge development around the central column for $v_i = 0.5$ m/s, $h_i = 0.4$ m and $v_w = 12$ m/s (a)

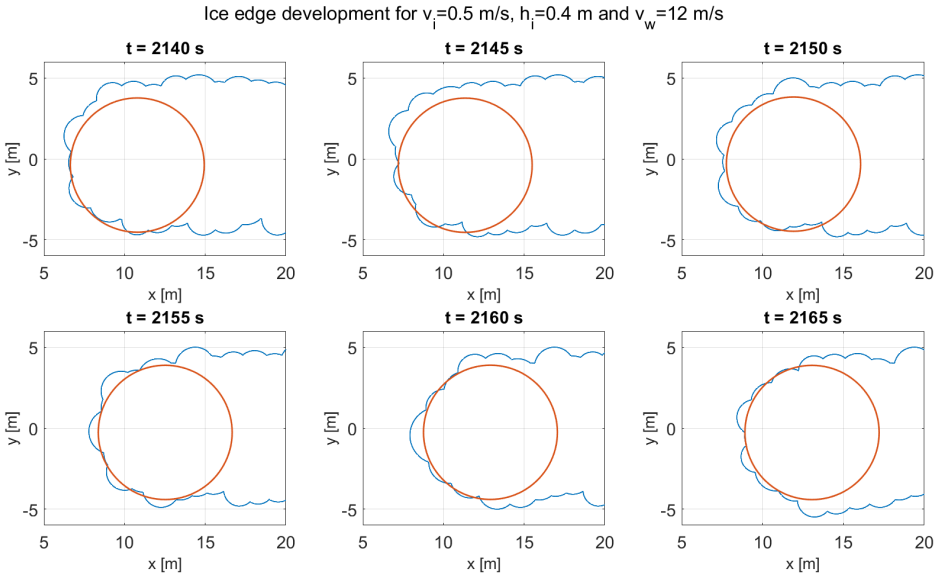

Figure 5.7: Ice edge development around the central column for $v_i = 0.5$ m/s, $h_i = 0.4$ m and $v_w = 12$ m/s (b)

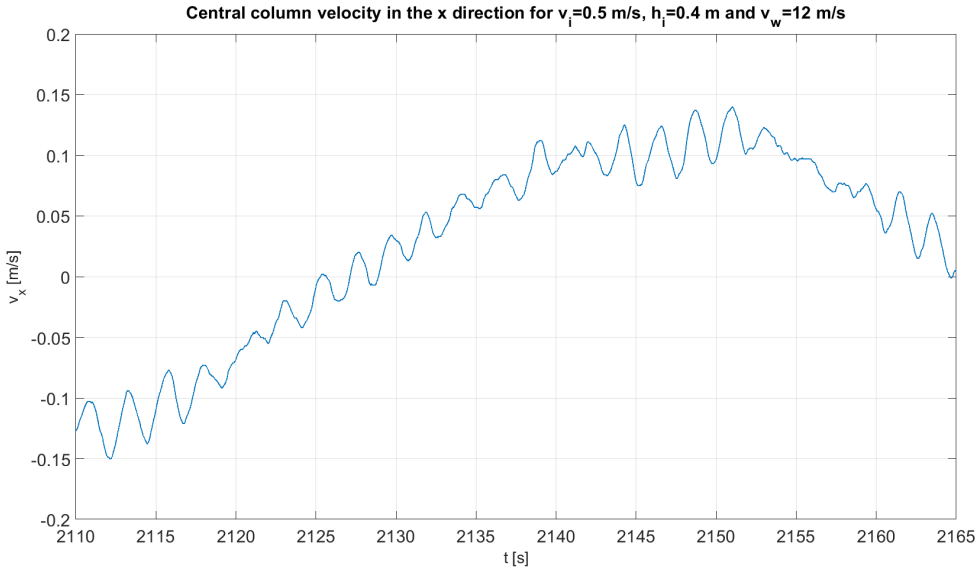

Figure 5.8: Central column velocity in the x direction for $v_i = 0.5$ m/s, $h_i = 0.4$ m and $v_w = 12$ m/s

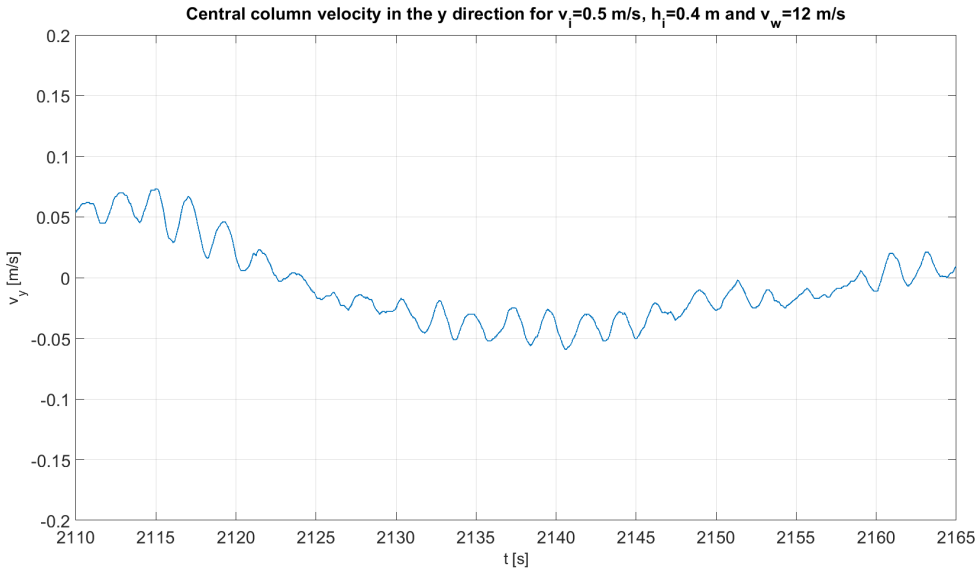

Figure 5.9: Central column velocity in the y direction for $v_i = 0.5$ m/s, $h_i = 0.4$ m and $v_w = 12$ m/s

5.2.1 Particular Case: High Thickness and Low Drifting Speed

The ice breaking process described in the previous section is a continuous process, where the load remains equal to 0 only for a few seconds before it starts to grow again. However, for some particular cases this does not happen. When the considered wind speed is close to the rated wind speed for the wind turbine, the induced platform motion can be high and consequently the platform speed can be higher then the ice drifting speed. When this happens, the relative velocity between the ice and the floater is in the opposite direction of the ice drifting direction, meaning that the structure gets further from the ice. In such

cases, the load can remain equal to 0 for longer time interval, but the platform motion will eventually change direction again and the breaking process will restart normally.

Another case that can cause some issues regarding the ice breaking process is when the ice is slow and thick. In such cases, the contact force may not be enough to trigger the breaking process. When this happens, the platform is simply pushed away by the ice without any change in the ice edge. An example of how the ice edge evolves in such cases is shown in Figures 5.10 and 5.11, where a case with $v_i = 0.1$ m/s, $h_i = 0.8$ m and $v_w = 12$ m/s is considered.

It is clearly shown that from $t = 1145$ s to $t = 1180$ s, the ice edge and the column are moving together without any breaking phenomenon occurring. In fact, the ice edge does not change during this time span, the platform speed in the x direction (Figure 5.12) oscillates very closely around the ice drifting speed and the platform speed in the y direction (Figure 5.13) oscillates around 0. During this time span, the calculated ice load is either equal to 0 or negative, as shown in Figure 5.14. However, this should not happened since the contact areas are located on the left half of the column WL only and therefore the load should be positive, if not 0. This may be due to some inaccuracies in the code which is not able evaluate loads in cases where no breaking process occurs.

After $t = 1170$ s, the platform velocity decreases slightly again so the column is pushed against the ice and the breaking process starts again. In fact, after $t = 1170$ s we can see that the column and the ice edge come closer together, but this is still not enough to generate a contact load. Eventually, after $t = 1190$ s, the column is pushed through the ice and the load start to increase again, up to the point when a breaking phenomenon occurs and the ice edge is updated ($t = 1195$ s).

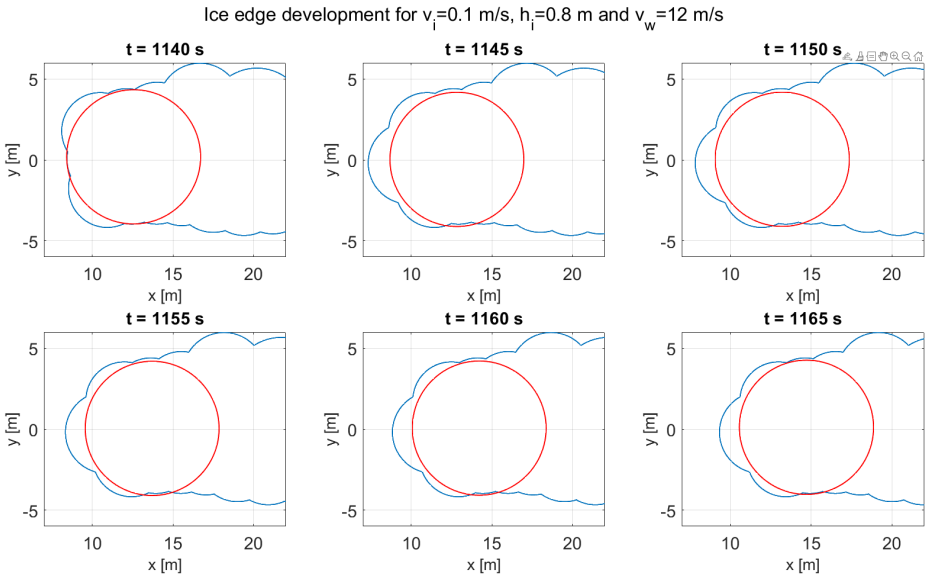

Figure 5.10: Ice edge development around the central column for $v_i = 0.1$ m/s, $h_i = 0.8$ m and $v_w = 12$ m/s (a)

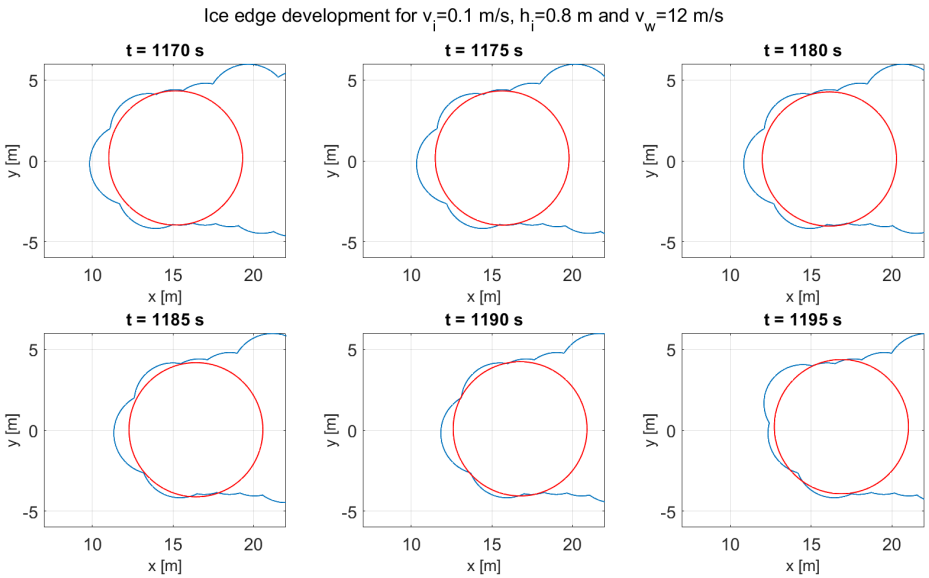

Figure 5.11: Ice edge development around the central column for $v_i = 0.1$ m/s, $h_i = 0.8$ m and $v_w = 12$ m/s (b)

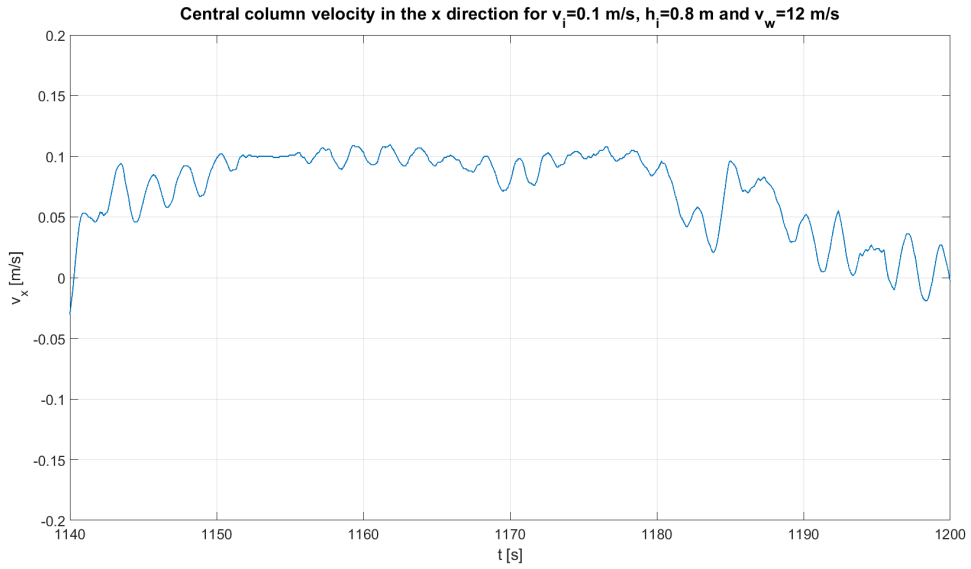

Figure 5.12: Central column velocity in the x direction for $v_i = 0.1$ m/s, $h_i = 0.8$ m and $v_w = 12$ m/s

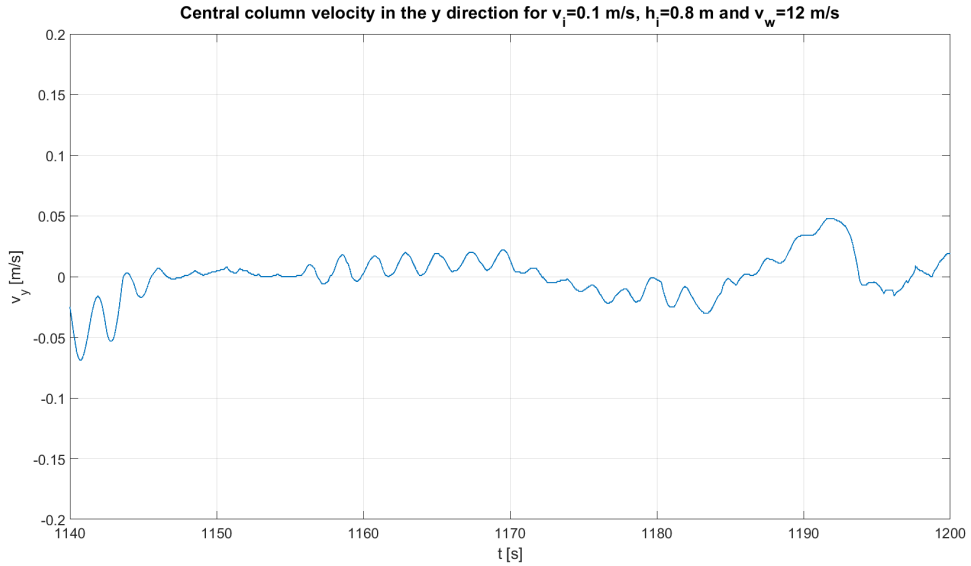

Figure 5.13: Central column velocity in the y direction for $v_i = 0.1$ m/s, $h_i = 0.8$ m and $v_w = 12$ m/s

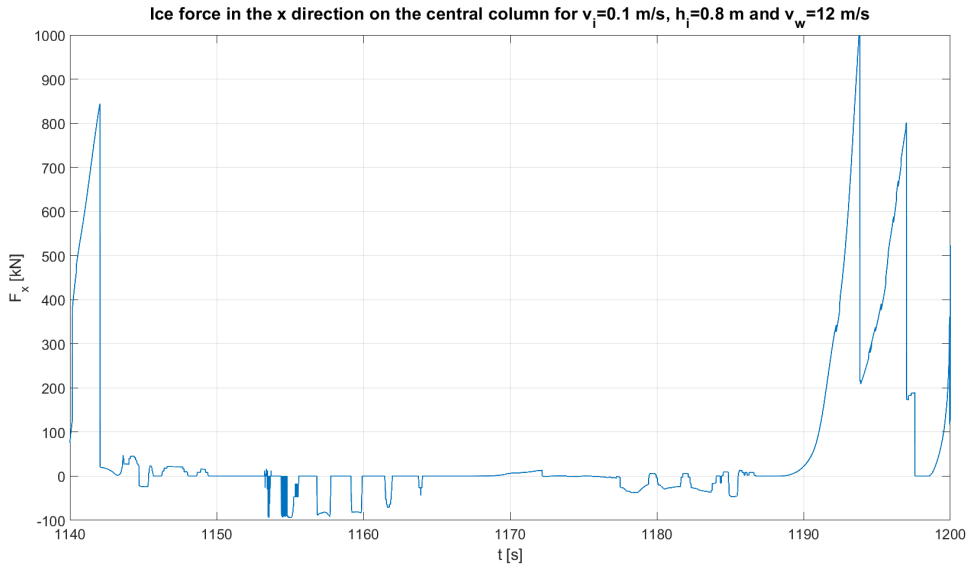

Figure 5.14: Ice force in the x direction on the central column for $v_i = 0.1$ m/s, $h_i = 0.8$ m and $v_w = 12$ m/s

5.3 Ice Thickness Influence

In order to describe the influence of the ice thickness, we present two sets of conditions with ice thicknesses equal to $h_i = 0.1$ m, $h_i = 0.4$ m and $h_i = 0.8$ m. A case with no ice is evaluated too. The sets differ in the ice speed, which is taken as $v_i = 0.5$ m/s and $v_i = 0.3$ m/s, while the wind speed is $v_w = 12$ m/s for all cases.

5.3.1 Ice and Wind Loads Comparison

Figure 5.15 shows a comparison between the aerodynamic thrust on the wind turbine rotor and the ice force in the x direction for different ice thickness. It should be noted that only the one time series of the aerodynamic thrust is provided, since it result almost unaffected by the ice loads. The mean wind thrust is approximately $T = 1200$ kN which is clearly the dominant load for the cases with $h_i = 0.1$ m to which correspond a mean ice force $F_{x,mean} = 50$ kN and $h_i = 0.4$ m when the mean ice load is $F_{x,mean} = 320$ kN. On the other hand, wind and ice loads are comparable when the thickness $h_i = 0.8$ m is considered, since the mean ice load in that case is $F_{x,mean} = 1140$ kN. We should also consider that the application point of the two loads is different: ice loads act at the MSL while wind thrust is applied on the hub. Therefore, while the loads are combined in terms of forces, they are opposite to each other in terms of overturning moment.

It is also interesting to compare the wind and and ice load spectrum, shown in Figure 5.16, where only the spectrum of for $h_i = 0.8$ m is shown. We can see that wind load spectrum is more dense at low frequency, while the ice load is more spread. This means that wind load are dominant for low frequency motions while ice load have a stronger impact for higher frequency motion.

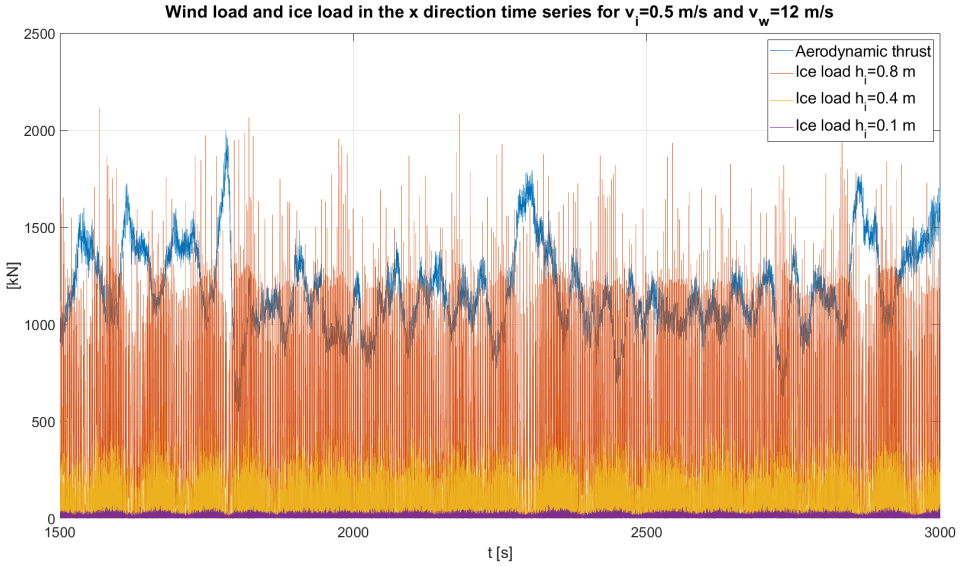

Figure 5.15: Ice and wind loads in the x direction time series comparison for $v_i = 0.5$ m/s, $v_w = 12$ m/s and different ice thickness

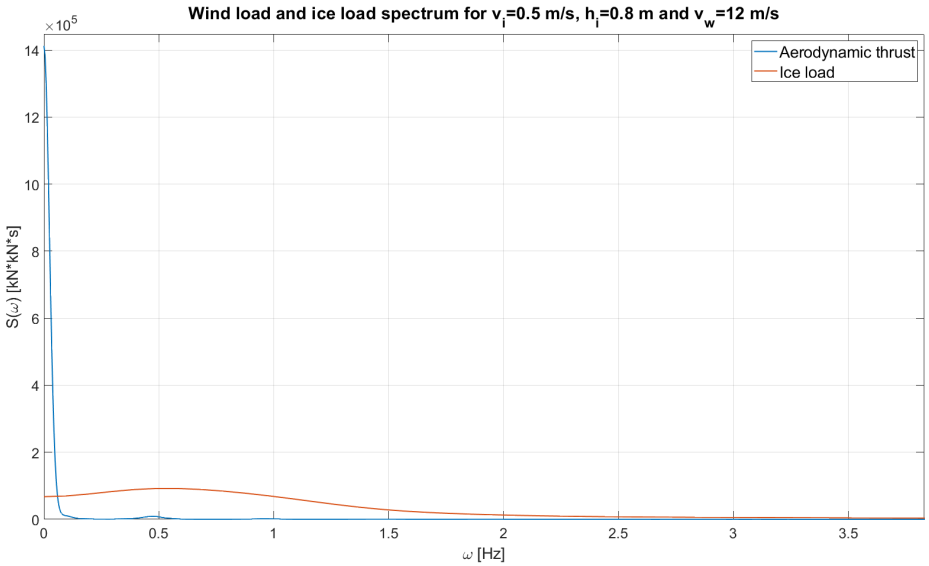

Figure 5.16: Ice and wind loads in the x direction spectrum comparison for $v_i = 0.5$ m/s, $h_i = 0.8$ m and $v_w = 12$ m/s

While in the x direction the wind load are dominant compared to the ice loads, the ice loads are much more relevant then the wind loads in the y direction, as shown in Figure 5.17. Both ice and wind loads in the y direction have almost 0 mean value. However, for thick ice, the oscillation amplitude is much higher then the one for wind loads. Only in the case of thin ice, the oscillation amplitude are comparable.

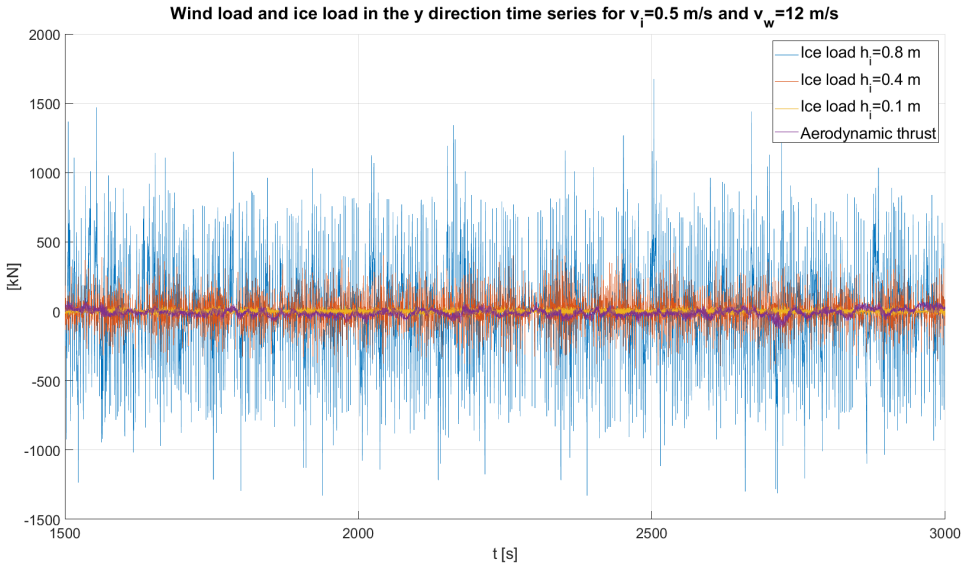

Figure 5.17: Ice and wind loads in the y direction time series comparison for $v_i = 0.5$ m/s, $v_w = 12$ m/s and different ice thickness

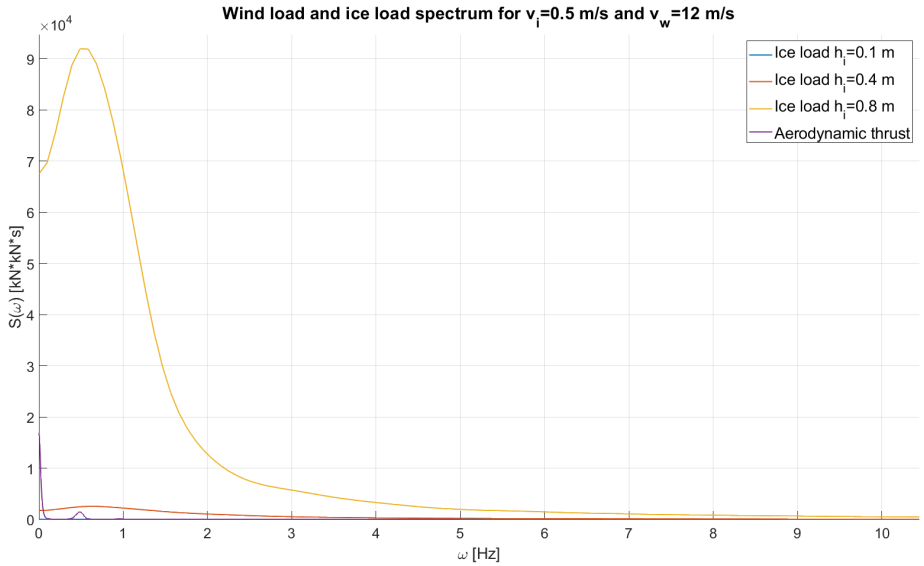

Figure 5.18: Ice and wind loads in the y direction spectrum comparison for $v_i = 0.5$ m/s, $v_w = 12$ m/s and different ice thickness

5.3.2 Surge Motion

Figures 5.19 and 5.20 present the surge motion time series, while Figures 5.21 and 5.22 present the statistical properties. The main effect of the increased ice thickness with respect to the translation along the x axis is the increased offset of the platform. This effect is due to the higher mean value of the ice load in the x direction and we can see how it is much higher for very thick ice, thus following the quadratic relationship between ice load in the drifting speed direction and ice thickness. Another effect of the increased ice thickness is a reduction of the oscillation amplitude, which is reflected by the decreasing standard deviation and can be observed in the spectrum too, Figures 5.23 and 5.24 . Thicker ice requires a stronger force to fail and therefore it acts like a damper with respect to the platform oscillation in the x direction.

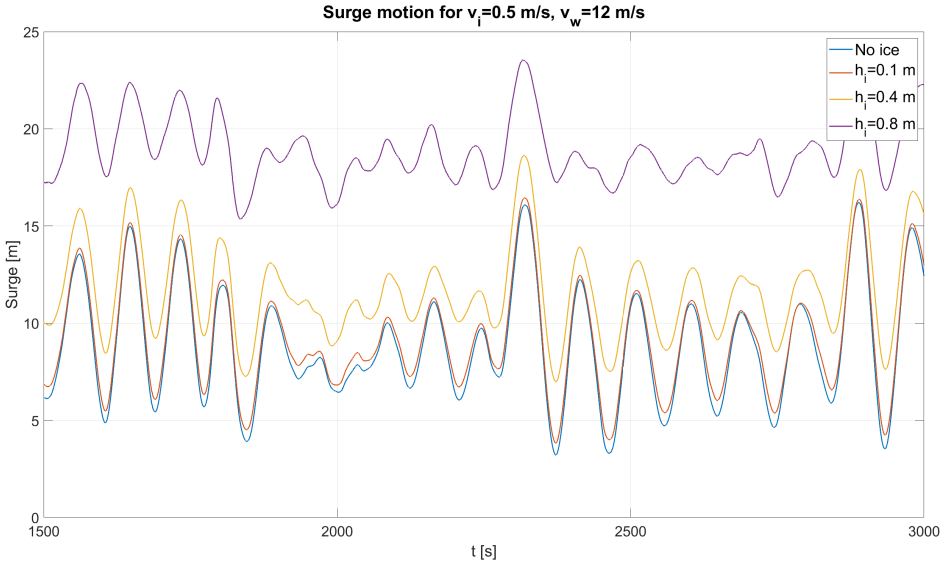

Figure 5.19: Surge motion time series for $v_i = 0.5$ m/s, $v_w = 12$ m/s and different ice thickness

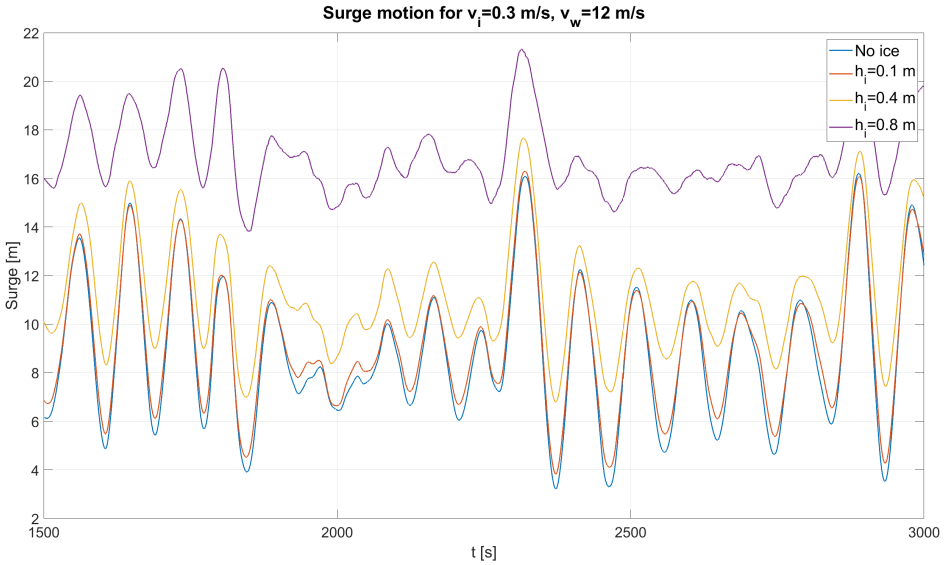

Figure 5.20: Surge motion time series for $v_i = 0.3$ m/s, $v_w = 12$ m/s and different ice thickness

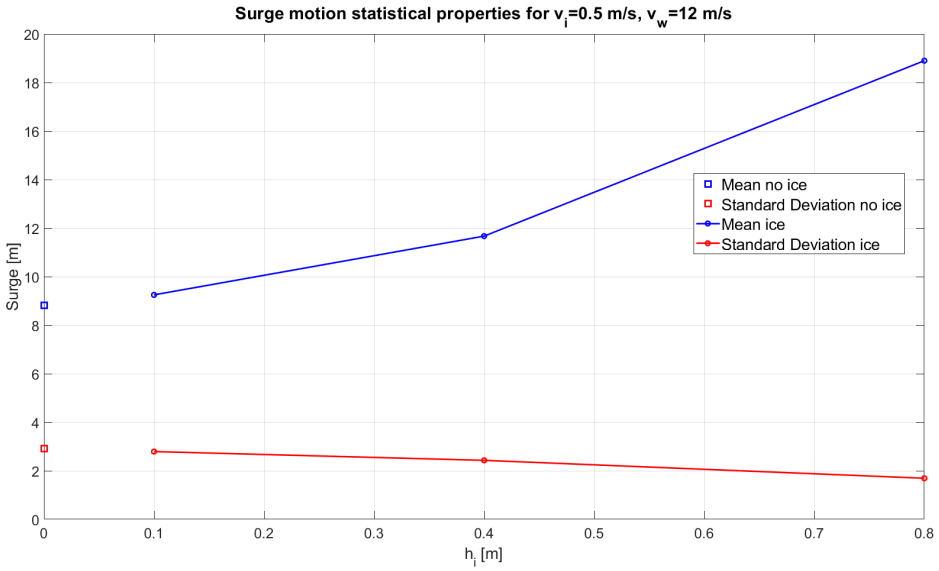

Figure 5.21: Surge motion statistical properties for $v_i = 0.5$ m/s, $v_w = 12$ m/s and different ice thickness

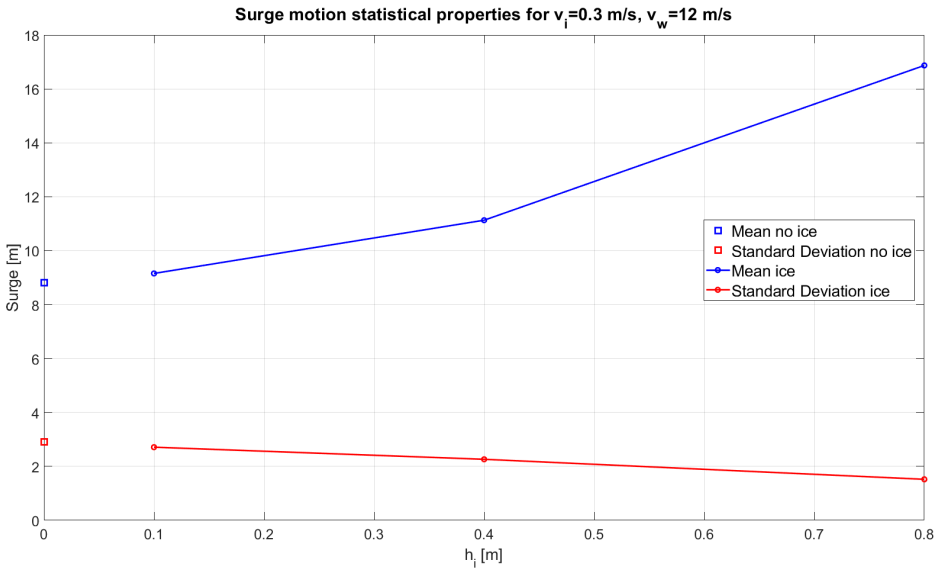

Figure 5.22: Surge motion statistical properties for $v_i = 0.3$ m/s, $v_w = 12$ m/s and different ice thickness

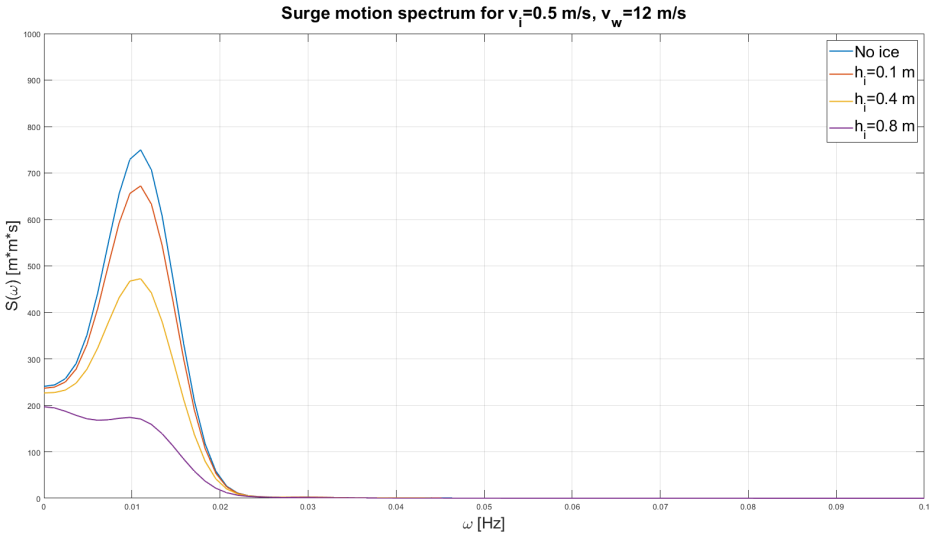

Figure 5.23: Surge motion spectrum for $v_i = 0.5$ m/s, $v_w = 12$ m/s and different ice thickness

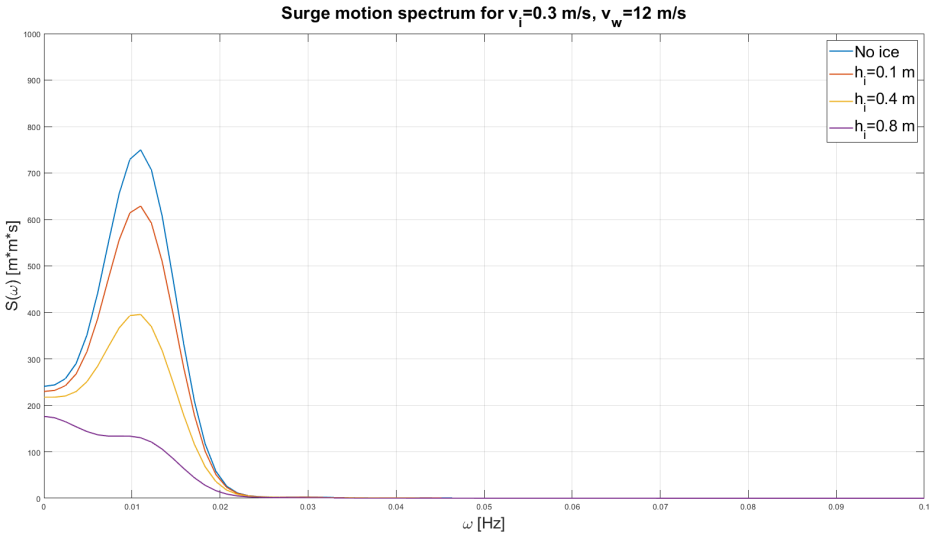

Figure 5.24: Surge motion spectrum for $v_i = 0.3$ m/s, $v_w = 12$ m/s and different ice thickness

5.3.3 Sway Motion

Sway motion time series are presented in Figures 5.25 and 5.26, while the statistical properties are presented in Figures 5.27 and 5.28. Due to the ice load in the y direction having a mean value close to 0, no substantial differences can be seen in the sway mean value. On the other hand, a more relevant effect is found in the sway motion standard deviation. Similarly to the surge motion, the sway motion oscillation are damped out by the ice load. However, the standard deviation increases again for $h_i = 0.8$ m/s for both the considered drifting speed. This effect is due to different frequency of the ice load for different speed and thickness. We can see that the damping effect is maximum when

$h_i = 0.4$ m for both the considered speed, while it is less relevant for the other thickness.

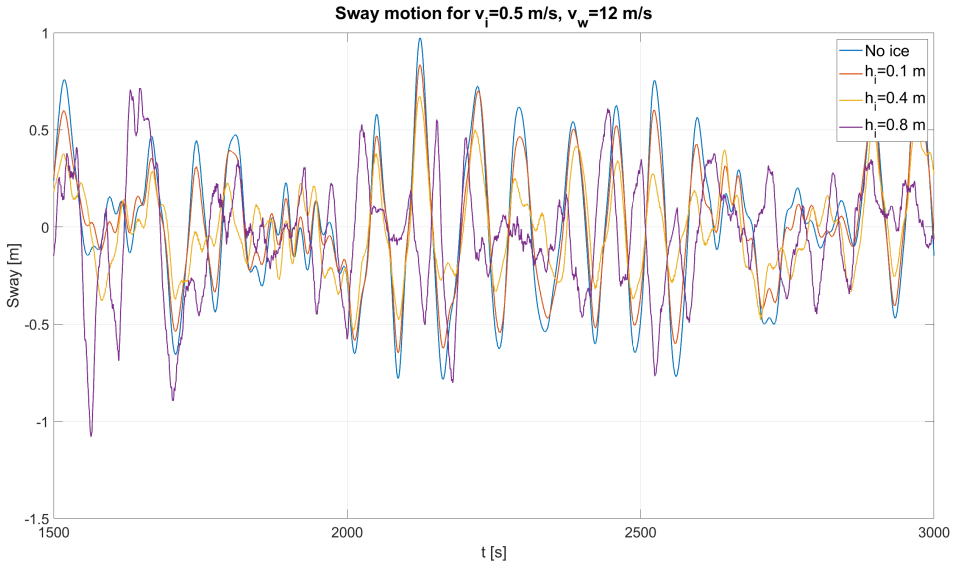

Figure 5.25: Sway motion time series for $v_i = 0.5$ m/s, $v_w = 12$ m/s and different ice thickness

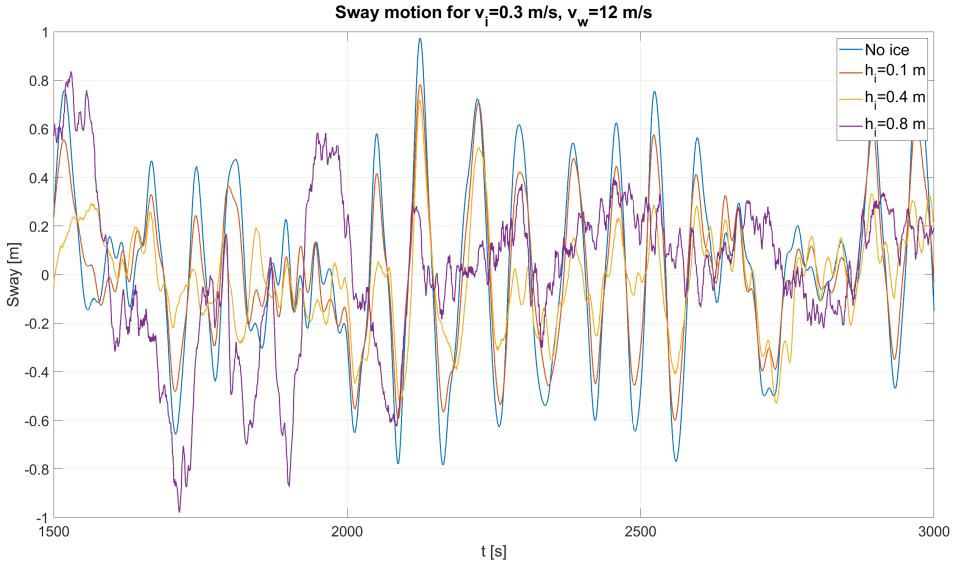

Figure 5.26: Sway motion time series for $v_i = 0.3$ m/s, $v_w = 12$ m/s and different ice thickness

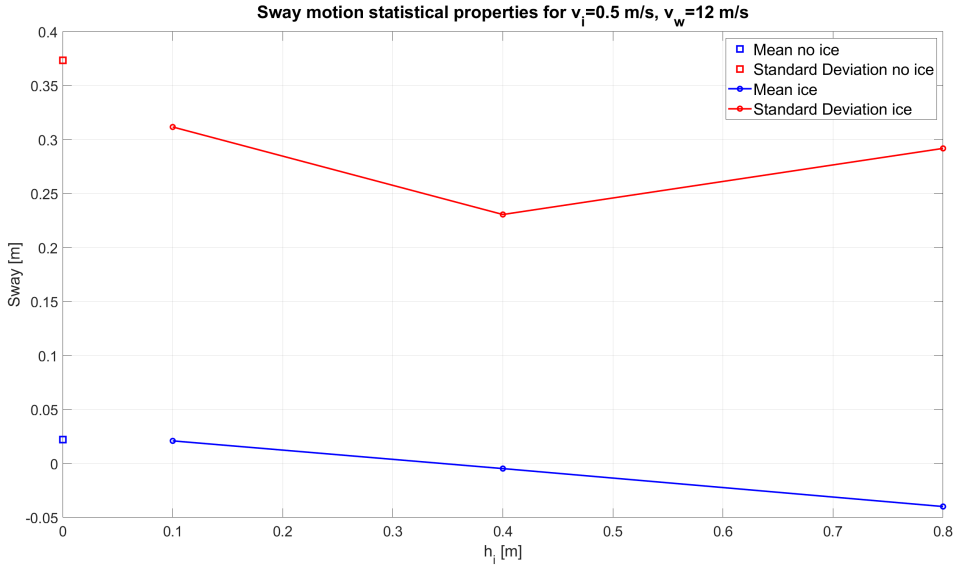

Figure 5.27: Sway motion statistical properties for $v_i = 0.5$ m/s, $v_w = 12$ m/s and different ice thickness

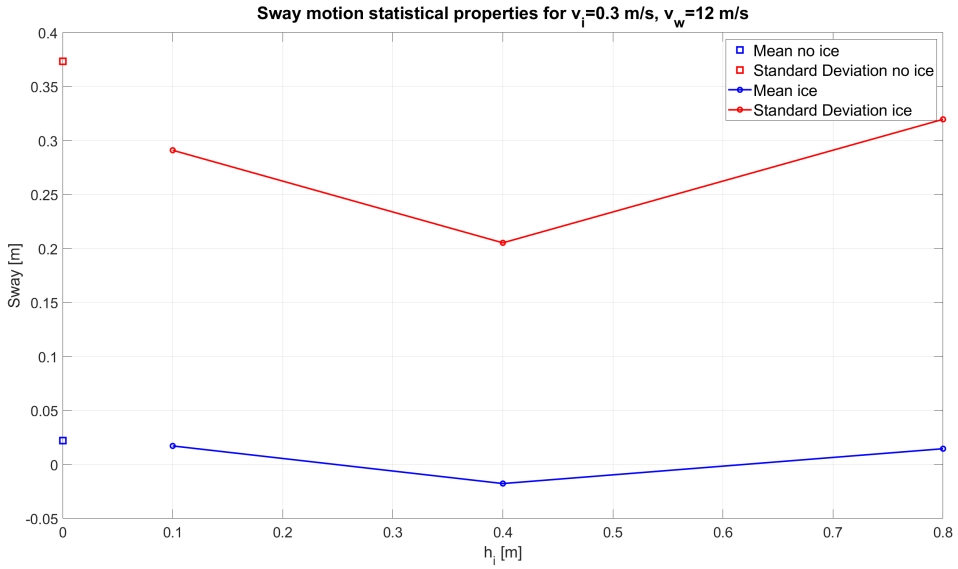

Figure 5.28: Sway motion statistical properties for $v_i = 0.3$ m/s, $v_w = 12$ m/s and different ice thickness

5.3.4 Roll Motion

Figures 5.29 and 5.30 present the roll motion time series, while Figures 5.31 and 5.32 present the statistical properties. Similarly to the sway motion, roll motion present an offset for the case with no ice, which is due to the forces induced by the wind turbine rotation. These forces are balanced by the ice load, thus resulting in a reduced mean value with the increasing ice thickness. Also, the standard deviation increases with the increasing thickness due to the cyclic nature of the ice load, which results in stronger oscillation. This effect is stronger when ice is moving faster and it can be seen also in the

roll motion spectrum shown in Figures 5.33 and 5.34.

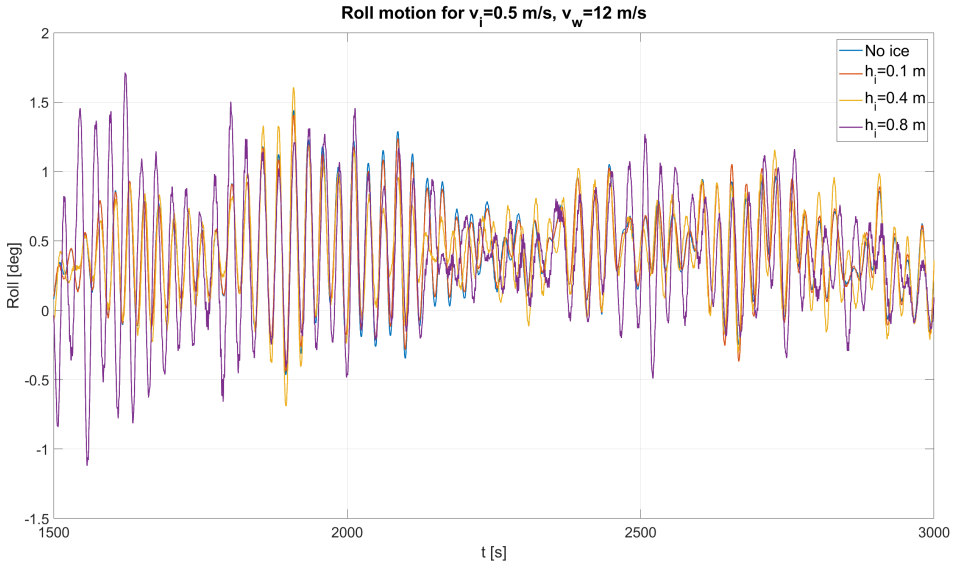

Figure 5.29: Roll motion time series for $v_i = 0.5$ m/s, $v_w = 12$ m/s and different ice thickness

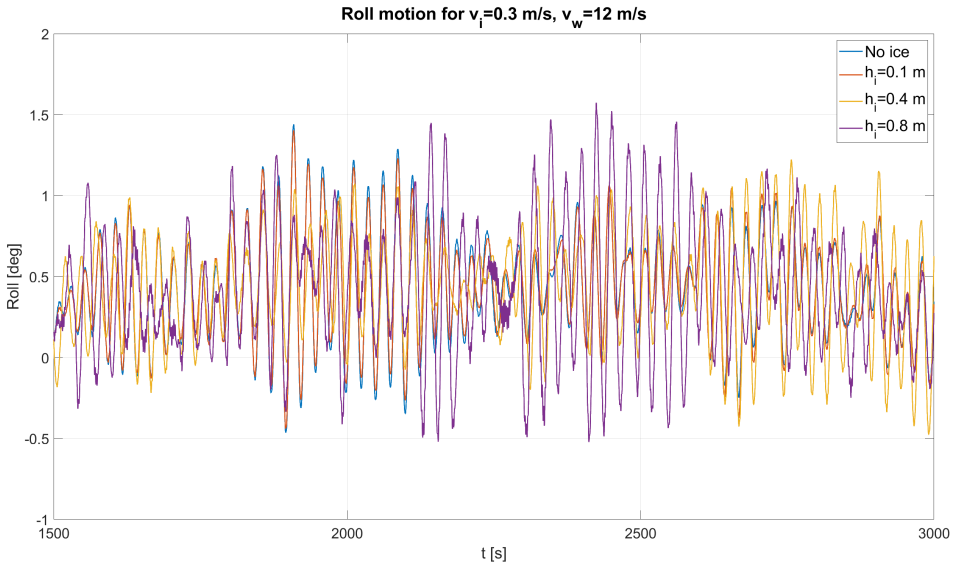

Figure 5.30: Roll motion time series for $v_i = 0.3$ m/s, $v_w = 12$ m/s and different ice thickness

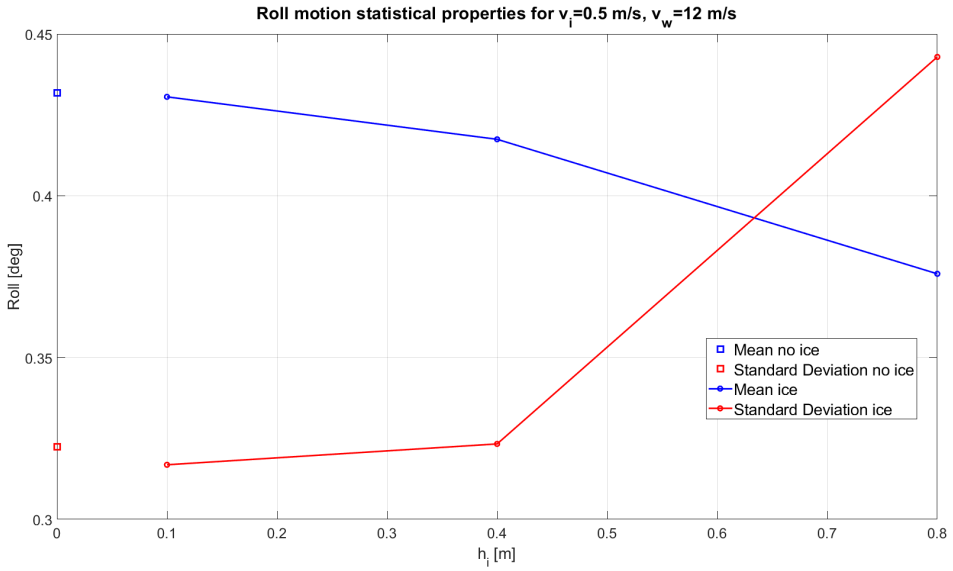

Figure 5.31: Roll motion statistical properties for $v_i = 0.5$ m/s, $v_w = 12$ m/s and different ice thickness

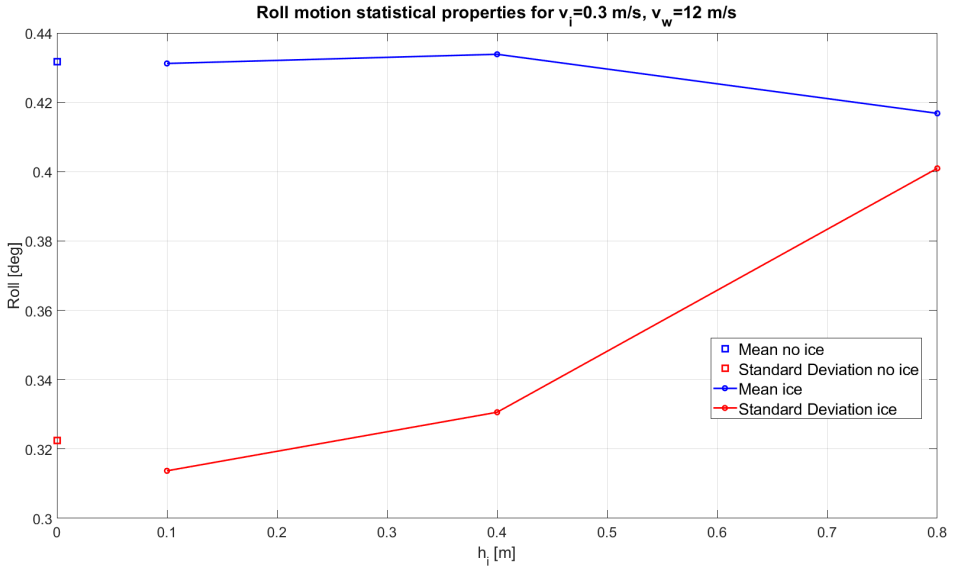

Figure 5.32: Roll motion statistical properties for $v_i = 0.3$ m/s, $v_w = 12$ m/s and different ice thickness

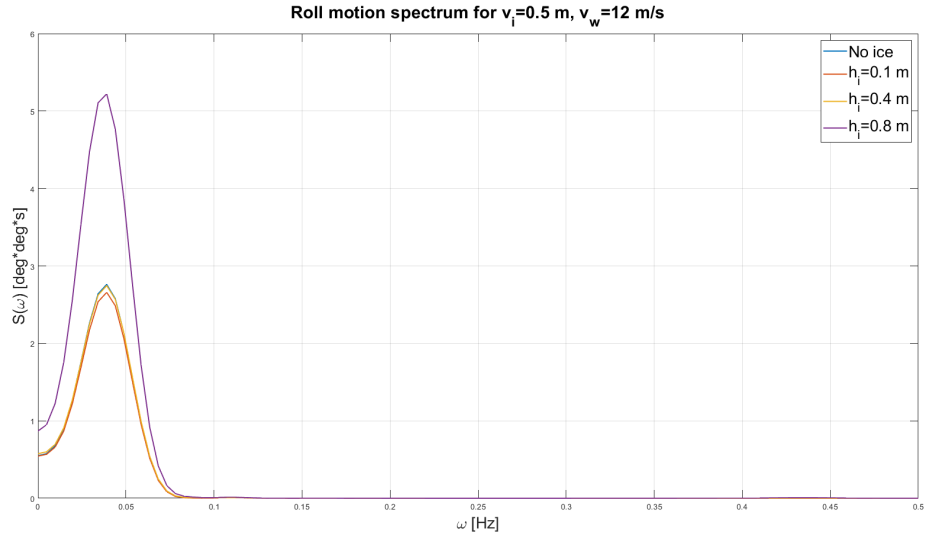

Figure 5.33: Roll motion spectrum for $v_i = 0.5$ m/s, $v_w = 12$ m/s and different ice thickness

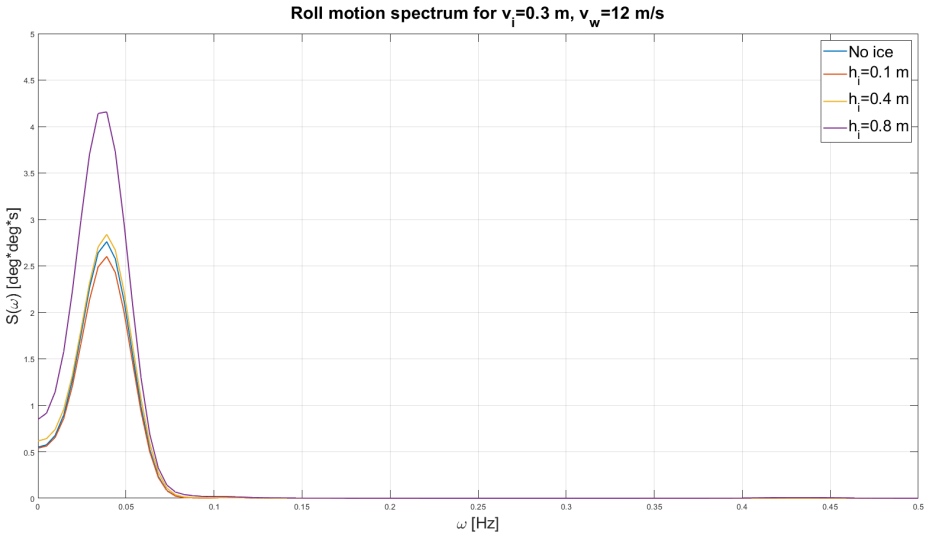

Figure 5.34: Roll motion spectrum for $v_i = 0.3$ m/s, $v_w = 12$ m/s and different ice thickness

5.3.5 Pitch Motion

Pitch motion time series are shown in Figures 5.35 and 5.36, while Figures 5.37 and 5.38 show the statistical properties. In this case, ice loads have very little effect on the results. This is due to the fact that the rotation around the y axis is dominated by the wind load acting on the wind turbine which is stronger then the ice load, as shown in the previous section. Therefore no substantial difference is noted in the different cases. Also the motion spectrum, shown in Figures 5.39 and 5.40, do not shows substantial differences when the ice load are applied, with the exception of the case with $v_i = 0.3$ m/s and $h_i = 0.8$ m, where a little amplification can be observed around 0.03 Hz.

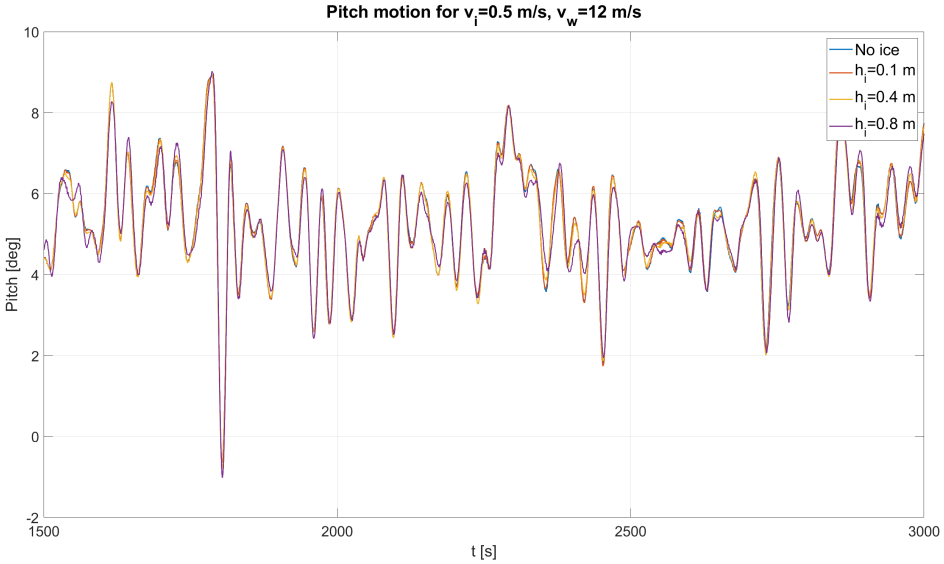

Figure 5.35: Pitch motion time series for $v_i = 0.5$ m/s, $v_w = 12$ m/s and different ice thickness

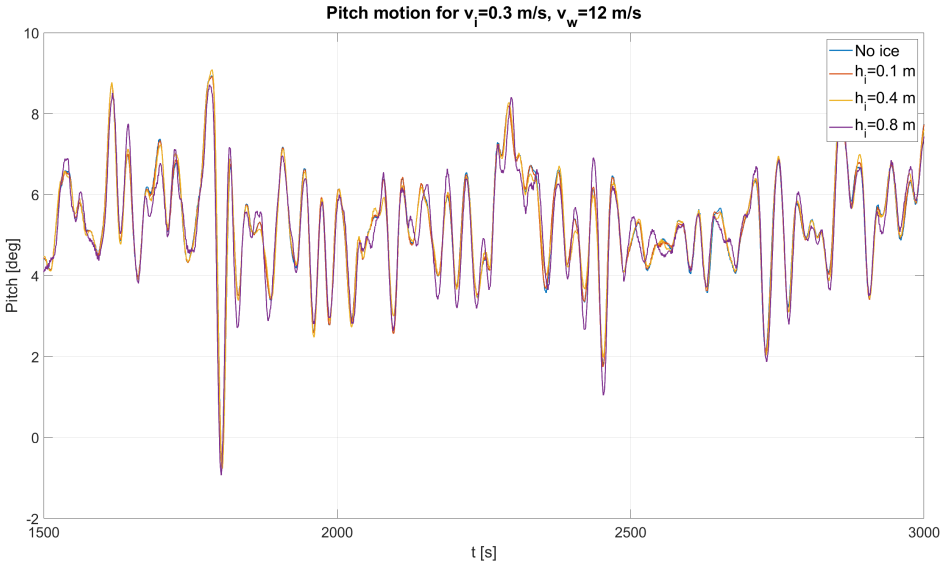

Figure 5.36: Pitch motion time series for $v_i = 0.3$ m/s, $v_w = 12$ m/s and different ice thickness

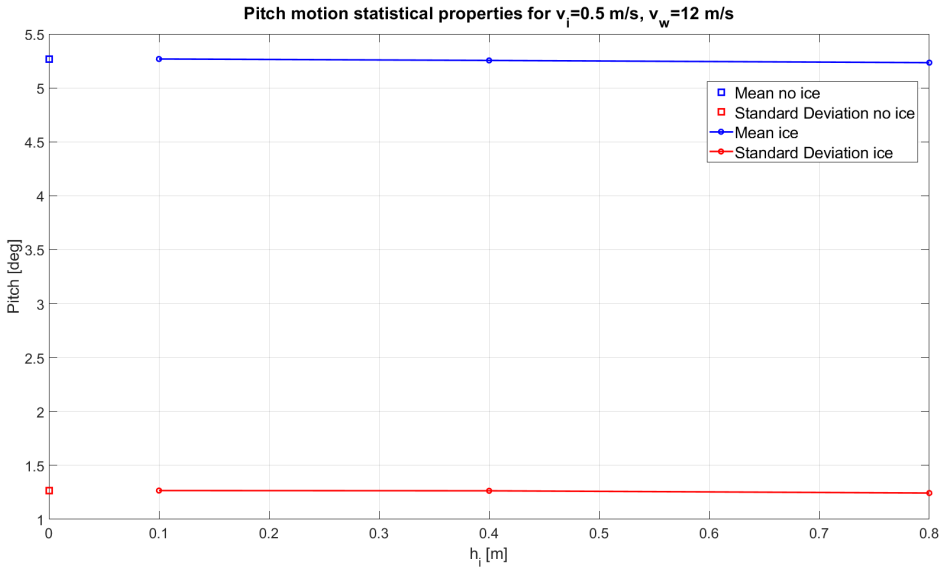

Figure 5.37: Pitch motion statistical properties for $v_i = 0.5$ m/s, $v_w = 12$ m/s and different ice thickness

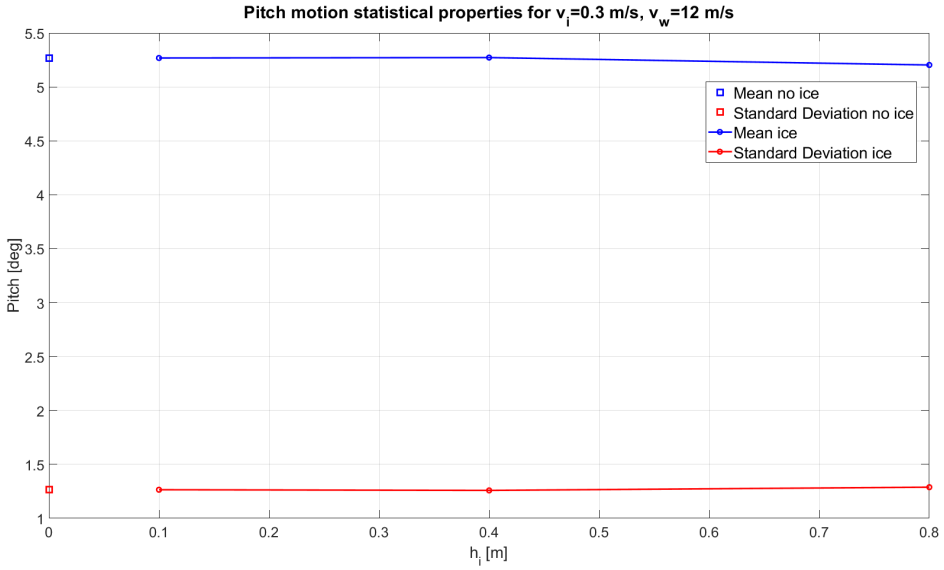

Figure 5.38: Pitch motion statistical properties for $v_i = 0.3$ m/s, $v_w = 12$ m/s and different ice thickness

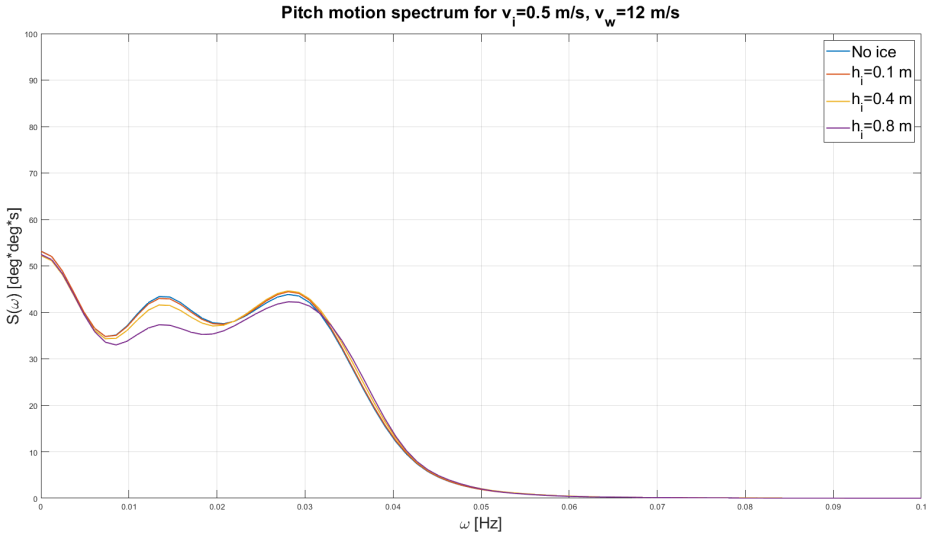

Figure 5.39: Pitch motion spectrum for $v_i = 0.5$ m/s, $v_w = 12$ m/s and different ice thickness

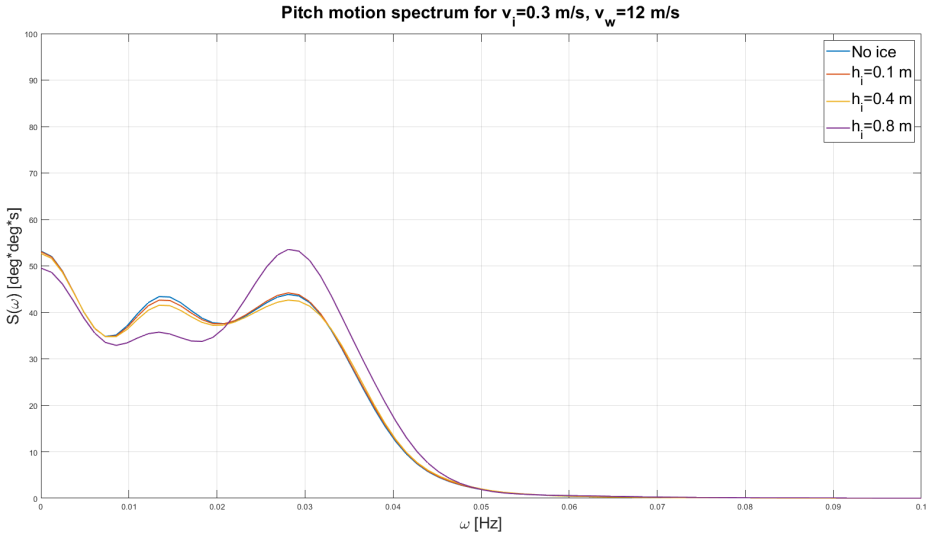

Figure 5.40: Pitch motion spectrum for $v_i = 0.3$ m/s, $v_w = 12$ m/s and different ice thickness

5.3.6 Yaw Motion

Yaw motion time series are presented in Figures 5.41 and 5.42, while the statistical properties are presented in Figures 5.43 and 5.44. Looking at the time series we can we that ice load tend to reduce the amplitude of the oscillation without affecting the frequency, with the exception of the case with $h_i = 0.8$, which strongly deviate from the other cases especially for $v_i = 0.3$. Similarly to what happens in the case of the roll motion this may be due to a resonant effect. Moreover, increased ice thickness appears to reduce the yaw mean value due to the ice induced moment around z axis having zero mean value.

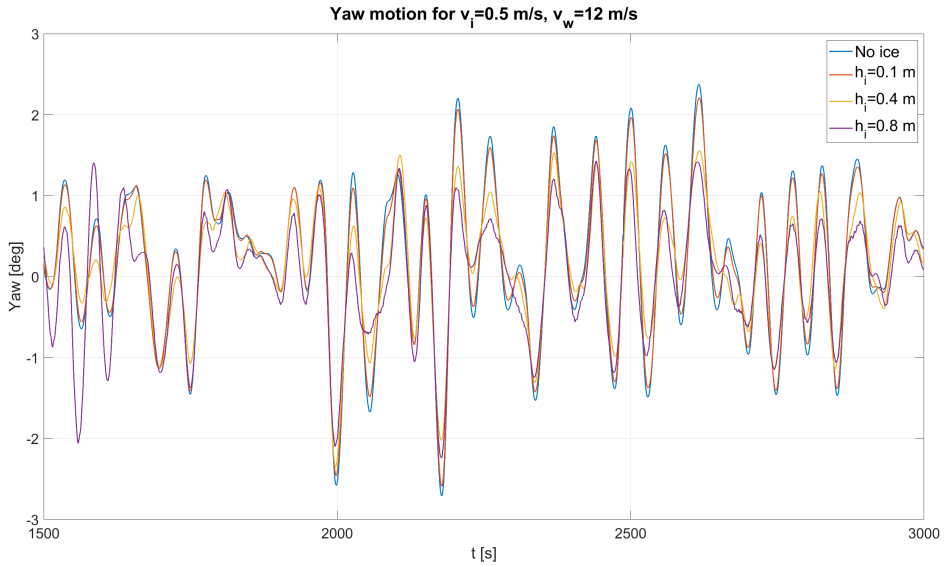

Figure 5.41: Yaw motion time series for $v_i = 0.5$ m/s, $v_w = 12$ m/s and different ice thickness

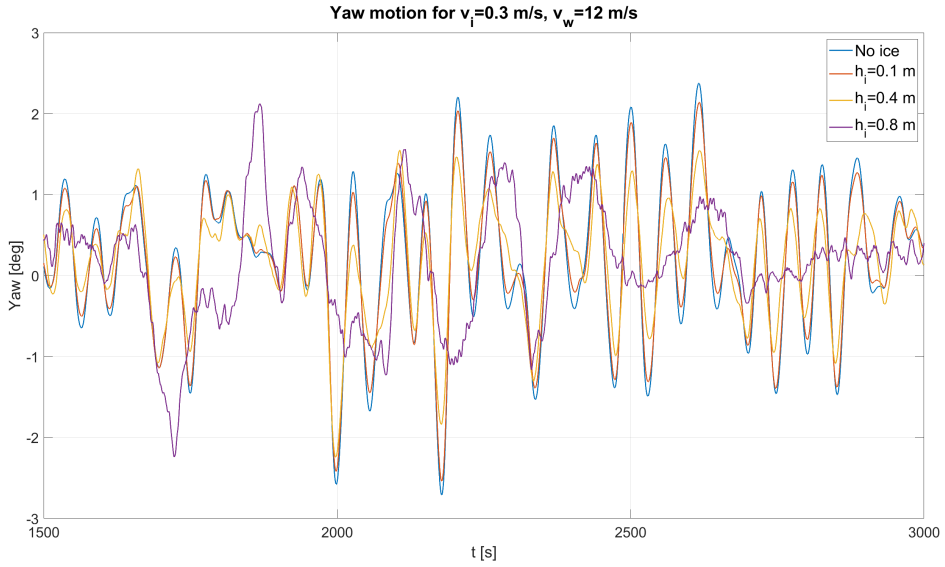

Figure 5.42: Yaw motion time series for $v_i = 0.3$ m/s, $v_w = 12$ m/s and different ice thickness

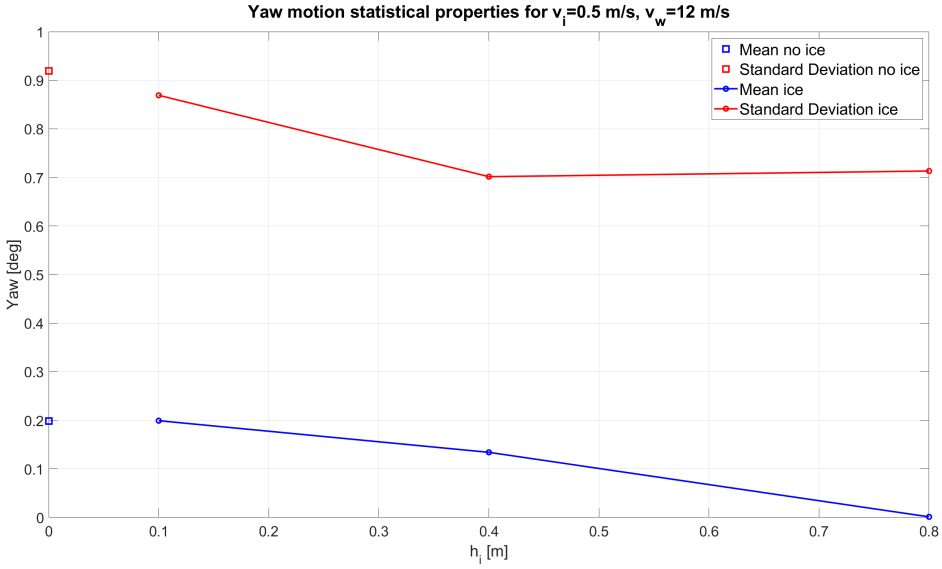

Figure 5.43: Yaw motion statistical properties for $v_i = 0.5$ m/s, $v_w = 12$ m/s and different ice thickness

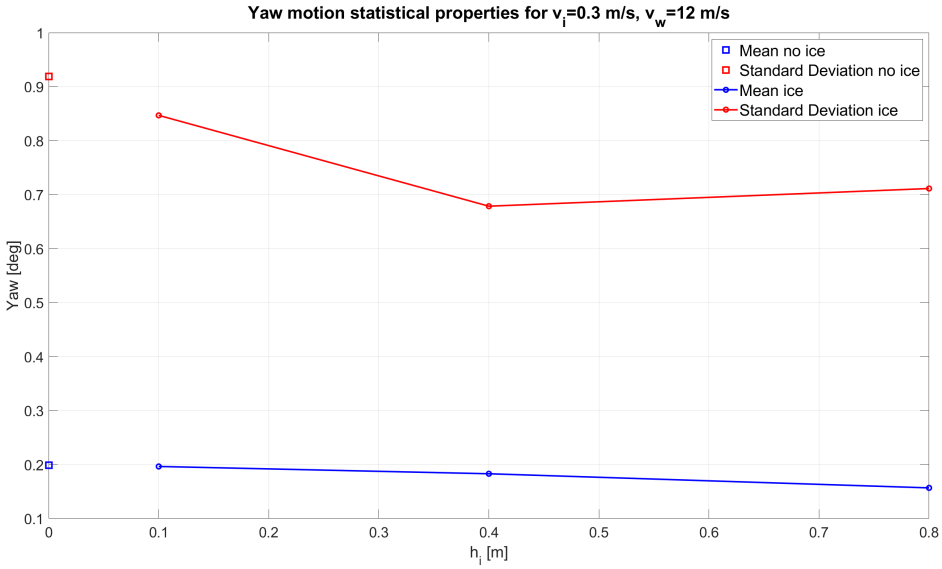

Figure 5.44: Yaw motion statistical properties for $v_i = 0.3$ m/s, $v_w = 12$ m/s and different ice thickness

5.4 Ice Drifting Speed Influence

In order to describe the influence of the ice drifting speed, we present two sets of conditions with ice speed equal to $v_i = 0.1$ m/s, $v_i = 0.3$ m/s and $v_i = 0.5$ m/s. A case with no ice is evaluated too. The sets differ in the ice thickness, which is taken as $h_i = 0.8$ m and $h_i = 0.4$ m/s, while the wind speed is $v_w = 12$ m/s for all cases.

5.4.1 Ice and Wind Loads Comparison

Figure 5.45 shows a comparison between the aerodynamic thrust on the wind turbine rotor and the ice force in the x direction for different ice drifting speed. It should be noted that only the one time series of the aerodynamic thrust, corresponding to $v_i = 0.5$ m/s, is provided, since it results almost unaffected by the ice loads. In this case the considered ice thickness always equal to $h_i = 0.8$ m and therefore the ice load magnitude is always comparable with the wind thrust. In fact, the ice drifting speed has a relatively lower impact on the ice load mean value then the ice thickness: $F_{x,mean} = 786$ kN for $v_i = 0.1$ m/s, $F_{x,mean} = 952$ kN for $v_i = 0.3$ m/s and $F_{x,mean} = 1140$ kN for $v_i = 0.5$ m/s, compared to a mean thrust force equal to $T = 1200$ kN. On the other hand, ice drifting speed has a relevant influence on the ice load frequency, which increases when the ice is moving faster as is also shown by the load spectrum in Figure 5.46. It can also be observed that the ice load for $v_i = 0.1$ is less regular the the other cases, with the load dropping to 0 multiple times. This is due to the issues described in §5.2.1, concerning the fact that the when the ice is slow and thick, the contact forces may not be high enough to trigger the breaking process.

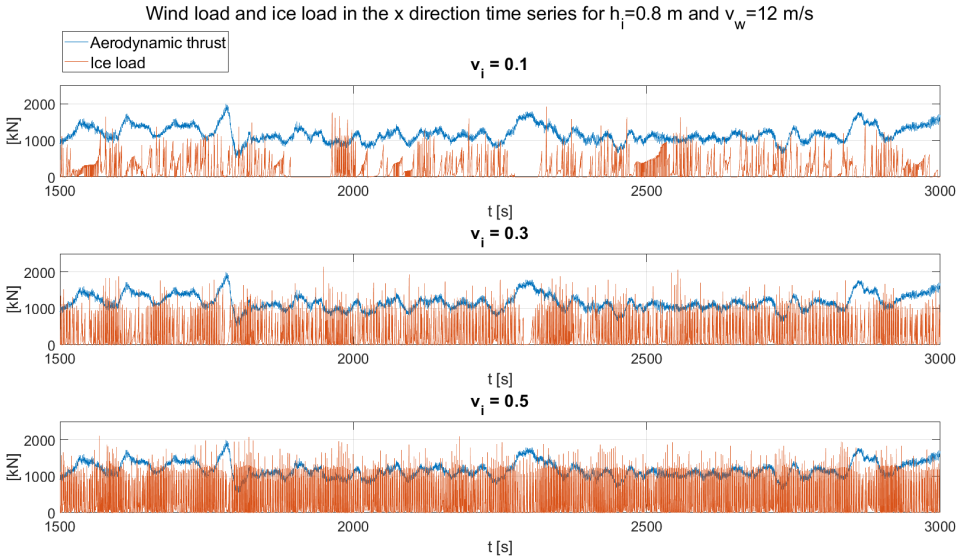

Figure 5.45: Ice and wind loads in the x direction time series comparison for $h_i = 0.5$ m, $v_w = 12$ m/s and different drifting speed

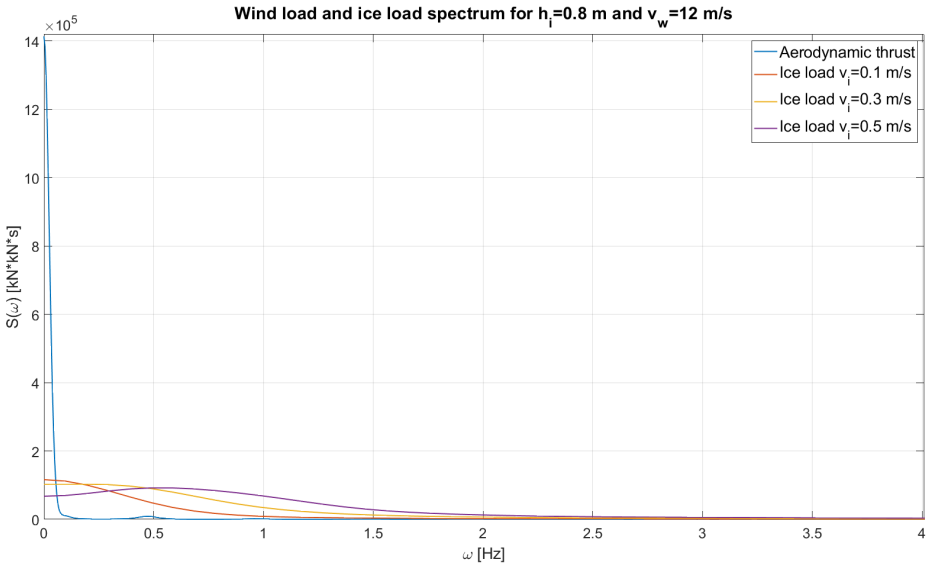

Figure 5.46: Ice and wind loads in the x direction spectrum comparison for $h_i = 0.8$ m, $v_w = 12$ m/s and different drifting speed

A comparison between ice and wind load on the y direction is shown in Figure 5.47. In this case the ice load are always dominant regardless of the ice speed, since the ice thickness is the most relevant parameter in terms of ice load magnitude. As already mentioned, ice drifting speed mainly affect the loading frequency. As can be seen in Figure 5.48, the peak frequency increases with the ice speed.

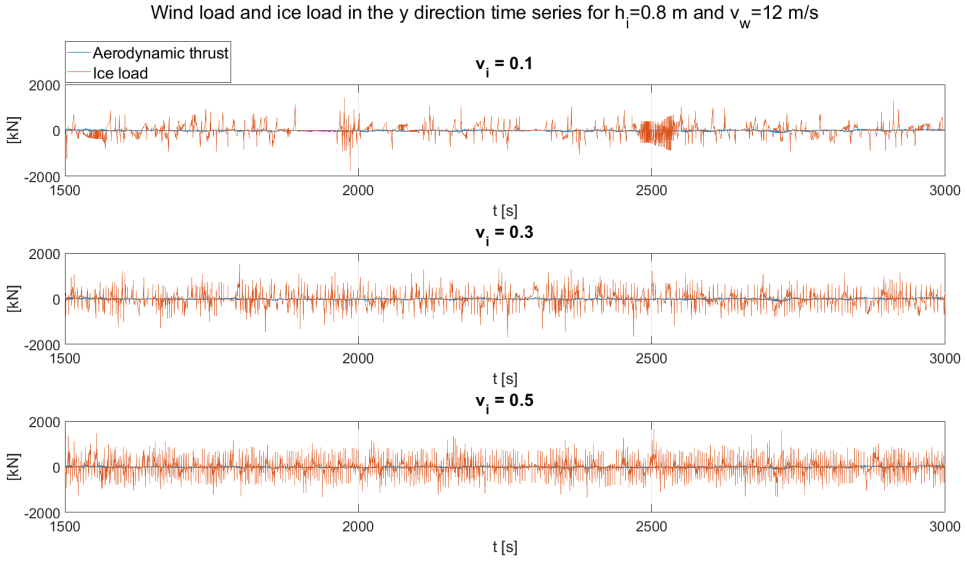

Figure 5.47: Ice and wind loads in the y direction time series comparison for $h_i = 0.5$ m, $v_w = 12$ m/s and different drifting speed

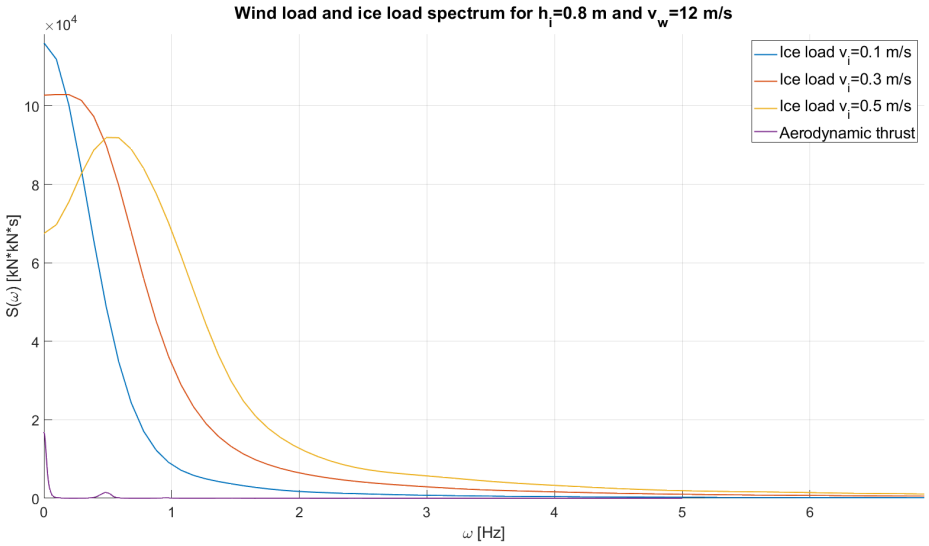

Figure 5.48: Ice and wind loads in the y direction spectrum comparison for $h_i = 0.8$ m, $v_w = 12$ m/s and different drifting speed

5.4.2 Surge Motion

Surge motion time series are shown in Figures 5.49 and 5.50, while the statistical properties are shown in Figures 5.51 and 5.52. The platform offset in the x direction increases with the ice drifting speed, but the effect appears to be less relevant then the one induced by the increased ice thickness. In fact, the surge mean value shows only little variation with for the $h_i = 0.4$ m case, since the ice force is lower in this case. However, we can observe that for $h_i = 0.4$ m the standard deviation increases for increased ice speed, while the opposite happens for $h_i = 0.8$ m, i.e. the surge standard deviation decreases for increased ice speed. It is also interesting to notice that the standard deviation is higher when no ice is considered, showing that the ice provides a damping effect to the platform motion in the x direction. This is also shown by the surge motion spectrum, Figures 5.53 and 5.54. In the spectrum we can also observe that the damping effect of ice ice stronger for thicker and slower ice. The only exception is the case with $v_i = 0.1$ m/s and $h_i = 0.8$ m which shows amplification at low frequency.

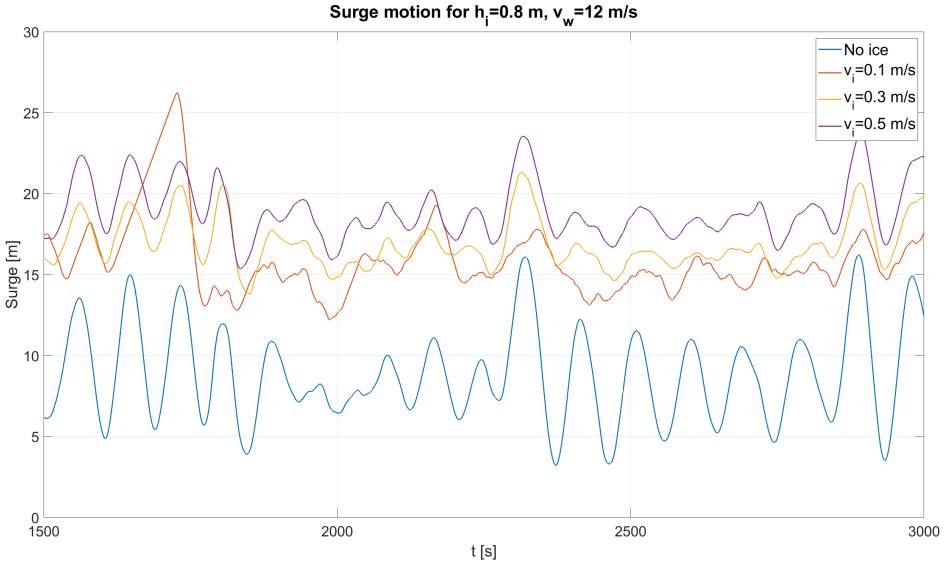

Figure 5.49: Surge motion time series for $h_i = 0.8$ m, $v_w = 12$ m/s and different ice drifting speed

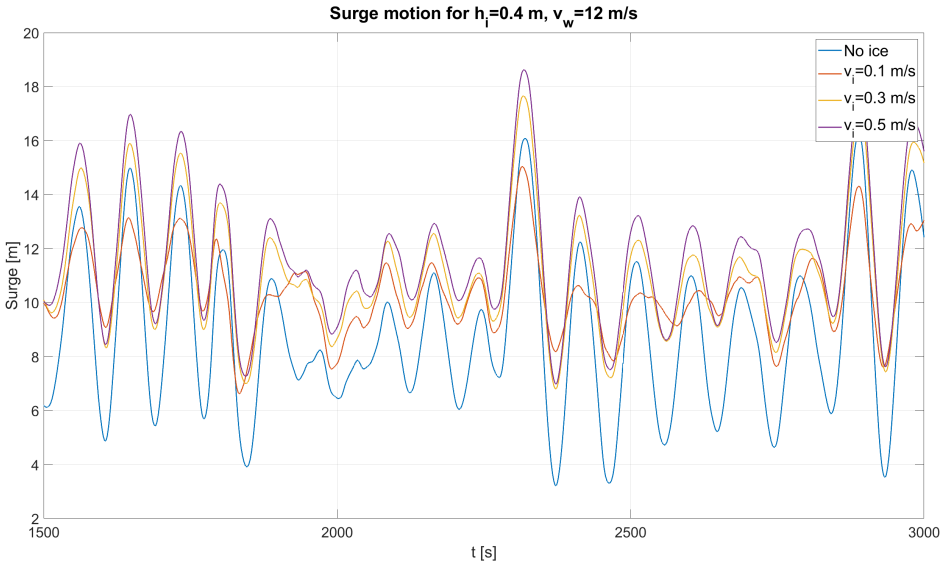

Figure 5.50: Surge motion time series for $h_i = 0.4$ m, $v_w = 12$ m/s and different ice drifting speed

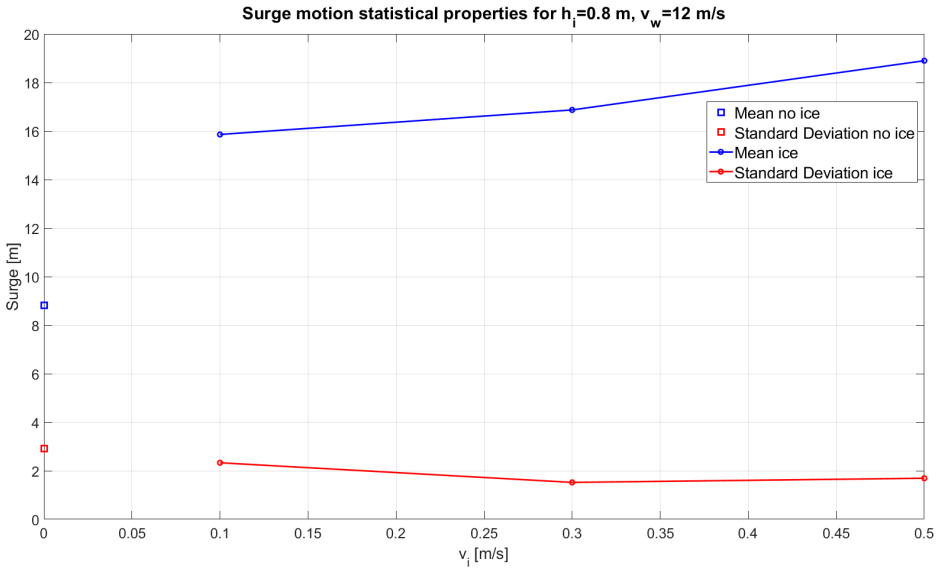

Figure 5.51: Surge motion statistical properties for $h_i = 0.8$ m, $v_w = 12$ m/s and different ice drifting speed

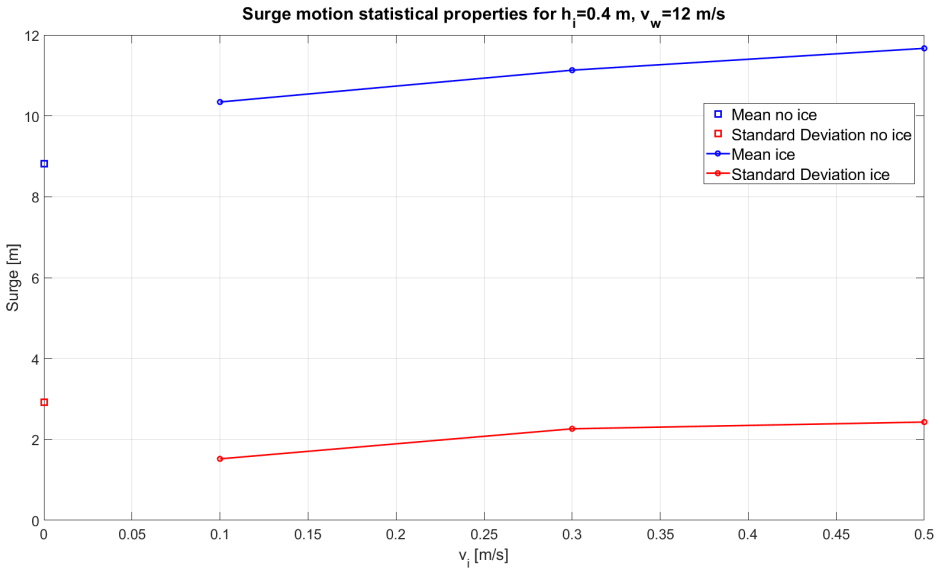

Figure 5.52: Surge motion statistical properties for $h_i = 0.4$ m, $v_w = 12$ m/s and different ice drifting speed

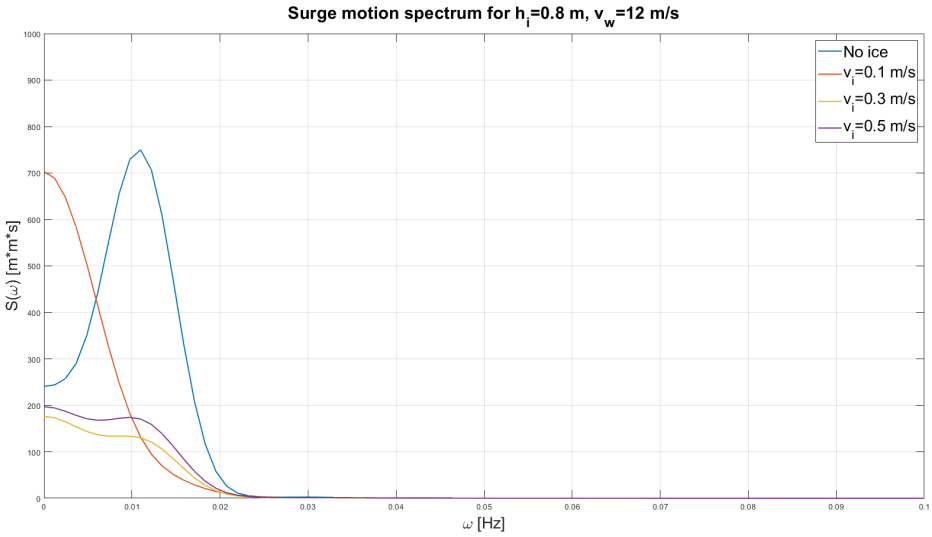

Figure 5.53: Surge motion spectrum for $h_i = 0.8$ m, $v_w = 12$ m/s and different ice drifting speed

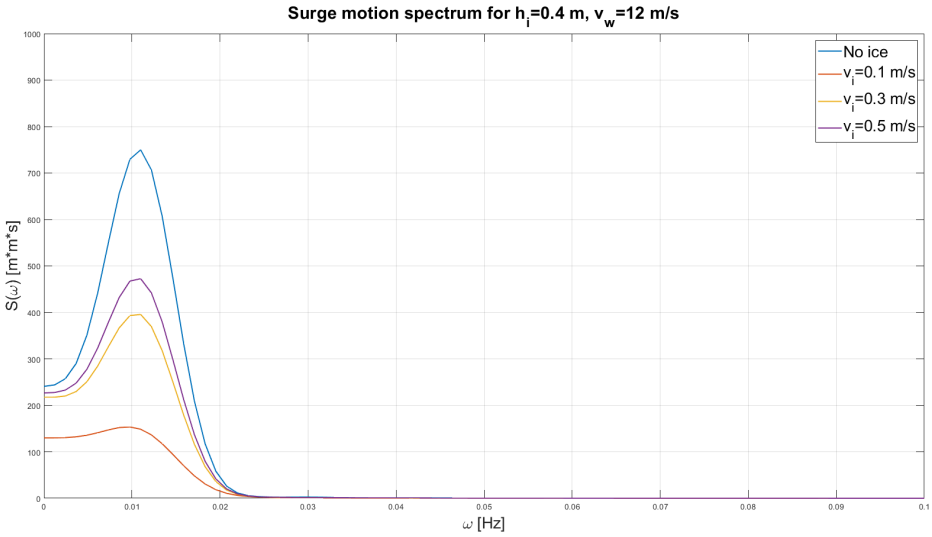

Figure 5.54: Surge motion spectrum for $h_i = 0.4$ m, $v_w = 12$ m/s and different ice drifting speed

5.4.3 Sway Motion

Figures 5.55 and 5.56 present the sway motion time series, while Figures 5.27 and 5.28 present the statistical properties. In this case, the motion exhibits different behavior for the two thicknesses. For $h_i = 0.8$ m, the mean value and standard deviation do not show relevant differences from the no ice case, with the only exception of $v_i = 0.1$ m/s. However, the times series are different from each other, with the one corresponding to the ice load having more oscillation as a result of the cyclic ice loads. On the other hand, for $h_i = 0.4$ m the time series corresponding to the case with are closer to each other but the differ from the no wind case, particularly, the standard deviation is reduced for such cases as a

result of the ice damping action on the platform motion.

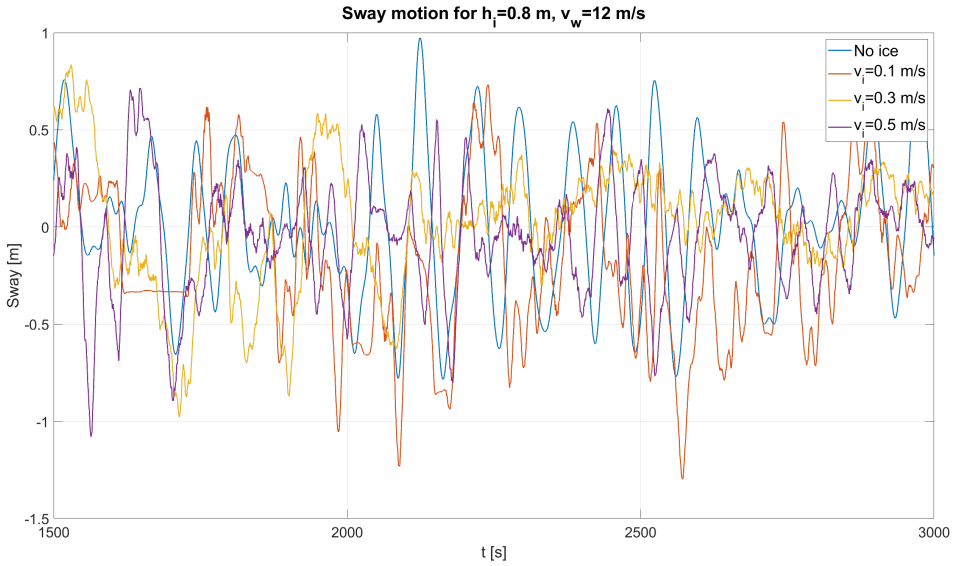

Figure 5.55: Sway motion time series for $h_i = 0.8$ m, $v_w = 12$ m/s and different ice drifting speed

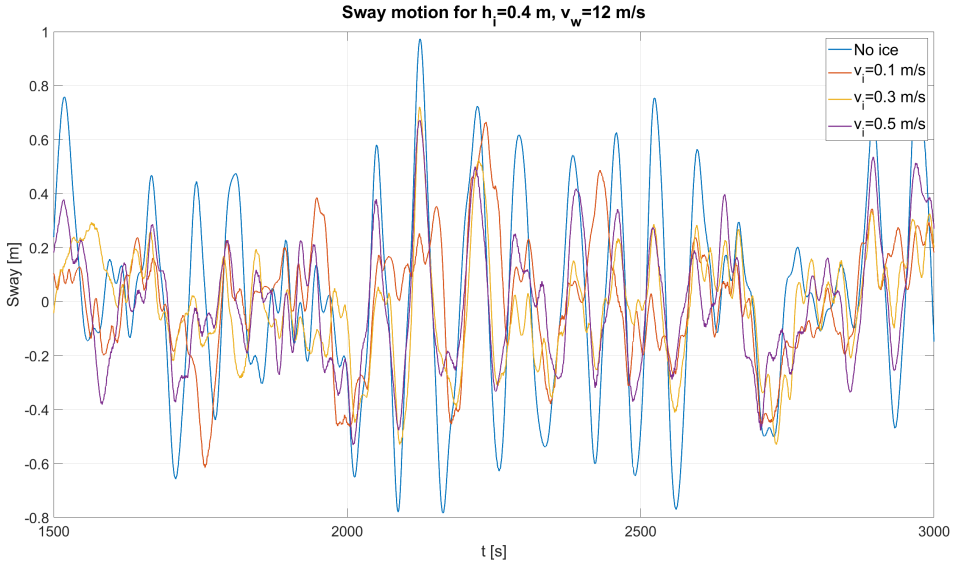

Figure 5.56: Sway motion time series for $h_i = 0.4$ m, $v_w = 12$ m/s and different ice drifting speed

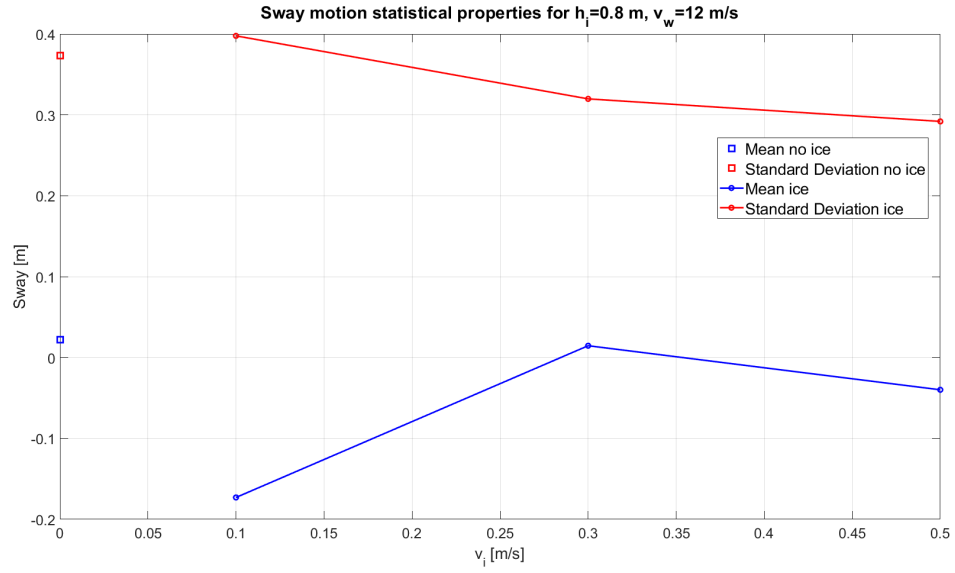

Figure 5.57: Sway motion statistical properties for $h_i = 0.8$ m, $v_w = 12$ m/s and different ice drifting speed

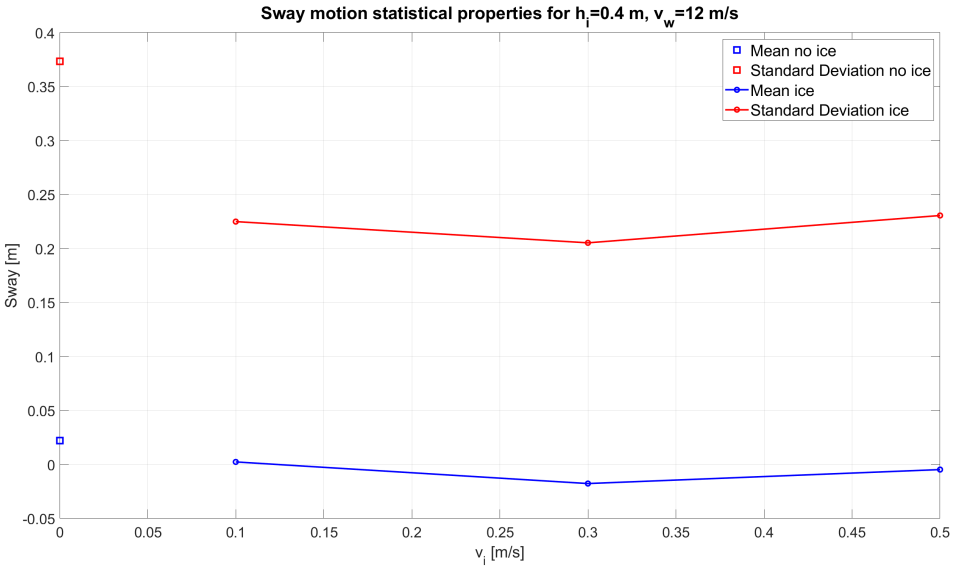

Figure 5.58: Sway motion statistical properties for $h_i = 0.4$ m, $v_w = 12$ m/s and different ice drifting speed

5.4.4 Roll motion

Figures 5.59 and 5.60 show the roll motion times series while the statistical properties are shown in Figures 5.61 and 5.62. The ice loads have no relevant effect on the roll mean value or on its frequency, but an important effect can be seen in the oscillations amplitude and therefore in its standard deviation. Particularly for the case of $v_i = 0.1$ m/s and $h_i = 0.8$ m, a strong resonant effect can be seen as shown also by the roll motion spectrum in Figure 5.63 and 5.64. For this case, an amplification of almost 7 times can be seen in the motion. This is due to the fact that, for that particular case, the frequency of the load

(both force in the x direction and moment around the y axis) matches the roll natural frequencies of the platform (corresponding to a period of approximately 27 s) and generate stronger oscillations.

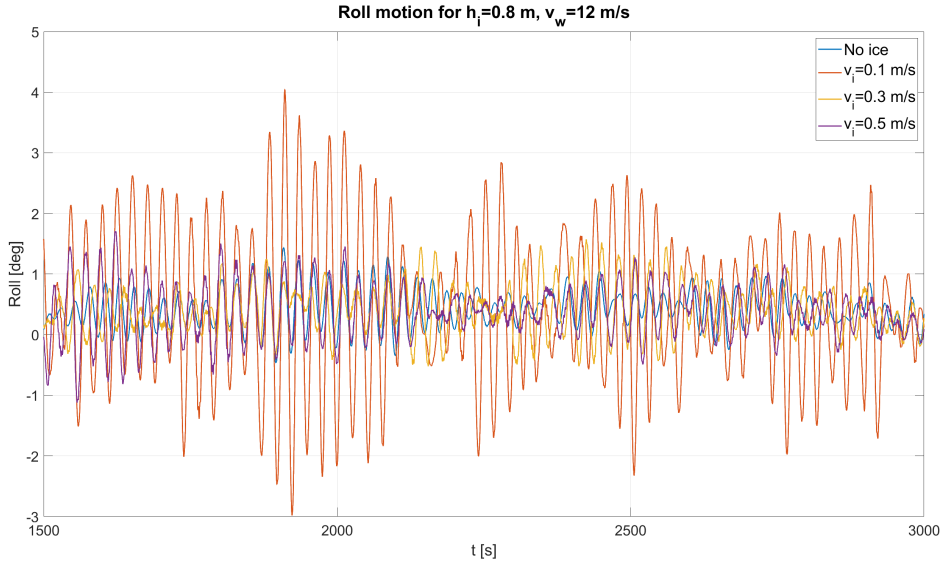

Figure 5.59: Roll motion time series for $h_i = 0.8$ m, $v_w = 12$ m/s and different ice drifting speed

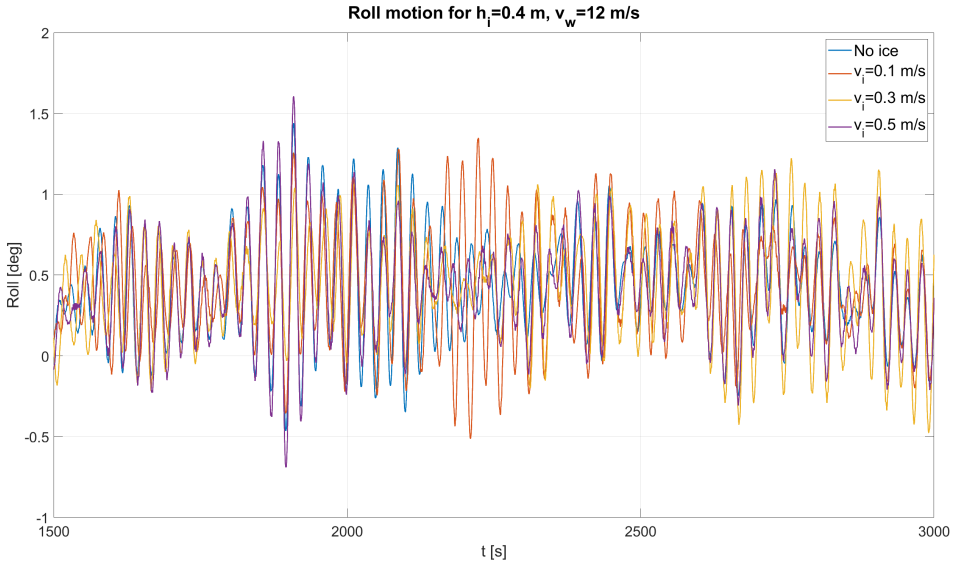

Figure 5.60: Roll motion time series for $h_i = 0.4$ m, $v_w = 12$ m/s and different ice drifting speed

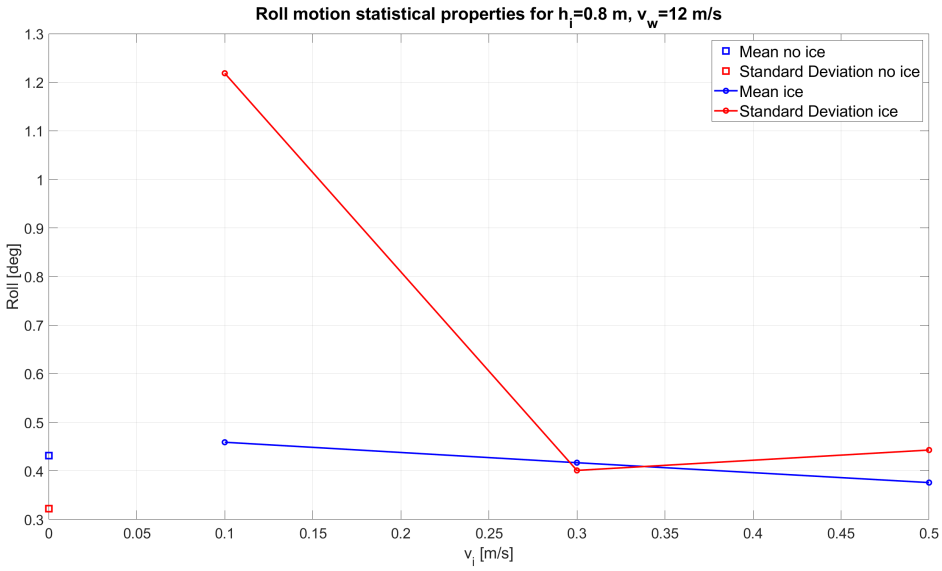

Figure 5.61: Roll motion statistical properties for $h_i = 0.8$ m, $v_w = 12$ m/s and different ice drifting speed

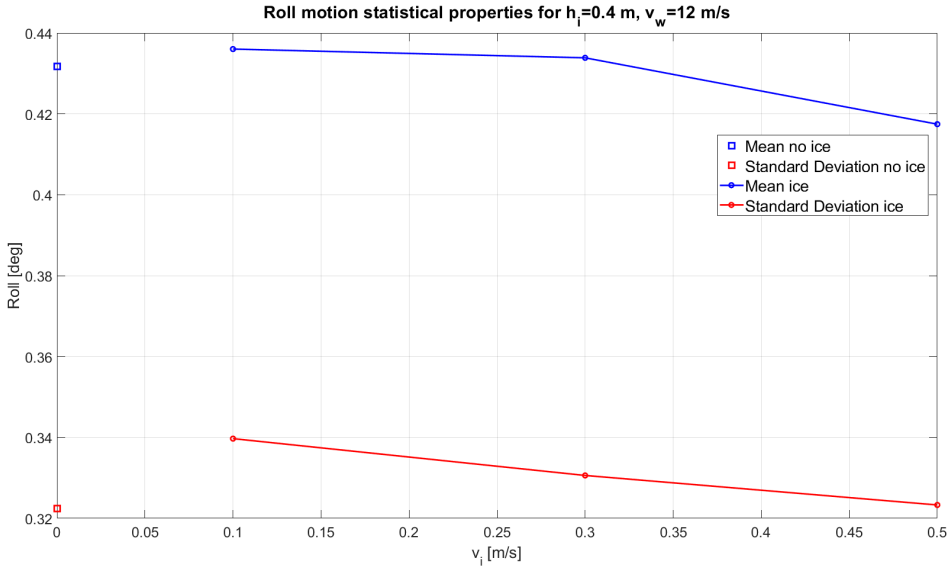

Figure 5.62: Roll motion statistical properties for $h_i = 0.4$ m, $v_w = 12$ m/s and different ice drifting speed

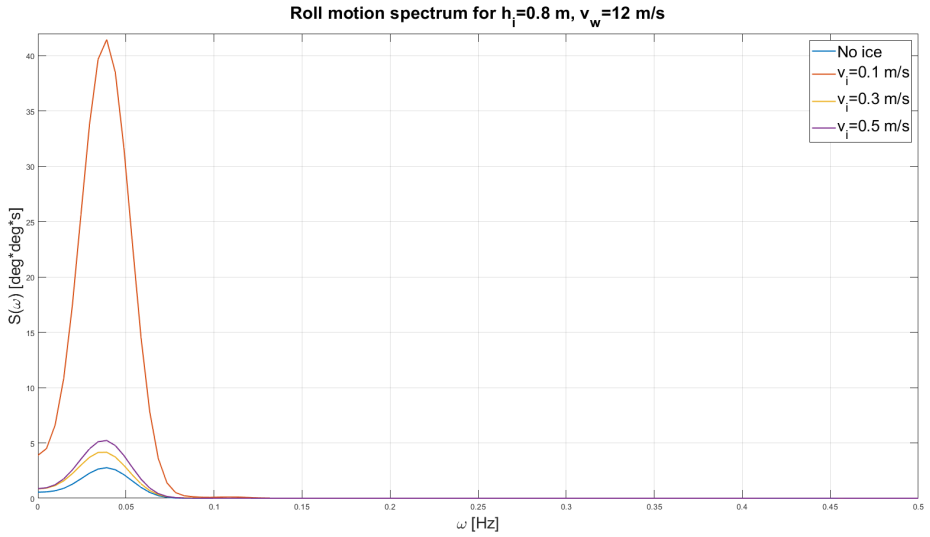

Figure 5.63: Roll motion spectrum for $h_i = 0.8$ m, $v_w = 12$ m/s and different ice drifting speed

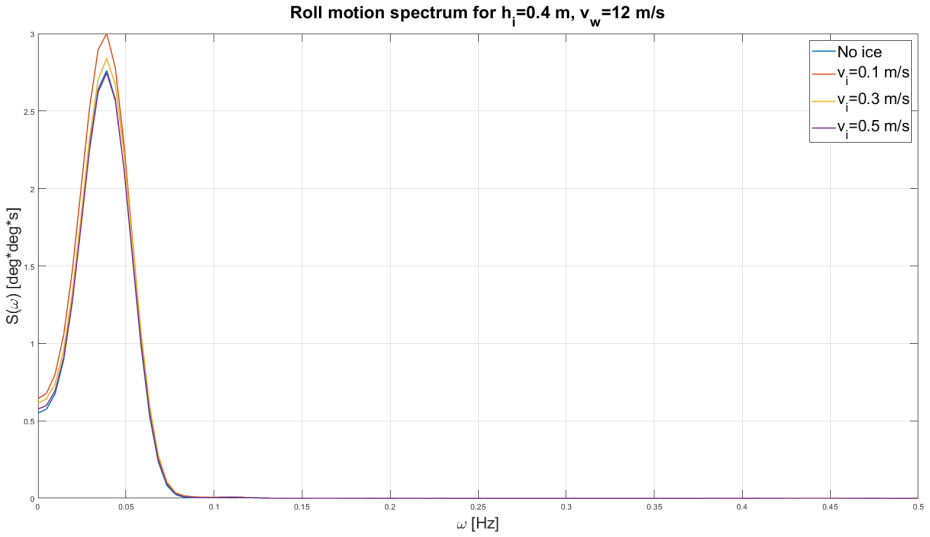

Figure 5.64: Roll motion spectrum for $h_i = 0.4$ m, $v_w = 12$ m/s and different ice drifting speed

5.4.5 Pitch Motion

The pitch motion time series and statistical properties are shown in Figure 5.65 to 5.68. We can clearly see how the pitch motion is dominated by the wind load, particularly for the case with $h_i = 0.4$ m. In fact, in this case the ice load are too little compared to the wind load for it to have a substantial effect on the platform Pitch. For $h_i = 0.8$ m some deviation can be seen between the case with no ice and the other, but is still not as relevant as other cases. Similarly to the roll motion, the case with $v_i = 0.1$ m/s and $h_i = 0.8$ is the one showing the greater difference from the no ice case, as can be observed also by the spectrum in Figures 5.69 and 5.70. In this case a relevant amplification can

be seen around 0.03 Hz also for $v_i = 0.3$ m/s and $h_i = 0.8$.

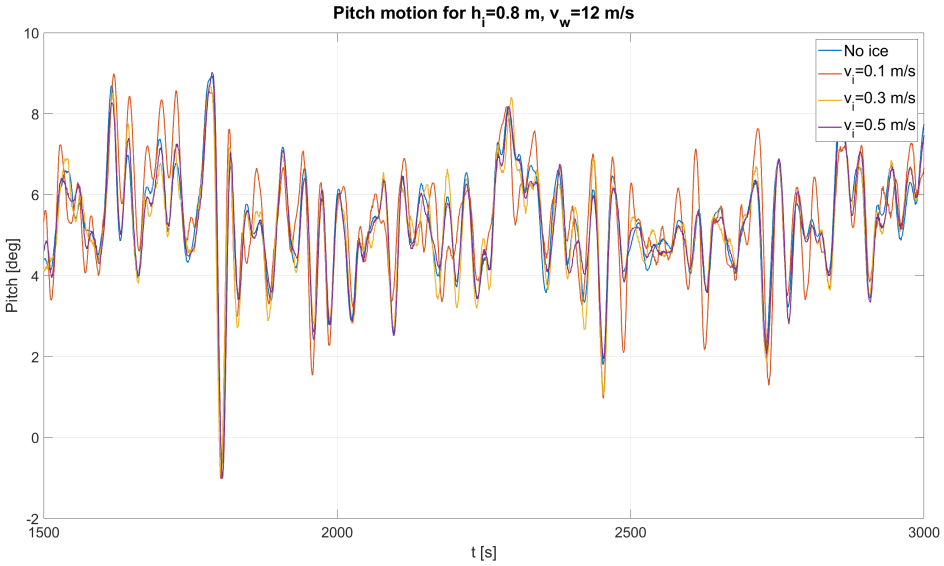

Figure 5.65: Pitch motion time series for $h_i = 0.8$ m, $v_w = 12$ m/s and different ice drifting speed

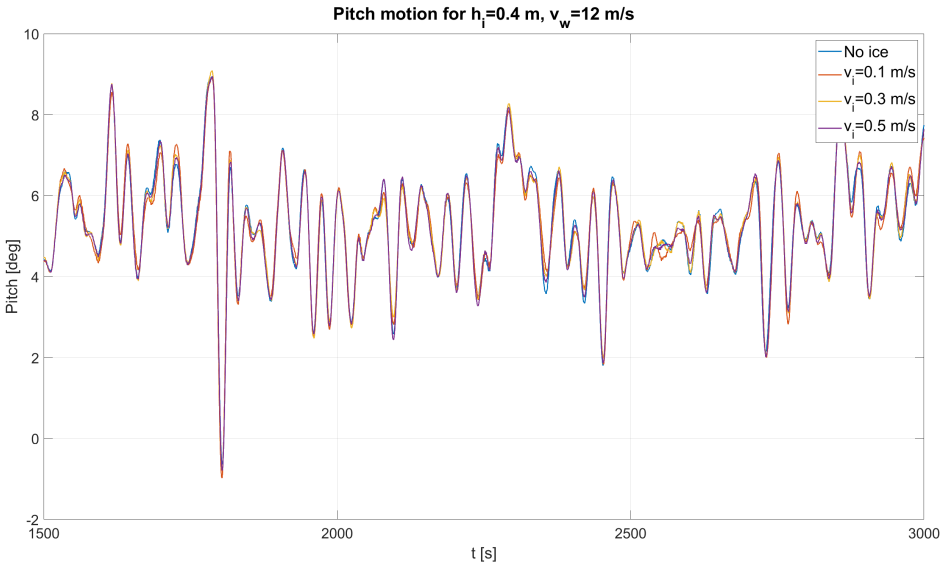

Figure 5.66: Pitch motion time series for $h_i = 0.4$ m, $v_w = 12$ m/s and different ice drifting speed

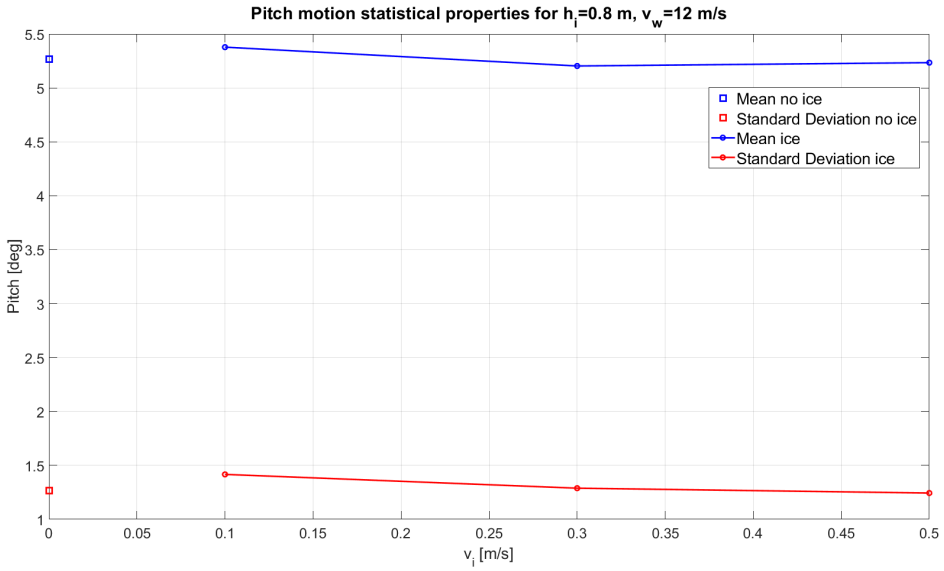

Figure 5.67: Pitch motion statistical properties for $h_i = 0.8$ m, $v_w = 12$ m/s and different ice drifting speed

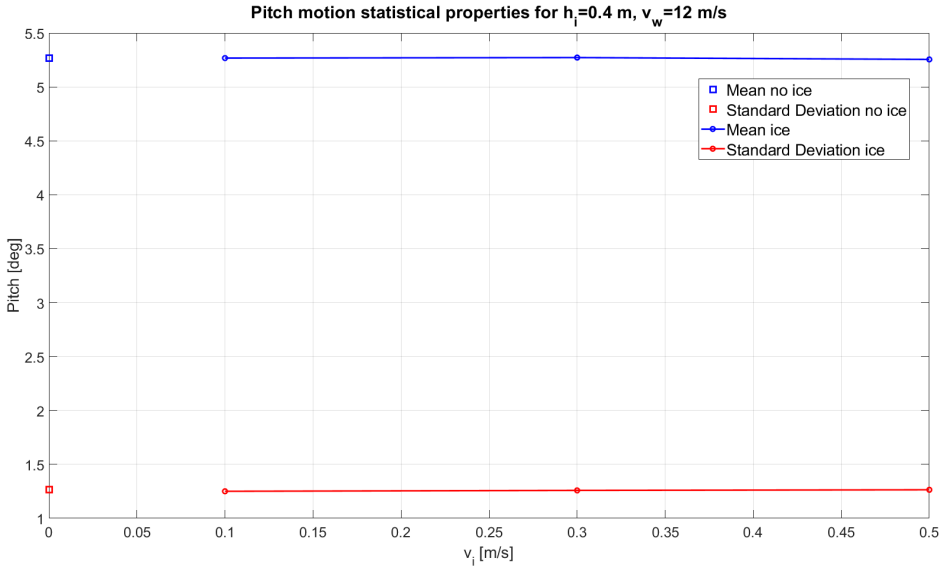

Figure 5.68: Pitch motion statistical properties for $h_i = 0.4$ m, $v_w = 12$ m/s and different ice drifting speed

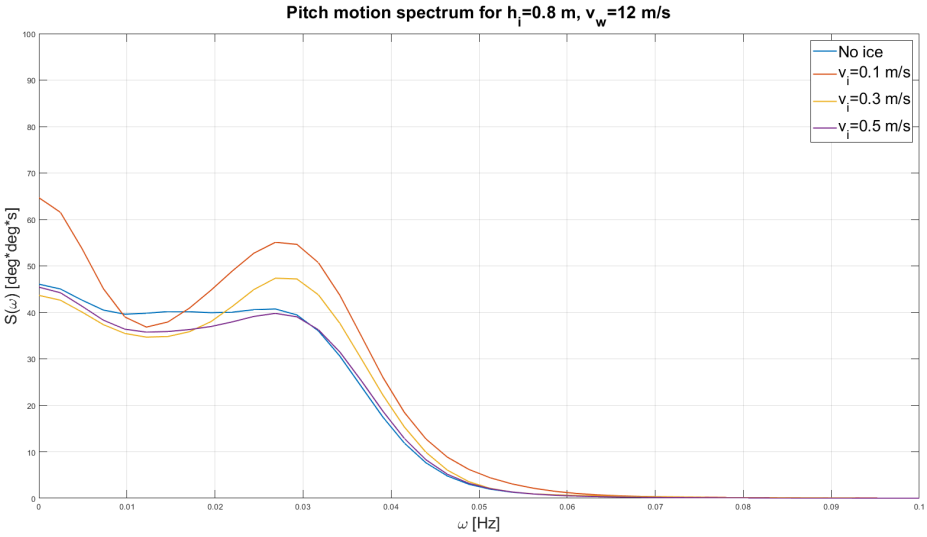

Figure 5.69: Pitch motion spectrum for $h_i = 0.8$ m, $v_w = 12$ m/s and different ice drifting speed

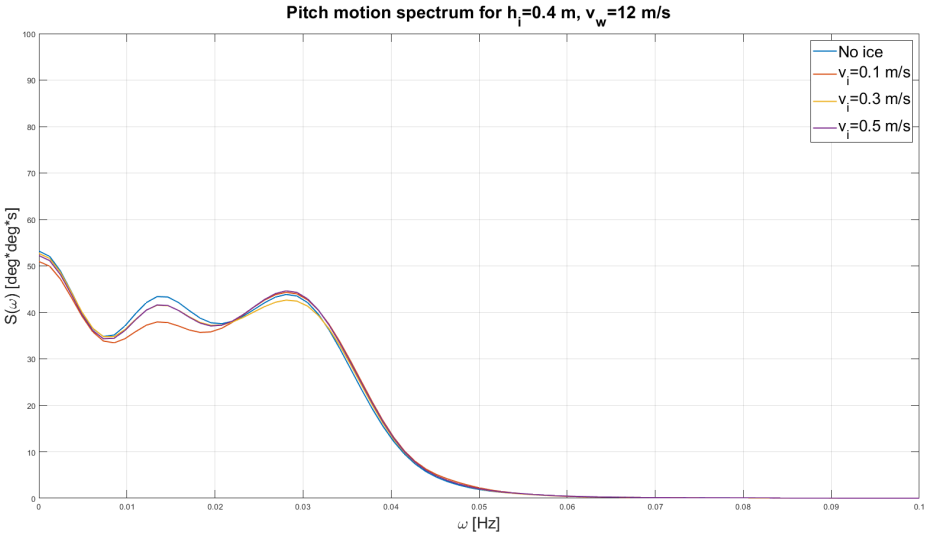

Figure 5.70: Pitch motion spectrum for $h_i = 0.4$ m, $v_w = 12$ m/s and different ice drifting speed

5.4.6 Yaw Motion

Yaw motion time series are presented in Figures 5.71 and 5.72, while the statistical properties are shown in Figures 5.73 and 5.74. In this case too, the ice act like a damper and the yaw motion oscillation are reduced when ice is considered compared to when it is not, as we can see observing the standard deviation. Moreover, the case with $h_i = 0.4$ shows no substantial difference in the phase of the motion time series. On the other hand, a bigger difference can be seen for $h_i = 0.8$, particularly for the case with $v_i = 0.3$ m/s, which time series show more differences in terms of shape then the others.

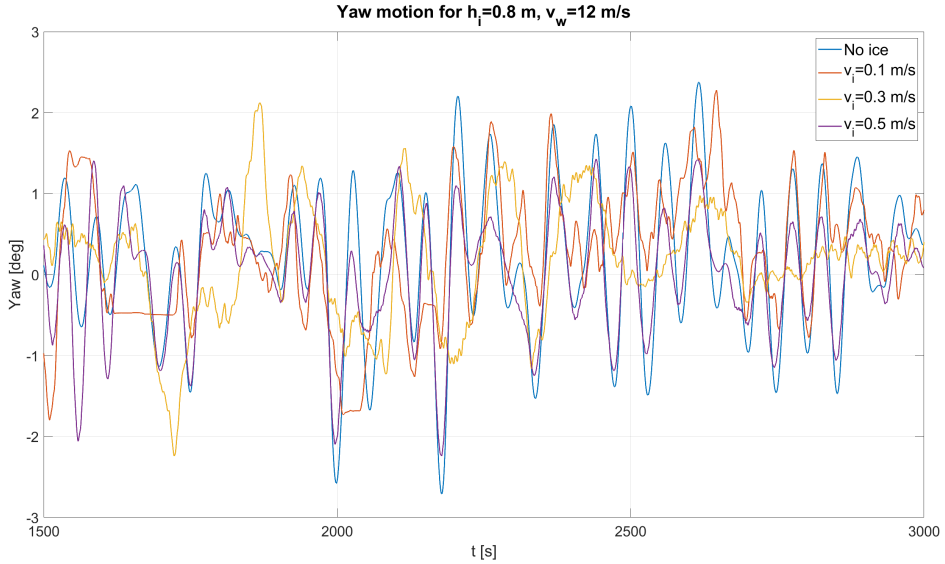

Figure 5.71: Yaw motion time series for $h_i = 0.8$ m, $v_w = 12$ m/s and different ice drifting speed

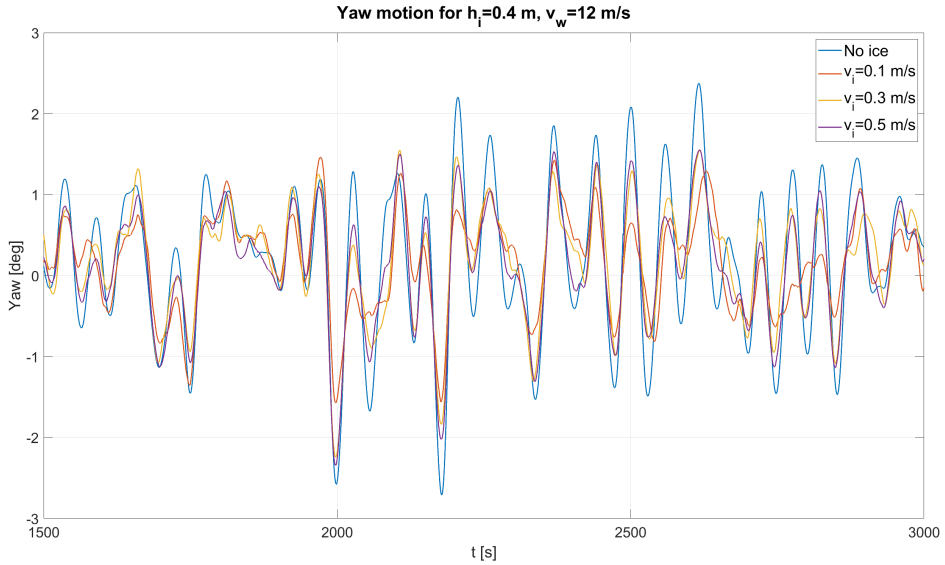

Figure 5.72: Yaw motion time series for $h_i = 0.4$ m, $v_w = 12$ m/s and different ice drifting speed

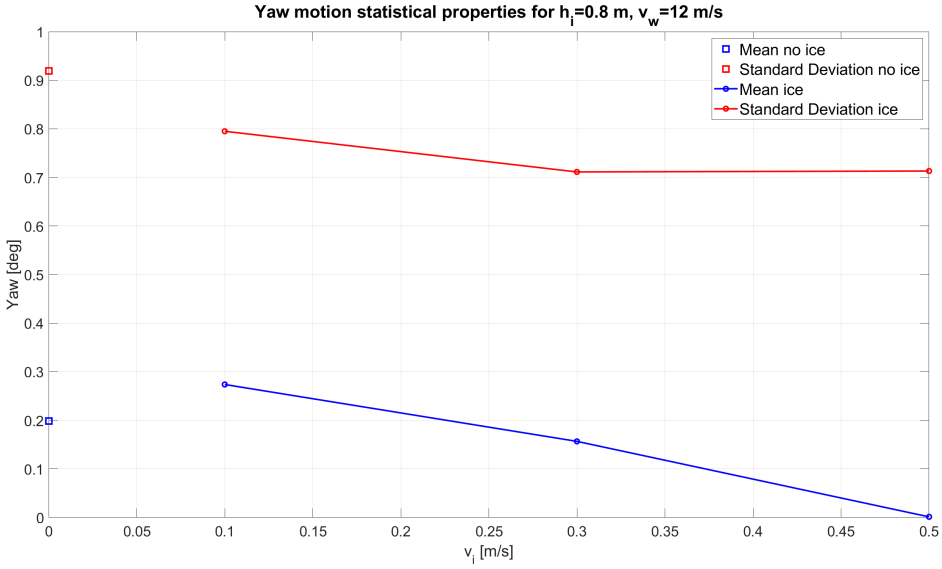

Figure 5.73: Yaw motion statistical properties for $h_i = 0.8$ m, $v_w = 12$ m/s and different ice drifting speed

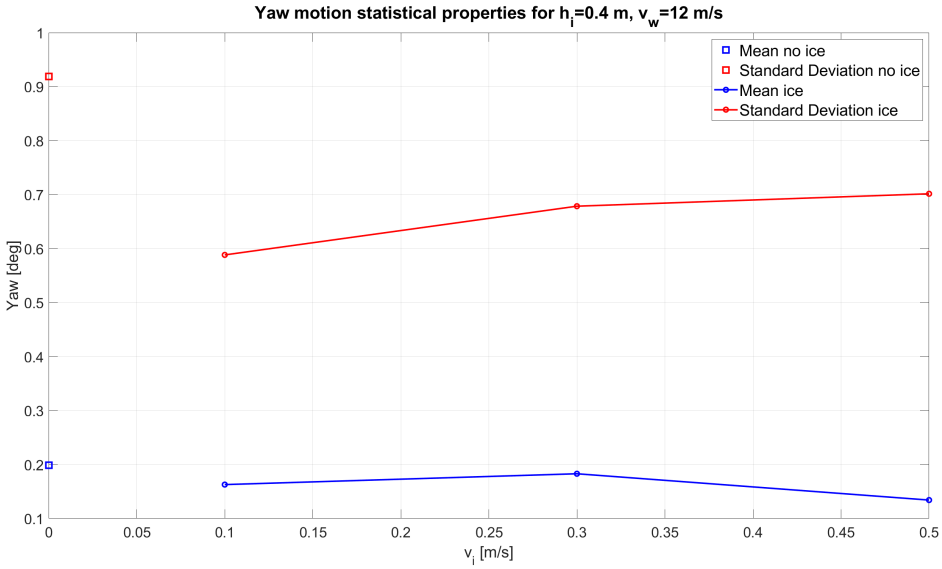

Figure 5.74: Yaw motion statistical properties for $h_i = 0.4$ m, $v_w = 12$ m/s and different ice drifting speed

6 Discussion

6.1 Simulation Length and Time Step

The general setting of all the presented simulations in terms of time step (0.0005 s) and simulation length (3000 s) were chosen in order to avoid the simulation time to be too excessive. With this settings, some simulations took up to 20 hours to be completed. In general, longer simulations with a smaller time step are to be preferred when a more powerful computer is available, but this was not the case. However, a steady state was reached in all the cases and the sensitivity study proved that with the used time step the results were not too far from those obtained with smaller time step, therefore the obtained results are acceptable, even though they may be improved.

6.2 Ice Edge Analysis

The development of the ice edge and its relationship with the ice parameters were analyzed, since it is of primary importance to understand how the ice loads develop in time. The ice edge development is mainly affected by the ice thickness. Thicker ice fails with higher breaking length, meanings that the pieces of broken ice get bigger when the ice get thicker. This aspect, combined with the higher force which is required for thick ice to fail through bending, results in the ice breaking pattern to be more regular for thick ice, with less contact points developing at the same time. On the other hand, thin ice fails more often and in smaller pieces and therefore the ice edge results more irregular, with several contact areas existing simultaneously. This difference in the regularity of the ice edge have been observed to have an influence also on the ice load and particularly on the peak values of the ice load cycle. Peak values are closer to each other for thick ice, while they are distributed over a wider range for thin ice.

6.3 Ice Thickness and Ice Drifting Speed Influence

Ice thickness and drifting speed influence on the ice loads and consequently on the platform motion is the aspect that have been investigated more accurately since this represent the core part of this work. These two parameters affect the ice loads by modifying its magnitude and its frequency: load magnitude increases with both thickness and speed, while the frequency increases with the speed and it decreases with the thickness. As a result, each combination of speed and thickness provides a unique load pattern which can amplify the platform motion or act like a damper. Particularly, we observed that roll motion is the one that tend to be amplified the most by the ice load, especially for slow and thick ice. On the other hand, a strong damping action was found to happen for surge an yaw motion, especially for thick ice. Generally, only a few load cases resulted in amplified motion. More accurate analysis are required in this sense, but from this work we may conclude that ice loads should not represent a problem in terms of rigid body dynamic for the semi submersible platform. It should be noted that the reliability of the case with $v_i = 0.1$ m/s and $h_i = 0.8$ m is questionable due to the problem presented at §5.2.1.

6.4 Wind and Ice Loads Comparison

The main aspect to be highlighted in the comparison between ice and wind loads is that the wind load is the dominating one in the x direction while the ice load is the dominating one in the y direction. The exceptions to that are the highest ice load ($h_i = 0.8$ m), which is comparable to the wind load in the x direction, and the lowest ice load ($h_i = 0.1$ m) which has similar magnitude to the wind load in the y direction. The result of these differences is that the motion controlled by load in the x direction (Surge and Pitch) are dominated by the wind load. Therefore these motions show little to none change when different ice loads are applied. On the other hand, motion controlled by load in the y direction (Sway and Roll) are more affected by the ice loads and they are highly influenced by the ice speed and thickness. These consideration yields for the wind speed presented in this work, i.e. $v_w = 12$ m/s. Other wind speeds deviates more from the rated speed of 11.4 m/s would result in lower wind forces and therefore this consideration may not be valid in those cases.

6.5 Future Developments

This work is intended to be only the first step in the study of the dynamic behavior of semi-submersible wind turbines under combined wind and ice loads and therefore several developments could be performed in order to obtain more accurate and reliable results, to investigate different conditions and eventually to obtain the base for a design procedure.

In order to improve the accuracy of this analysis, longer simulations with smaller time step should be performed and an iterative procedure should be implemented. Moreover, the code should be improved to make it able to analyze cases with thick and slow ice, which presented some issues in this work.

Other important improvements should be achieved regarding the environmental conditions. In this work, ice properties were considered constant during each simulations. However, ice is an extremely complex material and its properties usually vary along its surface. This could be implemented by considering varying ice properties (in terms of thickness, bending strength and crushing strength) along one simulations in order to realize a condition which is closer to the real life one. In addition to the ice condition, also the wave conditions could be improved. In this work we considered as if there where no waves acting on the platform, assuming that they were completely damped out by the ice sheet. This model could be improved by assuming that small waves can propagate under the ice especially if it is thin. Finally, a wake effect should be implemented, because when two columns are aligned in the ice drifting direction the one in the back will be subjected to rubble ice load instead of level ice load. Moreover, different ice drifting direction with respect to the platform orientation should be performed.

The local influence of the ice load on the platform structure should be investigated too. Ice induced vibration are a well-known phenomenon due to the ice loads being cyclic. These vibration can occurs both globally and locally on the side of the column where the contact occurs. Vibrations can have an impact both on the fatigue life of the structure and on its production rate. Therefore, a study on the ice induced vibrations should be performed to asses ice load impact on the wind turbine life and efficiency.

Finally, the results of this work should be validated with full scale data. However, this is not possible at the moment since there are no existing semi-submersible platform which are operating in ice.

7 Conclusion

The aim of this work was to develop a coupled dynamic analysis on a semi-submersible floating wind turbine under combined wind and ice loads. The considered wind turbine is the CSC 10 MW wind turbine, which is supported by a pontoon type steel semi-submersible platform. The turbine model is a aero-servo-hydro-elastic model developed on the software SIMA and it is coupled with a semi-empirical ice module developed through a FORTRAN DLL. The load acting on the platform and on the wind turbine are: ice loads, aerodynamic loads, mooring line loads and hydrodynamic loads. When evaluating the hydrodynamic loads, no waves are considered since they are assumed to be damped out by the ice.

The first part of the work consisted in modifying the ice load DLL in order to make it suitable for the considered case, since it was developed to evaluate the ice load acting on a SPAR buoy and it was meant to be coupled with HAWC2. Some modification were performed in order to make the code compatible with SIMA and to ensure the convergence. A linear load ramp was added before the actual ice load started, since applying the ice load from the beginning of the simulations was leading to the simulation to crash because the load acting on the platform can not increase too fast. Moreover, the initial ramp pushes the platform close to the equilibrium position, so that when the ice loads start it does not undergo excessive motion. However, this resulted in an initial distance between the ice edge and the structure which was again causing some problems. This issue was solved by moving the ice edge into the new equilibrium position before the ice load started. Then, the code was modified to make it able to evaluate the load acting on each of the column of the platform. The position of each column was calculated based on the rigid body motion of the platform utilizing the linear approximation of the equation of motion.

We started by studying the ice load acting on a bottom fixed cylinder without considering the wind turbine. This was done in order to analyze how the DLL works and how the two most relevant parameters, i.e. ice drifting speed and thickness, affect the loads. The findings followed the expectations since we found out that the load magnitude increases with both the ice thickness and speed (the thickness has larger influence) and that the load frequency increases with the ice speed and decreases with the ice thickness. Also the ice edge development in time was studied and its relationship with the ice parameters. Once again, the results followed the expectations since we found out that thick ice tends to break into bigger pieces and to produce a more regular edge then thin ice.

After the ice load on a bottom fixed cylinder has been investigated, we were able to perform coupled analysis on the floating wind turbines considering all the four columns and the combined action of ice and wind loads. We investigated how the ice edge develops around each column for this case, finding out that the resulting channel is wider then the one for the bottom fixed structure due to the lateral motion. We also compared the wind loads with the total ice loads and found out that in most cases wind loads are dominant in the x direction (i.e. the wind and ice drifting direction) while the ice load are dominant in the y direction.

Finally, we investigated the influence of the ice drifting speed and thickness on the platform motion, while considering a turbulent wind with mean speed equal to $v_w = 12$ m/s. As expected, surge and pitch resulted to be affected mainly by the wind load, while roll and sway are more affected by the ice loads. Only a few cases showed a significant amplification of the motion as a result of the ice load, while in most cases the ice appeared to damp out the oscillations.

In the future, this work could be used as a starting point for a more accurate analysis, considering more realistic environmental conditions and including other aspects such as the wake effect induced by one column on the other. Once it has been improved, this methodology could be used to study the effect of ice-induced vibration on the fatigue life of the platform and on its efficiency and eventually it could be used as a preliminary design tool.

References

[1] European Commision. Directive (eu) 2018/2001 of the european parliament and of the council of 11 december 2018 on the promotion of the use of energy from renewable sources. 2018.

[2] European Commision. A policy framework for climate and energy in the period from 2020 to 2030. 2014.

[3] International Renewable Energy Agency. Statistics time series, 2021.

[4] Wikipedia. History of wind power.

[5] Global Wind Energy Council. Global wind report 2021, 2021.

[6] Energy transition outlook 2020, executive summary, 2020.

[7] Orsted. 1991-2001 the first offshore wind farms.

[8] Global Wind Energy Council. Global offshore wind report 2020, 2020.

[9] Yi Li, Xuan Huang, Kong Fah Tee, Qiusheng Li, and Xiao-Peng Wu. Comparative study of onshore and offshore wind characteristics and wind energy potentials: A case study for southeast coastal region of china. *Sustainable Energy Technologies and Assessments*, 39:100711, 2020.

[10] J.K. Kaldellis and M. Kapsali. Shifting towards offshore wind energy—recent activity and future development. *Energy Policy*, 53:136 – 148, 2013.

[11] Equinor. The future of offshore wind is afloat.

[12] Ali Mostafaeipour, Mohammad Khayyami, Ahmad Sedaghat, Kasra Mohammadi, Shahaboddin Shamshirband, Mohammad-Ali Sehati, and Ehsan Gorakifard. Evaluating the wind energy potential for hydrogen production: A case study. *International Journal of Hydrogen Energy*, 41(15):6200 – 6210, 2016.

[13] Global Wind Energy Council. Global wind report 2020, 2020.

[14] Ryan Wiser, Karen Jenni, Joachim Seel, Erin Baker, Maureen Hand, Eric Lantz, and Aaron Smith. Forecasting wind energy costs and cost drivers: the views of the world's leading experts. 2016.

[15] Alex Benjamin Wilson. Offshore wind energy in europe, 2020.

[16] Kate Freeman et al. Our energy, our future, 2019.

[17] Jake Badger et al. Global wind atlas.

[18] M. Jakobsson, C. Stranne, M. O'Regan, S. L. Greenwood, B. Gustafsson, C. Humborg, and E. Weidner. Bathymetric properties of the baltic sea. *Ocean Science*, 15(4):905–924, 2019.

[19] Qiang Wang. Design of a steel pontoon-type semi-submersible floater supporting the dtu 10mw reference turbine. Master's thesis, DTU and NTNU, 2014.

[20] National Snow & Ice Data Center, 2020.

[21] Zhiyu Jiang, Xiangqian Zhu, and Weifei Hu. *Modeling and Analysis of Offshore Floating Wind Turbines*, pages 247–280. Springer International Publishing, Cham, 2018.

[22] Green giraffe - the renewable energy financial advisors.

[23] Global performance analysis of deepwater floating structures, 2010.

[24] Erin Bachinsky et al. Integrated dynamic analysis of wind turbines - lecture notes. 2020.

[25] J Jonkman. Definition of the floating system for phase iv of oc3.

[26] Madjid Karimirad. Marintek numerical tools for coupled aero-hydro-servo-elastic simulations of offshore wind turbines.

[27] Martin OL Hansen and Helge Aagaard Madsen. Review paper on wind turbine aerodynamics. *Journal of fluids engineering*, 133(11), 2011.

[28] MOL Hansen. Aerodynamics of wind turbinessecond edition earthscan. *London, UK*, 2008.

[29] Marine Yvette Josette Saccoman. Coupled analysis of a spar floating wind turbine considering both ice and aerodynamic loads. Master's thesis, NTNU, 2015.

[30] Odd Faltinsen. *Sea loads on ships and offshore structures*, volume 1. Cambridge university press, 1993.

[31] Frank M White. *Fluid mechanics*. 2009.

[32] Johannes Albert Pinkster. Low frequency second order wave exciting forces on floating structures. 1980.

[33] John Nicholas Newman. Second-order, slowly-varying forces on vessels in irregular waves. 1974.

[34] João Pessoa and Nuno Fonseca. Investigation of depth effects on the wave exciting low frequency drift forces by different approximation methods. *Applied Ocean Research*, 42:182 – 199, 2013.

[35] Aleksey Marchenko, Peter Wadhams, C Collins, Jean Rabault, and Mikhail Chumakov. Wave-ice interaction in the north-west barents sea. *Applied Ocean Research*, 90:101861, 2019.

[36] Joseph B Keller. Gravity waves on ice-covered water. *Journal of Geophysical Research: Oceans*, 103(C4):7663–7669, 1998.

[37] Xiang Tan, Biao Su, Kaj Riska, and Torgeir Moan. A six-degrees-of-freedom numerical model for level ice–ship interaction. *Cold Regions Science and Technology*, 92:1–16, 2013.

[38] ISO/FDIS19906. Petroleum and natural gas industries - arctic offshore structures, 2019.

[39] Wojciech Popko, Sebastian Hetmanczyk, Fabian Vorpahl, Jaakkko Heinonen, et al. State-of-the-art comparison of standards in terms of dominant sea ice loads for offshore wind turbine support structures in the baltic sea. In *The Twenty-second International Offshore and Polar Engineering Conference*. International Society of Offshore and Polar Engineers, 2012.

[40] Ning Xu and Qianjin Yue. Dynamic ice force analysis on a conical structure based on direct observation and measurement. *Journal of Offshore Mechanics and Arctic Engineering*, 136(1), 2014.

[41] Ning Xu, Qianjin Yue, Fengwei Guo, et al. Mitigating ice-induced vibration by adding ice-breaking cone. In *The Twentieth International Offshore and Polar Engineering Conference*. International Society of Offshore and Polar Engineers, 2010.

[42] Arkadiusz Mróz, Jan Holnicki-Szulc, and Tuomo Kärnä. Mitigation of ice loading on off-shore wind turbines: Feasibility study of a semi-active solution. *Computers & structures*, 86(3-5):217–226, 2008.

[43] KR Croasdale and AB Cammaert. An improved method for the calculation of ice loads on sloping structures in first-year ice. *Hydrotechnical Construction*, 28(3):174–179, 1994.

[44] Ken Croasdale, Tom Brown, Chee Wong, Noorma Shrestha, George Li, Walt Spring, Mark Fuglem, Jan Thijssen, et al. Improved equations for the actions of thick level ice on sloping platforms. In *Arctic Technology Conference*. Offshore Technology Conference, 2016.

[45] Christian Bak, Frederik Zahle, Robert Bitsche, Taeseong Kim, Anders Yde, LC Henriksen, Peter B Andersen, Anand Natarajan, and Morten Hartvig Hansen. Design and performance of a 10 mw wind turbine. *Wind Energy*, 124, 2013.

[46] Wei Shi, Xiang Tan, Zhen Gao, and Torgeir Moan. Numerical study of ice-induced loads and responses of a monopile-type offshore wind turbine in parked and operating conditions. *Cold regions science and technology*, 123:121–139, 2016.

[47] Kaj Riska. Models of ice-structure contact for engineering applications. *Studies in Applied Mechanics*, 42:77–103, 1995.

[48] *SIMO user manual appendix C.*

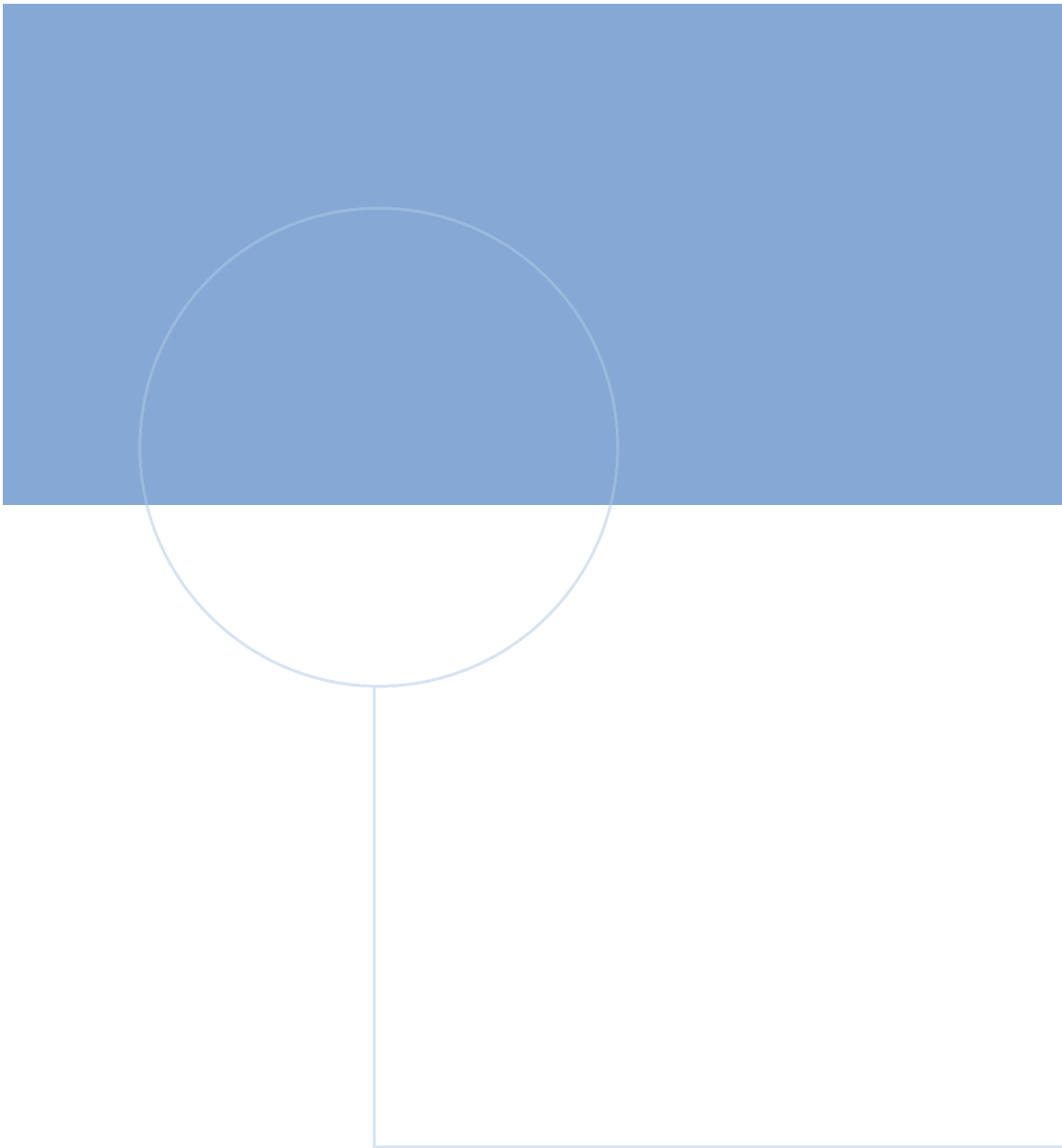

NTNU

Norwegian University of
Science and Technology